Alma Mater Studiorum – Università di Bologna

DOTTORATO DI RICERCA IN
FISICA
Ciclo XXVIII

Settore Concorsuale di afferenza: 02/B1-FISICA SPERIMENTALE DELLA MATERIA
Settore Scientifico disciplinare: FIS/03-FISICA DELLA MATERIA

Charge and spin transport in memristive organic LSMO/Alq3/AlOx/Co spin valves

Presentata da: **Marco Calbucci**

Coordinatore Dottorato:
Prof. Gastone Castellani

Relatore:
Dott. Alberto Riminucci

Co-relatore:
Prof. Federico Boscherini

Esame finale anno 2016

Contents

Introduction

Organic spintronics is a relatively new research field studying organic semiconductors as a medium to transport and control spin-polarized signals, with the aim to combine the advantages of organic electronics (cheap fabrication, low-weight, mechanical flexibility) and spintronics (control of the electron's spin, instead of or in addition to its charge). Since the pioneering works [1, 2] at the beginning of this century, organic spintronics drew great attention, not only for its technological interest but also because it offers the possibility to understand the fundamental physics behind spin injection and transport in organic semiconductors. In parallel to the evolution of organic spintronics, memristors (non volatile electrical memories) were the object of a significant research effort. Theoretically predicted in 1971 [3] as the fourth circuit element, the memristor was realized in 2008 [4], becoming one of the most promising candidates for the post-complementary metal oxide semiconductor (CMOS) era.

In this thesis I studied $La_{0.7}Sr_{0.3}MnO_3$/Alq3/AlOx/Co organic spin valves, which are multifunctional devices showing an interesting interplay between magnetoresistive effects and memristive switching [5, 6]. In particular this work aims at elucidating the elusive mechanisms for spin injection and transport in this archetypal structure. While spin injection in organic materials was demonstrated by different spectroscopic techniques [7, 8], the origin of magnetoresistive effect in organic spin valves is still debated. In fact, the Hanle effect, considered to be the only reliable proof for spin transport across the organic spacer layer, has not been observed in such a device, yet [9].

I investigated the thickness and temperature dependence of charge transport and magnetoresistive properties, and demonstrated the absence of the Hanle effect. Moreover I studied how the resistance and magnetoresistance of our devices were affected by memristive switching, which turned out to be a fundamental tool to

enlighten the comprehensive picture.
In chapters 1 and 2, I will introduce the basic properties of organic spintronics and resistive memories, giving a brief overview from the recent literature about these topics.
Chapter 3 contains a description of the equipment and techniques used to characterize the devices, as well as their fabrication process.
Chapter 4, contains a description of the charge transport and magneto-transport properties of our devices, showing that two clearly distinguishable conduction regimes can be found for magnetoresistive and non-magnetoresistive devices. An equivalent circuit model, represented by a metallic channel and a hopping channel acting in parallel, will be introduced in order to describe the former regime.
Chapter 5 demonstrates that the Hanle effect is missing in our devices.
Chapter 6 shows that electrode-induced artifacts can be ruled out as the responsible for SV signals.
Finally, chapter 7 contains a description of the effects of the memristive switching on the resistance and magnetoresistance of the devices, showing that they can be coherently explained in the framework of the above mentioned parallel circuit model.
The thesis work was carried out at the Institute of Nanostructured Materials (ISMN-CNR) in Bologna, Italy.

Chapter 1

Organic Spintronics

1.1 Organic Electronics

Organic electronics is a branch of electronics which employs a new class of organic materials known as Organic Semiconductors (OSC). These materials have been synthesized since 1970s and for their discovery A.J. Heeger, A.G. MacDiarmid and H. Shirikawa were awarded with the Nobel Prize in 2000. The enormous progress in this field has been driven by the expectation to realize new applications, such as large area, flexible light sources and displays, low-cost printed integrated circuits or plastic solar cells from these materials [10]. Today, organic semiconductors are already widely used commercially in xerography, employed as light emitting diodes (OLEDs) for display and lighting applications, or field effect transistors (OFETs). Moreover they are making progress to enter the solar cell market [11]. The knowledge of the physics behind this materials is of crucial importance to advance further with the associated semiconductor applications. A central problem is the understanding of the involved charge transport mechanisms, which will be treated in this chapter. It should be mentioned that these materials are referred to as semiconductors despite they are inherently insulators, with a very low intrinsic conductivity ($<10^{-12}$ $\Omega^{-1}\text{cm}^{-1}$) compared to that of an inorganic semiconductor such as silicon, germanium, or gallium arsenide (10^{-8}-10^{-2} $\Omega^{-1}\text{cm}^{-1}$). However, an inherent insulator can be converted into a semiconductor if free charge carriers are generated extrinsically [12].

1.1.1 Electronic properties of Organic Semiconductors

The π-conjugated materials used in organic electronics are mainly composed of carbon atoms, and also of other low-atomic-number atoms like oxygen, nitrogen and sulfur. These materials are characterized by chains of alternating single and double carbon-carbon bonds, that is conjugation. The conjugation is a result of the so-called sp^2 hybridization of carbon atoms, that yields three covalent σ-bonds within a plane. The remaining p_z orbital overlaps with the corresponding p_z orbital of an adjacent carbon, yielding π-bonding and π^*-antibonding orbitals (figure 1.1), delocalized over the molecule or, in the case of polymers, over large segments of the polymer chain.

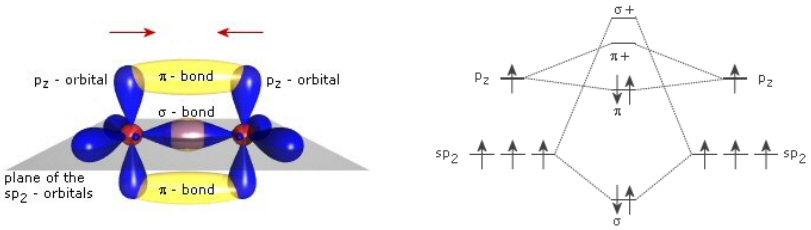

Figure 1.1: Scheme of the orbitals and bonds for two sp^2-hybridized carbon atoms.

In the ground state of the molecule (figure 1.2a), all bonding orbitals up to the highest occupied molecular orbital (HOMO) are filled with two electrons of antiparallel spin, while the antibonding orbitals, from the lowest unoccupied molecular orbital (LUMO) onwards, are empty. In general, any configuration with an additional electron in an antibonding orbital and a hole in a bonding orbital corresponds to a neutral excited state (figure 1.2b,c). Due to the low relative dielectric constant in organic semiconductors (on the order of $\epsilon_r \approx 3$), coulomb attraction between electron and hole is strong, resulting in an exciton binding energy ranging from 0.5 eV to more than 1 eV [12]. For charge transport to take place, there must be a charge on the molecular unit. This can be an additional electron in an antibonding orbital, or one that is removed from a bonding orbital. The addition or removal of an electron from the molecule may be obtained through injection or extraction of an electron at the interface between a metal electrode and the molecule, through reduction or oxidation of the molecule by a dopant molecule, and through thermal dissociation of a neutral excited state in molecule by electron transfer to an adjacent molecule. When an electron is taken from a π-orbital or added to a π^*-

orbital, this alters the spatial distribution of electrons in the more strongly bounds σ-orbitals, resulting in different bond lengths of the molecule. The combination of the charge with the geometric distortion of the molecule is referred to as a polaron (figure 1.2d,e).

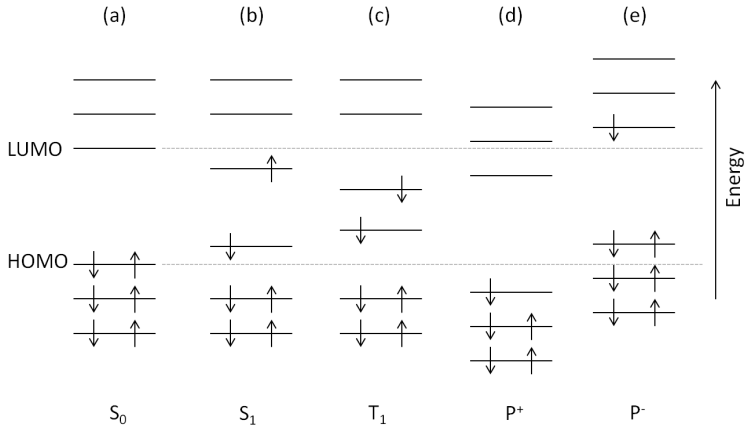

Figure 1.2: Molecular orbital diagram showing the electronic configuration for the ground state S_0 (a), for the first spin-singlet excited state S_1 (b) and for the first spin-triplet excited state T_1 (c). The arrows indicate the electron spin, the thin horizontal gray line is a guide to the eye. In this representation, coulomb and exchange energies are explicitly included in the positions of the frontier orbitals. Molecular orbital diagram for positively charged molecule (d) and negatively charged molecule (e) are also shown. The shifts in the molecular orbital levels upon charging are only drawn in a qualitative fashion. Adapted from Ref. [12].

In a solid state material, the molecules interact among each other and the molecular energy levels are perturbed. Figure 1.3 compares the electronic structures of a single organic molecule, an organic crystal, and an inorganic semiconductor crystal. In inorganic semiconductors, such as Si or Ge, atoms are bound by strong covalent bonds to form a crystal and few eV wide bands are formed which allow for charge transfer at high mobilities. In contrast, molecular crystals are kept together by weak van der Waals bonds and the resulting bands are narrow, with a bandwidth below 500 meV [13]. In amorphous films, deposited by spin-coating or evaporation, the surrounding polarization for a molecule varies spatially in a random fashion, leading to a random distribution of the absolute values of the molecular energies. For this reason they are generally described by a Gaussian distribution of electronic sites with a variance that is characteristic for the energetic disorder. In this work

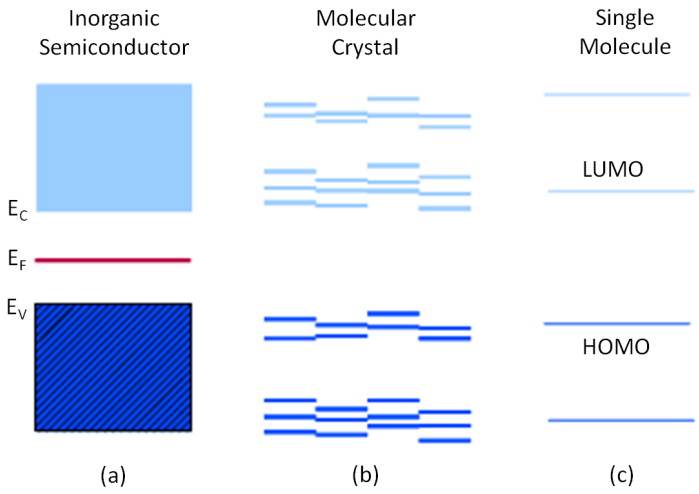

Figure 1.3: Schematic representation of the electronic structure of an inorganic semiconductor (a) in comparison to that of a molecular crystal (b) and a single molecule (c). The free molecules have well defined energy levels. In a molecular crystal molecules weakly interact and a disordered distribution of localized energy levels can be observed, while in the inorganic semiconductor a stronger interaction between molecules led to the formation of a conduction band.

a disordered organic semiconductor, Tris(8-hydroxyquinolinato)aluminium (Alq3), has been used and I will focus my attention on the charge transport properties of this kind of materials.

1.1.2 Charge transport in disordered OSCs

A disordered organic material, made of polymers or small molecules, can be modeled as a homogeneous distribution of electronic sites which can host charge, with hole or electron transporting states following a Gaussian distribution of energies

$$N(E) = \frac{1}{\sqrt{2\pi}\sigma} exp\left(\frac{E^2}{2\sigma^2}\right), \tag{1.1}$$

schematically illustrated in figure 1.4. The tacit assumption contained in equation 1.1 is that the energies of adjacent sites are uncorrelated. Since structural correlation lengths in organic do not exceed a few intermolecular distances at most, it appears to be a reasonable assumption [14]. Localized charge carriers may travel through the material by hopping from one localized state to the next and the rate at which this occurs is related to the conductivity of the material. This process is

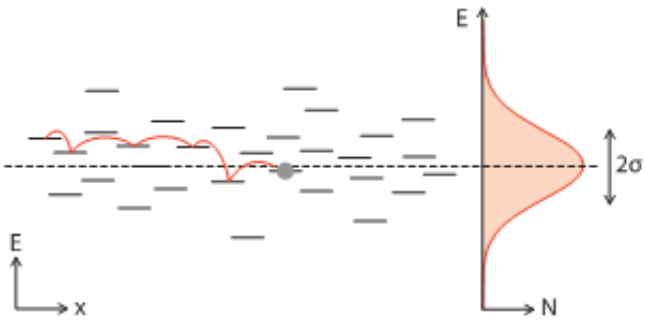

Figure 1.4: Schematic representation of electronic sites in a disordered organic material. It is a common assumption that the number of sites per energy N(E) follows a Gaussian distribution. The hopping of a carrier is illustrated.

described by a probability evolution equation known as master equation [15]:

$$\frac{\partial}{\partial t} f_i(t) = +\sum_{j \neq i} W_{ji} f_j(t)[1 - f_i(t)] - \sum_{j \neq i} W_{ij} f_i(t)[1 - f_j(t)] - \lambda_i f_i(t) \qquad (1.2)$$

where $f_i(t)$ is the probability that the site i (at location R_i and energy E_i) is occupied by a carrier or excitation at time t and $[1 - f_j(t)]$ is the probability that the site j is unoccupied, W_{ij} is the transition rate from site i to site j, and λ_i is the decay rate of the excitation at site i. Often one assumes that recombination is only a small perturbation, taking $\lambda_i = 0$. The first Monte Carlo simulations of hopping transport were performed by Bässler [14] for the case of a Gaussian disorder model (GDM). He assumed the transition rate W_{ij} to be of the Miller-Abrahams type [16]:

$$W_{ij} = \nu_0 exp(-2\gamma|R_{ij}|) \begin{cases} exp(-\frac{(E_j - E_i)}{kT}) & \forall E_j > E_i \\ 1 & \forall E_j < E_i \end{cases} \qquad (1.3)$$

where ν_0 is the phonon vibration frequency (can be intuitively considered as the "jump-attempt" rate), γ is the inverse localization radius (the result of the overlap integral of the wavefunction assuming exponential decay with distance), and E_i and E_j are the energy levels of the respective sites, which are supposed to contain also the contribution due to the applied electric field. A cubic lattice with periodic boundary condition is considered, and random energy values are assigned to each lattice site following eq. 1.1 with a given variance. Then a number of carriers are started on an arbitrary site and the simulated time-of-flight (TOF) experiment is

performed, keeping track of the mean position <x> and the mean energy <E> of a carrier as a function of time. The carrier mobility, a key parameter for the charge transport, is inferred from the mean carrier arrival time at the exit contact, allowing to study its field and temperature dependence. The Bassler's simulations showed a non-Arrhenius temperature dependence $\mu \propto exp(-c\hat{\sigma}^2)$, with $\hat{\sigma} \equiv \sigma/k_BT$, and a Poole-Frenkel $\mu \propto exp(\gamma\sqrt{F})$ behavior, in a limited range, for the dependence on electric field (here defined by F in order to be distinguished from the energy E). Several improvements of the initial GDM model have then been suggested. First, spatial correlations of the energies of transport levels in disordered media have been taken into account [17]. Then it was demonstrated that the mobility can strongly depend on the charge-carrier density. In fact, experiments on hole-only diodes and FETs, with the same polymer as active material, showed that μ can differ up to 3 orders of magnitude between the diode and the FET, where the current is confined to a thin layer of the dielectric [18]. Taking into account the dependence on charge-carrier density led to the development of a so-called extended Gaussian disorder (EGD) model [19, 20, 21, 22]. These groups used different approaches to describe the mobility in organic systems where interactions among charge carriers are not negligible due to the presence of a space charge. Space charge effects can occur in presence of charged traps or ionized dopant molecules modifying the density of states (DOS), or if the current flowing through the dielectric is sufficiently large so that a non-negligible fraction of tail states of the DOS is already occupied. In the latter case the carrier statistics becomes Fermi-Dirac-like whereas it is Boltzmann-like if state filling is negligible [12].

Space charge limited current

The theory of space charge limited current (SCLC) in insulating solids was formulated by Rose [23] and Lampert [24]. In the case of a perfect insulator without intrinsic carriers and traps, assuming a constant charge carrier mobility and neglecting diffusion, the SCLC can be derived from the equations

$$J = ne\mu F, \tag{1.4}$$

$$\frac{dF}{dx} = \frac{e}{\epsilon_o \epsilon_r} n, \tag{1.5}$$

$$V = \int_0^d F(x)dx, \tag{1.6}$$

where F is the electric field, n the charge density, V the applied bias voltage, and d the dielectric layer thickness. The solution gives the Mott-Gurney equation:

$$J_{SCLC} = \frac{9}{8}\epsilon_o\epsilon_r\mu\frac{V^2}{d^3} \tag{1.7}$$

However, as seen above, the assumption of a constant charge carrier mobility is unrealistic, and several groups tried to describe this SCL regime taking into account the mobility dependence on field, temperature, and charge carrier density [19, 20, 21]. An approximate analytic solution has been given for a Poole-Frenkel like mobility [25]. In this approximation the current is described as the trap free SCL current multiplied by the field and temperature dependent mobility:

$$J_{SCL}^{PF} = \frac{9}{8}\epsilon_o\epsilon_r\frac{(V-V_{bi})^2}{d^3}\mu_{PF} \quad exp\left(-\frac{\Delta E}{k_B T_{eff}} + \frac{\beta_{PF}\sqrt{V-V_{bi}}}{k_B T_{eff}\sqrt{d}}\right) \tag{1.8}$$

where V_{bi} is the built-in voltage, μ_{PF} is the Poole-Frenkel mobility pre-factor, ΔE is the activation energy at zero field, and β_{PF} is the so called Poole-Frenkel pre-factor. T_{eff} is the effective temperature, given by the relation

$$\frac{1}{T_{eff}} = \frac{1}{T} - \frac{1}{T_0}, \tag{1.9}$$

where T is the absolute temperature and T_0 is an empirical parameter.

Trap charge limited current

The SCLC theory was extended to include the effect of charge trapped in either shallow or deep levels. In the trap charge limit (TCL) a sharply reduced carrier mobility is observed at low voltages due to charge capture in traps. Increasing bias results in an increase of injected charge, thereby filling the limited number of traps. Due to the reduction in empty traps the current will increase faster than quadratic until all traps are filled. At sufficiently high injection levels, all the traps are filled, and consequently the current becomes SCL. The problem has been solved analytically for a constant charge carrier mobility and an exponential trap distribution

$$N_t(E) = \left(\frac{N_t}{kT_t}\right) exp\left(\frac{E - E_{LUMO}}{kT_t}\right), \tag{1.10}$$

where N_t is the total trap density and T_t is the characteristic temperature of the exponential trap distribution. The current density for unipolar electron injection

is given by

$$J_{TCL} = N_{LUMO}\mu_n q^{1-m}\left(\frac{\epsilon m}{N_t(m+1)}\right)^m\left(\frac{2m+1}{m+1}\right)^{m+1}\frac{V^{(m+1)}}{d^{(2m+1)}}, \tag{1.11}$$

where $m = T_t/T$ and N_{LUMO} is the density of the state in the LUMO band [26]. If both the presence of traps and a field dependent mobility are included, in general, only numerical solutions of the problem are possible.

Injection limited current

In the pure SCL regime treated above one assumes that at least one contact has good injecting properties and can be considered as an inexhaustible carrier reservoir. By contrast one has a purely injection limited current (ILC) when the current behavior is dominated by the injection mechanism. In conventional crystalline inorganic semiconductors, the charge injection is described in terms of Richardson-Schottky emission or Fowler-Nordheim tunneling [27], schematically illustrated in figure 1.5. In the former mechanism, electrons are thermally excited

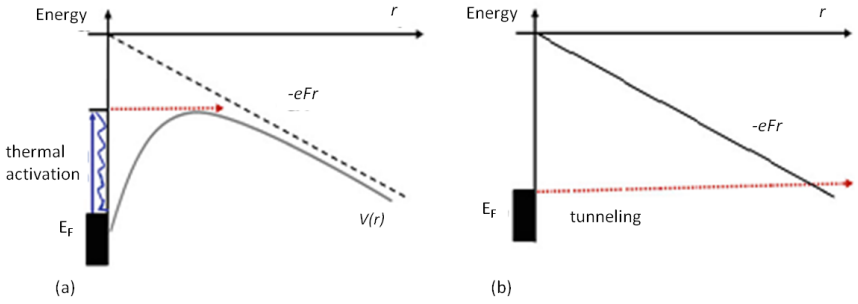

Figure 1.5: Schematic representation of electron injection from a metallic electrode into a semiconductor (a) via Schottky emission and (b) via Fowler-Nordheim tunneling. Adapted from Ref. [12].

from the Fermi level of the electrode across the interfacial barrier modified by the coulomb potential of the image charge and the applied electric field without being scattered. It gives rise to an Arrhenius-type temperature dependence ($lnJ \propto T$) and a Poole-Frenkel-type of field dependence ($lnJ \propto \sqrt{F}$) and is expected to dominate at high temperature. For very large barriers or at low temperatures, Fowler-Nordheim mechanism has been thought to dominate the injection process.

In this case, an electron tunnels through a triangular potential barrier set by the interfacial energy barrier and the applied potential, while the image potential is ignored. However, the crucial condition for both mechanism to work is a strong interaction among the lattice elements giving rise to wide valence and conduction bands, implying that the scattering length of charge carriers is much larger than the interatomic separation. This is not the case for organic molecules, typically interacting by weak van der Walls forces. Thus, this classic models fail in describing charge injection in organic semiconductors. In 1999 a model for charge injection in a disordered organic material has been proposed by Arkhipov et al. [28], supported by Monte Carlo simulations [29]. The existence of an image charge at the electrode, the hopping-type of charge transport, and the presence of disorder existing in a non-crystalline system are taken into account, es schematically illustrated in figure 1.6. The model is based on the idea, originally introduced by Gartstein

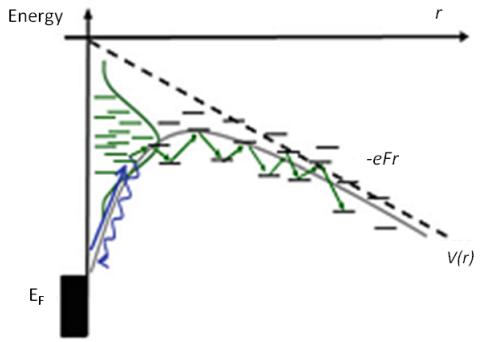

Figure 1.6: Schematic representation of electron injection from a metallic electrode into a semiconductor via hopping in a disordered organic solid [12].

and Conwell [30], that a thermally excited electron can jump to a tail state of the DOS at an interface site, subject to the condition that this site has at least one hopping neighbor at equal or even lower energy. This condition ensures that the injected carrier can continue its motion away from the interface avoiding the recombination with its image charge in the electrode. Since then several models have been proposed [31, 32, 33], all based on the existence of a tail state in the DOS at the interface, which allows the electrons to jump in the dielectric medium and be transported by meas of a hopping mechanism. Since in a bulk system the low energy sites are spatially fixed, the injection process is NOT spatially homo-

geneous, but filamentary, as pointed out by van der Holst et al. [33].
Finally the thickness dependence of the current density at constant applied field is an important parameter to distinguish between these three pictures (SCLC, TCLC, ILC). For purely injection limited behavior (regardless what the actual mechanism is in detail) the current has no explicit thickness dependence. For trap-free SCL regime, the current at constant field results inversely proportional to d. For space-charge limited conduction, with an exponential trap distribution and a constant mobility, the current at constant field scales with d^{-l}, with $l > 1$ [34].

Polaron-based models

As already mentioned, due to the weak intermolecular interaction, organic materials have not a rigid structure and a propagating charge carrier is able to distort the hosting molecule physical structure. The charge carrier with the induced deformation can be treated as a quasi-particle called polaron. To incorporate polaron effects, Fishchuk et al. [22] replaced the Miller-Abrahams-type of hopping rate with a Marcus rate

$$W_{ij} = \frac{J^2}{\hbar}\frac{\pi}{\sqrt{2U_b kT}} exp\left(-\frac{U_b}{2kT}\right) exp\left(-\frac{(E_j - E_i)}{2kT} - \frac{\beta(E_j - E_i)^2}{8kTU_b}\right) \qquad (1.12)$$

where J is related to the overlap integral and is given by $J^2 = J_0^2 exp(-2\gamma|R_{ij}|)$, and U_b is the polaron binding energy. Under steady-state and quasi-equilibrium (low electric field) conditions, the difference between equations 1.3 and 1.12 is negligible. Polaron-based models will not be treated here, however an interesting comparison with the pure disordered-based models can be found in the review by Bässler et al. [12].

1.1.3 Metal-OSC interface

When a π-conjugated molecule or polymer is brought into contact with the surface of another material, the adsorption process may result in a wide variety of effects: polarization of the electron density of the organic material due to interaction with an image charge on the substrate surface, partial charge transfer through covalent organic-substrate bonds, integer charge transfer through tunneling across the organic/substrate interface, surface rearrangement by (inter)diffusion across

the organic/substrate interface, adsorption-induced order or disorder [35, 36]. This variety of interfaces are classified by the strength of the involved interactions, subdivided into physical adsorption (Physisorption) and chemical adsorption (Chemisorption).

Physisorption

In the case of physisorption the molecules interact with the substrate (in our case the electrode of the device) by weak physical forces (on the order of 0.1 eV), which cause no chemical bonding. Generally, this is the case of interfaces with an electrode unintentionally passivated by oxide or residual hydrocarbons, and of engineered barrier layers. Typically Al_2O_3 or LiF [37] are used in order to isolate the FM surface from the OSC interface layer preventing chemical interaction and interdiffusion (mixing). Even if no chemical bonds are involved and the insulator barrier has no intrinsic dipole, the work function of the FM electrode always will be strongly modified due to the so-called push-back effect [38]. Moreover, electron transfer can still occur by tunneling if the passivating layer is thin enough [36]. This implies the transfer of an integer amount of charge, one electron at a time, into well-defined charged states on the polymer or molecule. This process is known as Integer Charge Transfer (ICT) model, illustrated in figure 1.7.
When the substrate work-function is larger than the energy of the positive integer charge state of the π-conjugated organic material ($\Phi_{SUB} > E_{ICT+}$) as illustrated in figure 1.7a, electrons within tunnel distance begin to flow spontaneously from organic material into the electrode. As this charge transfer takes place, the organic molecules at the interface become increasingly positively charged and the electrode increasingly negatively charged, creating a dipole potential at the interface that down-shifts the vacuum level. This flow continues until equilibrium is reached, where the E_{ICT+} together with the potential energy Δ at the interface equals the substrate work-function. In the case $E_{ICT-} < \Phi_{SUB} < E_{ICT+}$ charge transfer across the organic substrate cannot occur because the cost in energy of creating a hole in the organic material at the organic/electrode interface is greater than what is gained by the substrate when accepting an electron, and the same holds for electron transfer from substrate to organic molecules at the interface. Then there is no vacuum level offset (1.7b). Finally, when the substrate work-function

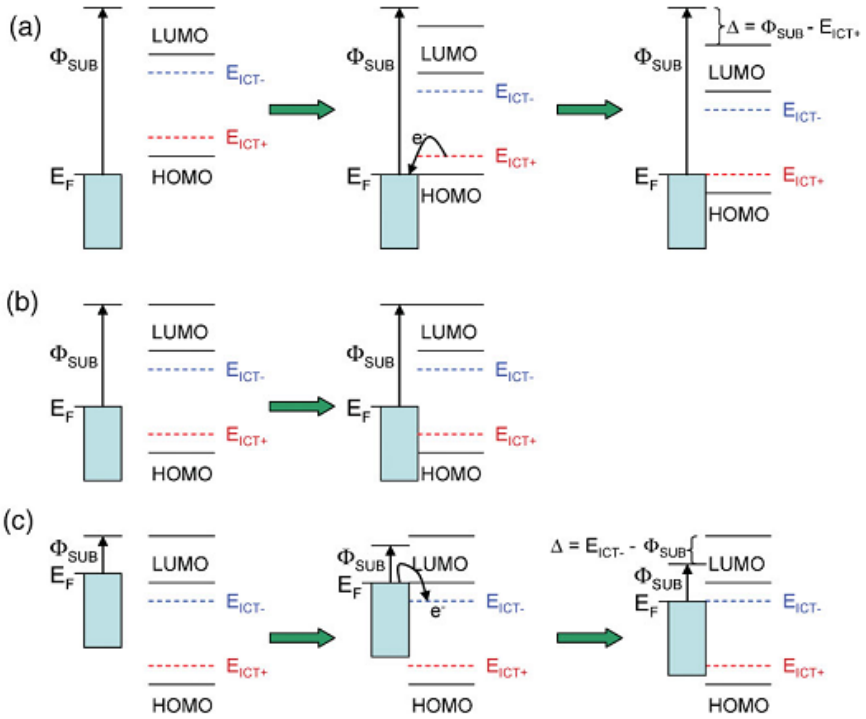

Figure 1.7: Schematic illustration of the evolution of the energy-level alignment when a π-conjugated organic molecule or polymer is physisorbed on a substrate surface when a) $\Phi_{SUB} > E_{ICT+}$: Fermi-level pinning to a positive integer-charge state, b) $E_{ICT-} < \Phi_{SUB} < E_{ICT+}$: vacuum level alignment, and c) $\Phi_{SUB} < E_{ICT-}$: Fermi-level pinning to a negative integer charge-transfer state. The charge-transfer-induced shift in vacuum level, Δ, is shown where applicable [36].

is smaller than the energy of the negative integer charge state of the π-conjugated material ($\Phi_{SUB} < E_{ICT-}$) as illustrated in figure 1.7c, electrons will spontaneously flow from the electrode to the organic molecules at the interface (tunnel distance) until equilibrium is reached. In this case the resulting dipole potential up-shifts the vacuum level.

Chemisorption

In the case of chemisorption the molecules interact with the electrode by chemical bonds (with an involved energy of about 1 eV). Generally, chemisorption takes place in the case of organic films deposited onto atomically clean metal surfaces.

Metal-on-organic interfaces in particular will often feature a rough interface due to diffusion of metal atoms into the organic film, and the organic material may offer a number of different feasible bonding sites for the metal [36]. Systems in which the chemical interactions are moderate but non-negligible (i.e. vapor deposition of π-conjugated molecules on clean but nonreactive metals such as gold) can be described by the hybridization-induced states (HISs) model, a combination of DFT, many-body, and Green-functions techniques. The key idea of this model is that, when the molecules adsorb onto the clean metal surface, there is a resonance of the molecular states with the metal continuum of states that gives rise to a shift and broadening of the molecular levels, and that each molecular level is broadened into a Lorentzian function (figure 1.8). The sum of the contributions of the different molecular levels transforms the initial discrete distribution into a continuum DOS with non-negligible values in the former energy gap. By filling this induced DOS by the charge of the isolated and neutral molecule, the position of the charge neutrality level (CNL) is obtained. The relative position of the semiconductor CNL and substrate Fermi level then determines the direction and size of the charge transfer between the molecules at the interface and the metal substrate.

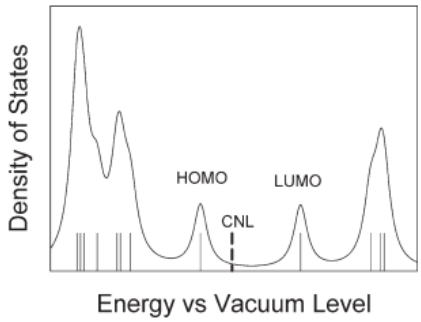

Figure 1.8: Schematic illustration of the calculated molecular-orbital energies for the isolated molecule (bars) and the Lorentzian broadened density of states (curve). The charge neutrality level, CNL, is depicted as dashed line [36].

Energy level alignment at the metal/OSC interface

The electrode/OSC interfaces are very critical for the device performance and in the past decades they have been investigated by many groups [35, 36, 39]. Here I

will focus on the interface energy-level-alignment studied in organic spin valves, in particular in the prototypical LSMO/Alq3/Co structure, which is used in this work. In their pioneering work, Xiong et al [2] gave a schematic energy level diagram in which the vacuum level of the Alq3 spacer layer is aligned with the vacuum level of both the cobalt and LSMO electrodes (figure 1.23c reported in paragraph 1.3.1), suggesting that holes are the main carriers in the spin valve, since the electron injection barriers are too high. However, UPS measurements performed by Zhan et al. [40] gave totally different results. Indeed, they revealed the existence of 1.4 eV interface dipole at the Co/Alq3 (cobalt on Alq3) interface, which results in a 2.1 eV hole-injection barrier. By choosing an Alq3 HOMO-LUMO gap determined from scanning tunneling spectroscopy STS data, an electron-injection barrier of around 1 eV is then obtained [41], suggesting the electrons as the main carriers. If taking band gap obtained by inverse-photoelectron spectroscopy (IPES, 4.6 eV [42]) or ballistic-electron-emission spectroscopy (BEES, 4.8 eV [43]), the electron-injection barrier is also more than 2 eV. The Alq3/LSMO interface has similar properties. UPS measurements showed a 0.9 eV interface dipole, yielding a 1.7 eV hole-injection barrier [44]. Figure 1.9 schematically illustrates these results, showing that the electron and hole-injection barriers are not negligible, at both the studied interfaces. Similar results have been obtained from many metal/OSC

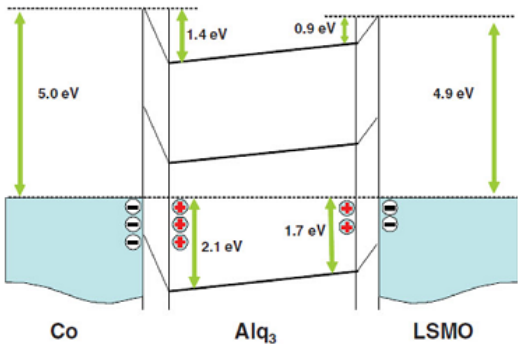

Figure 1.9: Schematic representation of the energy level alignment in a Co/Alq3/LSMO spin valve structure. The reported values are taken from UPS measurement reported in the text [40].

interfaces. Some examples are reported in the table in figure 1.10. This picture seems not compatible with electrical characterizations performed on vertical spin valve structures, showing that electrons or holes can be injected into the OSC at

	6T/ LSMO	CuPc/ LSMO	NPB/ LSMO	Fe/ Alq_3	Pn/CoO_x/ Co	Pn/Al_2O_3/ Co	Rubrene/ Al_2O_3/Co	C60/ Co	C60/Alq_3/ Co	Co/Al_2O_3/ Alq3	Fe/ Alq_3
Φ	4.8	4.9	4.6	4.5	4.3	3.1	3.5	5.2	5.2	5.0	4.6
Δ	−0.4	−0.8	−0.1	−1.1	−0.1	0	−0.2	−0.6	−0.9	−1.3	−1.1
h+ barrier	0.2	0.4	0.8	2.2	1.0	2.2	2.3	1.7	2.0	2.0	2.5
e^- barrier	2.4	1.7		2.6				0.6	0.3		

Figure 1.10: Metal work function Φ, interfacial dipole Δ, and hole and electron-barrier for some metal/OSC interfaces. The table is taken from the review work by Zhan et al. [41], where the references relative to each column can be found.

low bias (a few millivolts) and low temperatures [2, 45]. A solution to this apparent contradiction has been indicated in interfacial hybridization-induced states (HISs), already discusses above. In fact, if HISs at the interfaces are induced around the Fermi level, remaining partially unoccupied, this will transform the OCS/metal interface into a ohmic-like contact. Such states located around the interface Fermi level have been observed by NEXAFS [46] and UPS [47] for several interfaces. Clearly, the injected carrier has then to overcome the energy differences between HIS and OSC bulk states, proceeding by hopping towards the opposing electrode. Since the rising of organic spintronics, many group have also studied the spin-polarization properties of these HISs at the FM/OSC interface, as will be discussed below in the paragraph 1.3.4.

1.2 Spintronics

Spintronics is a rapidly emerging branch of electronics which exploits the spin degree of freedom in addition to the electron charge. Generally when a material or a device changes its resistance under the influence of a magnetic field, this property is referred to as magnetoresistance. The first known phenomenon where the electrical resistance is altered by the direction of a magnetic moment is called anisotropic magnetoresistance (AMR), discovered in 1857 by Thomson [48]. In 1973, Tedrow and Meservey determined for the first time experimentally the spin polarization of the conduction band in a FM material using a FM/tunnel barrier/superconductor junction [49]. This work was then used to explain the tunnel magnetoresistance (TMR) in FM/tunnel barrier/FM junctions, observed by Jullière in 1975 [50]. The tunnelling current is proportional to the product of the DOS

for each spin sub-band, and is hence dependent on the relative orientation of the magnetizations in both FM layers. TMR is therefore a pure interface effect and does not require spin transport in the NM layer. In 1988 for the first time spin polarized transport through a NM metal was demonstrated with the discovery of the giant magnetoresistance (GMR) by Albert Fert [51] and by Peter Grunberg [52], awarded with the Noble Prize in 2007. The wish to combine semiconductor and spintronic concepts stimulated efforts to inject spins into a semiconductor, and only very recently an all-electrical spin injection and detection was demonstrated for an inorganic semiconductor [53]. One of the major obstacles for spin injection/detection in semiconductor devices is the so-called conductivity mismatch between the semiconductor spacer and the metallic FM contacts [54].

1.2.1 Tunnel Magnetoresistance

Tunnel magnetoresistance (TMR) is a magnetoresistive effect which occurs in a magnetic tunnel junction (MTJ), a device consisting of two ferromagnetic (FM) electrodes separated by a thin non magnetic (NM) insulating barrier. This effect consists in the variation of the device resistance depending on the relative magnetization of the FM electrodes. Jullière was the first who reported a magnetoresistance effect in a Co/Ge/Fe MTJ in 1975. At 4.2 K he got a change in conductance of $\Delta G = 14\%$ [50]. The Jullière's model describes the TMR in terms of the spin polarization of the two FM electrodes and the experimental values for spin polarization were taken from the work of Tedrow and Meservey [49]. It is assumed that the transmission probability of electrons across the barrier is simply proportional to the product of the initial and final spin-dependent densities of states at the Fermi level (figure 1.11). The first (second) FM electrode polarization is defined as

$$P = \frac{N_{i\uparrow}(E_F) - N_{i\downarrow}(E_F)}{N_{i\uparrow}(E_F) + N_{i\downarrow}(E_F)}, \qquad i = 1, 2 \tag{1.13}$$

where $N_{\uparrow,\downarrow}(E_F)$ are the densities of states at the Fermi level relative to the different spin orientations. The TMR signal is expressed as

$$TMR = \frac{R_{AP} - R_P}{R_P} = \frac{G_P - G_{AP}}{G_{AP}}, \tag{1.14}$$

and considering the conductance for the parallel and antiparallel state given by

$$G_P \propto N_{1\uparrow} N_{2\uparrow} + N_{1\downarrow} N_{2\downarrow}, \tag{1.15}$$

$$G_{AP} \propto N_{1\uparrow}N_{2\downarrow} + N_{1\downarrow}N_{2\uparrow}, \tag{1.16}$$

it results

$$TMR = \frac{2P_1P_2}{1 - P_1P_2}. \tag{1.17}$$

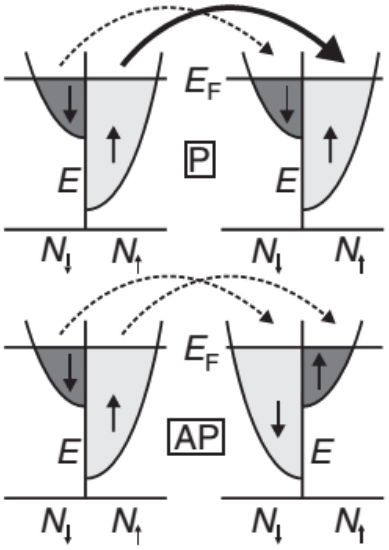

Figure 1.11: Schematic representation of a magnetic tunnel junction in the parallel (P) and antiparallel (AP) state. According to Julliere's model the transmission probability of electrons across the barrier depends only on the initial and final density of state at the Fermi level. The dashed (solid) arrow represents low (high) spin current.

MTJs have attracted great attention since 1994, when Moodera et al. [55] found MR values up 11.8% at room temperature in CoFe/AlOx/Co junctions. In 2004 Parking at al. [56] and Yuasa et al. [57] observed TMR values over 200% at room temperature in Fe/MgO/Fe junctions, confirming the theoretical predictions of Butler et al. [58] and Mathon et al. [59]. These works drove a rapid development of MTJs, which are now employed as read-heads of modern hard-disc drives and also in Magnetic-RAM (MRAM).

1.2.2 Giant Magnetoresistance

Giant magnetoresistance (GMR) effect is a large resistance variation depending on the relative magnetization of the FM electrodes in a multilayer device made of

alternating FM and NM metallic layers. It was discovered in an epitaxially grown Fe-Cr multilayer by Albert Fert [51], and independently by Peter Grunberg [52] in 1988. Their discovery was awarded by the 2007 Nobel Prize in physics and led to the development of spin-valve sensors and spintronics in general. The GMR underlying principles are still not completely understood. As in the case of TMR, it is also related to the DOS asymmetry between the FM electrodes, but in a more indirect fashion because electrons are injected in the NM spacer layer and its role cannot be neglected. We assume that spin-flip scattering is negligible in a ferromagnetic material

$$\tau_{\uparrow\downarrow}, \tau_{\downarrow\uparrow} \rightarrow \infty. \tag{1.18}$$

This turns out to be a very good approximation on the timescale of the dissipative processes that give rise to electrical resistivity [60]. This assumption allows one to treat their transport in terms of the two-channel model introduced by Mott [61]. Moreover we assume that all conductors are in the diffusive limit, i.e. the electron mean free path is much shorter than the typical dimensions of the conductors. Given these assumptions, and limiting the discussion to the most commonly used CPP (current perpendicular to plane) geometry (figure 1.12), the GMR effect can be qualitatively described as follows. When a FM electrode (injector) is connected to a NM material and a current is driven through the system, far from the interface on the magnetic side, the current is larger in one of the spin channels (conventionally the spin-up channel), while, far from the interface on the other side, it is equally distributed in the two channels. Spin-up electrons crossing the interface encounter a much higher barrier and accumulate on the FM side. Due to neutrality charge conservation, spin-down electrons are pushed towards the NM side and a finite magnetization builds up in the NM material, which is known as spin accumulation [63]. The spin accumulation is defined as the difference between the electrochemical potential for spin-up electrons, $\mu_{\uparrow}$, and that for spin-down electrons, $\mu_{\downarrow}$. The magnitude of the spin accumulation depends on the spin injection rate into the normal material and the spin relaxation time, and it decays exponentially away from the injecting contact on a length scale set by the spin relaxation length l_s

$$\mu_{\uparrow} - \mu_{\downarrow} \propto exp(-l/l_s) \tag{1.19}$$

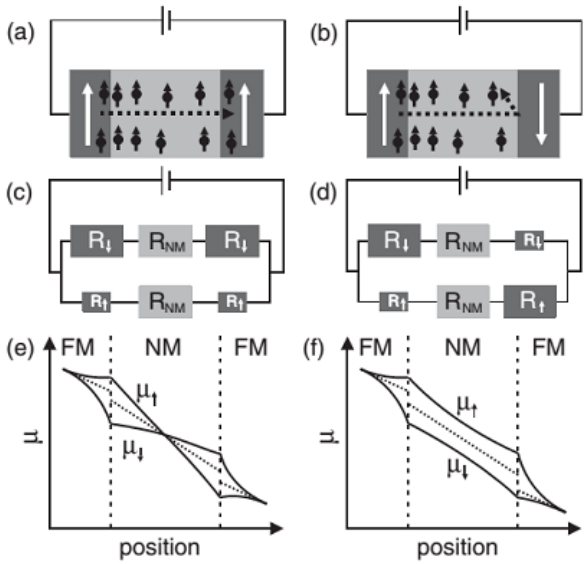

Figure 1.12: Schematic representation of a CPP GMR device consisting of two FM electrodes (dark grey) separated by a spacer (light grey) for the P (a) and AP configuration (b). The magnetization of the FM electrodes is denoted by the white arrows. The black arrows represent the spin current. The corresponding resistor model is given for the P (c) and AP configuration (d). The colours correspond to the layers in (a) and (b), and bigger resistors represent a larger resistance for the denoted spin species. The electrochemical potentials μ for the two spin species are given for the P (e) and AP (f) configuration. The dotted lines are the asymptotes of the electrochemical potentials to which they would collapse at large distances. The dashed lines correspond to the interfaces in (a) and (b) [62].

where l is the distance from the injecting contact. The net spin density resulting from the spin accumulation is typically orders of magnitude smaller than the charge density in the NM layer. However, it can be probed by a second FM electrode, the spin detector, if it is placed at a distance smaller or comparable to the spin relaxation length from the spin injector. The transmission will be largest when the magnetization of the detector contact is parallel to the net spin accumulated at its interface (figures 1.12 (a) and (b)). CPP GMR is often described in terms of a parallel resistor model, as shown in figures 1.12 (c) and (d). When the ferromagnetic layers are magnetically aligned spin-up electrons cross the device without experiencing scattering while spin-down electrons undergo scattering with higher

probability, and the device resistance can be expressed as

$$\frac{1}{R_P} = \frac{1}{2R_\uparrow} + \frac{1}{2R_\downarrow}. \tag{1.20}$$

When the ferromagnetic layers are antiparallel spin-up and spin-down electrons undergo scattering with the same probability and the resistance is expressed by

$$\frac{1}{R_{AP}} = \frac{1}{R_\uparrow + R_\downarrow} + \frac{1}{R_\uparrow + R_\downarrow}. \tag{1.21}$$

Thus

$$R_{AP} = \frac{R_\uparrow + R_\downarrow}{2} > R_P = \frac{2R_\uparrow R_\downarrow}{R_\uparrow + R_\downarrow}. \tag{1.22}$$

A more thorough theoretical description of CPP GMR, based on the Boltzmann equation, has been provided by Valet and Fert [64]. With their model, the electrochemical potentials of the two spin species can be calculated, as illustrated in figures 1.12 (e) and (f). It reveals the splitting of the electrochemical potentials at the interfaces of the FM electroode and NM material. It also shows the different voltage drop (represented by the discontinuity of the asymptote) at the interfaces for the P and AP configuration, which leads to the difference in resistance between these two cases. This models assume a negligible interface resistance, actually the interface potential barrier between adjacent layers should be considered.

Spin valve devices

Spin valve devices are the most common application of GMR effect, consisting in a thin-film stack with just two FM layers. The first one is pinned by exchange coupling to an adjacent antiferromagnetic (AFM) layer, while the other, the free layer, is able to rotate with as little coercivity as possible. The device resistance changes when the magnetization of the free layer is switched relative to the other. A pseudo spin valve device (often referred to simply as spin valve) can be obtained simply sandwiching a non magnetic layer between two ferromagnetic electrodes with different coercive fields. This is the device structure employed in this work. Figure 1.13 schematically shows its working principle. Starting from high applied field, the electrodes assume a parallel configuration corresponding to the R_P resistive state. When the magnetization of the first electrode is reversed, the electrodes assume an antiparallel configuration and the device resistance jump to the value R_{AP}. Finally, reaching the second coercive field, the parallel configuration is restored together with the original resistance.

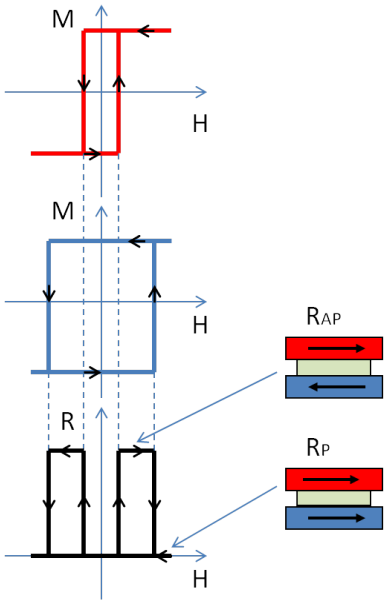

Figure 1.13: Schematic representation of electrode hysteresis loop and MR curve of a spin valve device. At high magnetic field the top electrode (red line) and the bottom electrode (blue line) magnetic moments are aligned and the device is set in the low resistance parallel configuration R_P. When the top electrode magnetization is reversed the device is switched in a high resistance state antiparallel configuration R_{AP}. Finally, when the bottom electrode moment is also reversed, the parallel configuration is restored.

The conductivity mismatch problem

The problem of conductivity mismatch was raised by Schmidt et al. [54]. They showed that, in the diffusive transport regime, for typical ferromagnets only a current with small spin-polarization can be injected into a semiconductor (described as a two dimensional electron gas) with long spin-flip length even if the conductivities of semiconductor and ferromagnet are equal. If the semiconductor resistance is much larger than the ferromagnetic metal injector then the spin-polarization in the semiconductor becomes negligible. This is due to the much larger density of states in the metal with respect to the semiconductor, which leads to a larger spin accumulation density and number of spin flips on the metallic side. The polarization is therefore faster on the metallic side and the current is almost completely depolarized when it enters the semiconductor [65]. Several groups [66, 67] showed that the problems can be solved by introducing a spin-dependent interface resi-

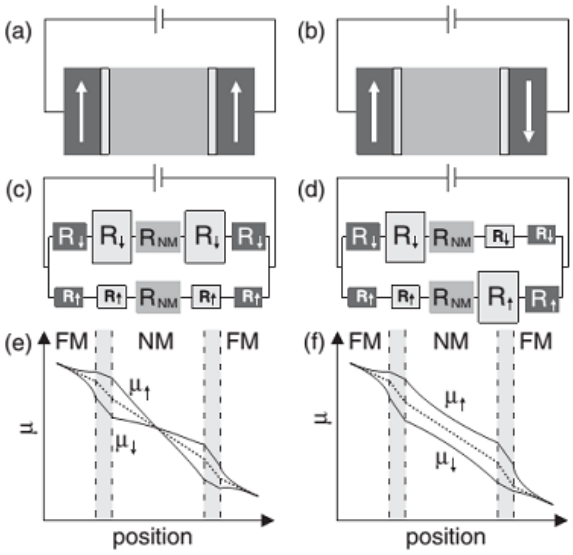

Figure 1.14: Schematic representation of a CPP GMR device consisting of two FM electrodes (dark grey) separated by a spacer (light grey) and tunnel barriers (light grey with black outline) for the P (a) and AP configuration (b). The corresponding resistor model is given for the P (c) and AP configuration (d). The electrochemical potentials μ for the different spin species are given for the P (e) and AP configuration (f). The dotted lines are the asymptotes of the electrochemical potentials to which they would collapse at large distances. The dashed lines correspond to the interfaces in (a) and (b) [62].

stance, typically a tunnel junction (figure 1.14), to introduce a discontinuity of the spin accumulation at the interface and shift the depolarization from the metallic to the semiconductor side. Spin injection through a tunnel barrier has now been achieved successfully in several experiments but the tunnel resistances are generally too large for an efficient transformation of the spin information into an electrical signal [68].

1.2.3 Spin relaxation in NM spacer layer

While, according to the Jullière's model, the TMR depends only on the density of states of the FM electrodes, the GMR requires spin transport across the spacer layer. The spin relaxation length in the non magnetic layer is thus a crucial parameter. In general, one can distinguish two classes of spin relaxation. The first one describes the decay of a net spin component along the axis of spin quantization,

let's say the z-axis. The z-component (or longitudinal component) of the total spin S_z decays exponentially to equilibrium due to individual spin-flips on a time scale T_1, defined by the spin relaxation time

$$\frac{1}{\tau_s} = \frac{1}{\tau_{\uparrow\downarrow}} + \frac{1}{\tau_{\downarrow\uparrow}}, \tag{1.23}$$

where the spin-flip time $\tau_{\uparrow\downarrow}$ indicates the average time for an up-spin to flip to a down-spin, and $\tau_{\downarrow\uparrow}$ for the reverse process. The spin relaxation length l_s is related to τ_s in a different way depending on the material. In the case of a NM metal or a degenerate Fermi gas semiconductor [69]:

$$l_s = \sqrt{\frac{\tau_s}{4e^2 N(E_F)\rho_N}}, \tag{1.24}$$

where $N(E_F)$ is the density of states (DOS) at the Fermi level E_F, and ρ_N the resistivity of the NM spacer material. For a semiconductor in the non-degenerate regime [70]:

$$l_s = \sqrt{\frac{k_B T \tau_s}{2e^2 \rho_N}}. \tag{1.25}$$

The condition

$$d << l_s, \tag{1.26}$$

where d is the thickness of the spacer layer, must be fulfilled for a spin valve device to work properly for a spin valve device to work properly. As the z-component decay process requires energy exchange with the environment, it is a rather slow process [71]. There is a second process, however, that does not require energy exchange and affects the spin component perpendicular to the quantization axis, i.e. the transverse component $S_\perp$. This process affects the quantum-mechanical phase of individual spins and leads to loss of coherence on a time scale T_2. For different spins within an ensemble the phases are in general affected unequally, which results in the spins getting out of phase, an effect referred to as inhomogeneous broadening. The timescale related to this process of ensemble dephasing is often denoted as T_2^* [72], and usually $T_2^* < T_2$. The time evolution of a spin ensemble with total spin $\mathbf{S}$ in an external magnetic field B along the z-axis can then be described by the Bloch equations

$$\frac{dS_z}{dt} = \gamma(\mathbf{B} \times \mathbf{S})_z - (S - S_z)/T_1 \tag{1.27}$$

$$\frac{dS_\perp}{dt} = \gamma(\mathbf{B} \times \mathbf{S})_\perp - (S - S_\perp)/T_2^*, \tag{1.28}$$

where γ is the gyromagnetic ratio. The underlying mechanisms for spin relaxation in solids can be divided in mechanisms related to spin-orbit coupling and to hyperfine interaction. Spin-orbit coupling is a relativistic effect, describing the interaction between the electron's spin and its orbital motion around an atomic nucleus. More generally, spin-orbit coupling occurs whenever a particle with non-zero spin moves in a region with a finite electric field. Three different spin-orbit-coupling-related spin relaxation mechanisms can be distinguished in non-magnetic solids: Elliot-Yafet (EY), D'yakonov-Perel (DP), and Bir-Aronov-Pikus (BAP) [71]. The EY mechanism [73] consists in the relaxation of a conduction electron spin via ordinary momentum scattering (mainly caused by impurities at low temperature and phonons at high temperature [74]), if the lattice ions induce spin-orbit coupling in the electron wave function. This leads to a spin relaxation time τ_s that is proportional to the momentum scattering time τ_p. The DP [75] mechanism arises when the solid lacks a center of symmetry. Without inversion symmetry the momentum states of the spin-up and spin-down electrons are not degenerate: $E_{\mathbf{k}} \neq E_{\text{-}\mathbf{k}}$. Spin splittings induced by inversion asymmetry is described by introducing an intrinsic $\mathbf{k}$-dependent magnetic field $\mathrm{B}_i(\mathbf{k})$ around which electron spins precess with Larmor frequency $\omega(\mathbf{k}) = (e/m)B_i(\mathbf{k})$. The momentum-dependent spin precession, together with the momentum scattering characterized by momentum relaxation time τ_p, leads to spin dephasing. Heavy scattering slows down the spin relaxation because the spin cannot follow the internal magnetic field when it changes too rapidly. Therefore, the spin relaxation time is inversely proportional to the scattering time, contrary to the EY mechanism. The BAP [76] mechanism affects p-doped semiconductors, where spin relaxation of conduction electrons can also proceed through scattering, accompanied by spin exchange, with holes. The other source for spin relaxation is the hyperfine interaction. This magnetic interaction between the spins of electrons and nuclei of the host material provides an important mechanism [77] for ensemble spin dephasing and single-spin decoherence of localized electrons, such as those confined in quantum dots or bound on donors [71]. In general, the electron spin interacts with many nuclear spins, and the statistical fluctuation scales with with inverse of the nuclear spin number $1/\sqrt{N}$ [78]. Hence the more delocalized the electron wave function is, the less the

electron is influenced by the nuclei. For this reason the hyperfine interaction is too weak to cause effective spin relaxation of free electrons in metals or in bulk inorganic semiconductors.

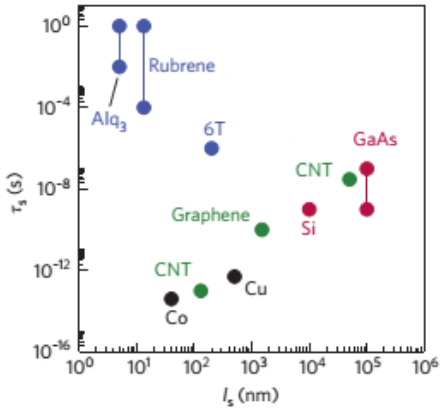

Figure 1.15: Spin-diffusion length l_s versus spin diffusion time τ_s for various materials. The organic semiconductors appear in the top-left corner. They have a long spin lifetime but, owing to their low mobilities, spin-diffusion lengths are short. Taken from Ref. [79], where the references for the plotted data are reported.

Since the spin valves studied in this thesis have an organic spacer layer, I am interested in the spin relaxation mechanisms in organic semiconductors. These materials have attracted the attention of the spintronic community because of their potentially very long spin relaxation times [80]. In fact, since spin-orbit coupling generally grows with atomic number Z (it scales as Z^4 in the case of an hydrogen-like atom [81]) and they consist mainly of low-Z materials (in particular C), they are expected to have a low spin orbit coupling. However, as pointed out by Yu [82], caution must be taken when making general statements on the SOC in organics, because values can differ by orders of magnitude. The nuclear spins in organic materials are mainly originating from the isotopes ^{1}H ($I = 1/2$), ^{13}C ($I = 1/2$), and ^{14}N ($I = 1/2$) and the hyperfine interaction is usually weak because the delocalized states of π-conjugated molecules have practically no overlap with the C or H atoms. For this reason the nuclear spin effectively experienced by the conduction electrons can be neglected [81]. Electron paramagnetic resonance (EPR) measurements effectively revealed room-temperature spin relaxation times in the range 10^{-7}–10^{-5} s [83] for many organic materials, compared to 10^{-10} s

in metals [84]. However, as pointed out by Szulczewski et al. [79], it does not necessarily imply a long spin-diffusion lengths, due to their low electrical mobilities (figure 1.15). Here I report some estimated and measured values for the spin diffusion length in Alq3, since it is the material used for the spacer layer of our spin valves. Yu [82] used ab initio approach to study the effects of SOC on the polaronic regime, finding $l_s = 11.2$ nm for electron polaron and $l_s = 60$ nm for hole polaron. Bobbert et al. [85] presented a theory for spin diffusion in disordered organic semiconductors, based on incoherent hopping of a charge carrier and coherent precession of its spin in an effective magnetic field, composed of the random hyperfine field of hydrogen nuclei and an applied magnetic field. They claim that their estimated spin diffusion lengths are compatible with the experimental values (about 10-100 nm) derived from MR measurements [1, 2, 86] and muon spin-resonance studies [8]

1.2.4 $La_{0.7}Sr_{0.3}MnO_3$: a half-metal for spintronics

A half-metallic ferromagnet is a metal that has an energy gap at the Fermi level E_F in one of the two spin channels (figure 1.16). Only the other channel has states available for transport, and thus the electric current is fully spin-polarized. Half-

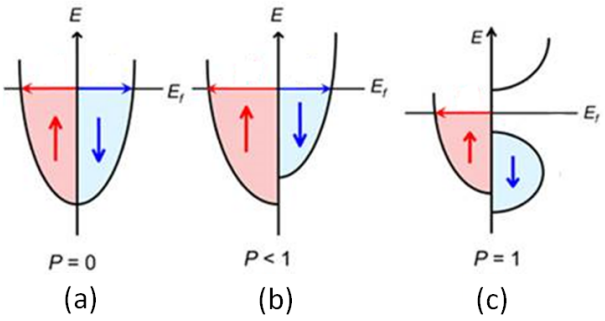

Figure 1.16: Schematic representation of the density of states in (a) non-magnetic (NM) metals, (b) ferromagnetic (FM) metals, and (c) half-metallic ferromagnets (HM). In HM only spin up states are available at the Fermi level, and thus the conduction electrons are fully spin-polarized.

metallic or other highly spin-polarized metals are strongly requested in spintronics, since device performance improves dramatically as the spin polarization of the metal approaches 100 % [87]. Perovskite manganites $La_{1-x}D_xMnO_3$, with D=Ca, Sr, or Ba, have attracted much interest due to the high spin polarization, predicted

theoretically [88] and observed experimentally by several techniques [89, 90, 91]. In particular in this paragraph I will focus on $La_{0.7}Sr_{0.3}MnO_3$ (LSMO), which has been employed as bottom electrode of our device. In 1950 Jonker and van Santen [92] discovered a striking correlation between magnetic order and conductivity in these systems. At the end points x=0 and x=1 the alloys are insulating and antiferromagnetic (AFM), but in the $0.2 < x < 0.5$ region they are ferromagnetic (FM) and their conductivity at low temperature is better described as metallic (figure 1.17). Zener [94] identified a double exchange process to explain this

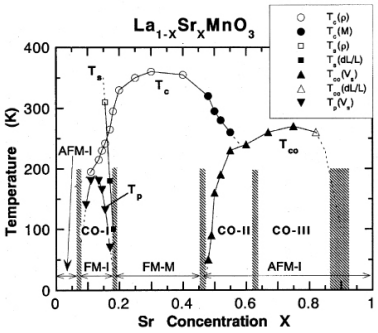

Figure 1.17: LSMO fase diagram shows that transport and magnetic properties are function of Sr ions fraction. In the range $0.2 \leq x \leq 0.5$ the compound becomes ferromagnetic and metallic under a Curie temperature near room temperature [93].

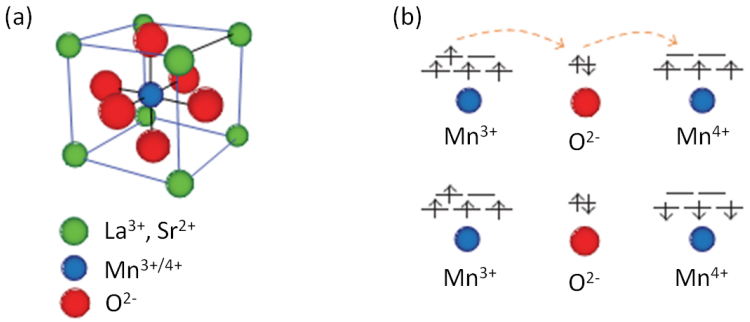

Figure 1.18: (a) Crystal structure of the perovskite manganite LSMO. (b) Schematic representation of the double exchange mechanism described in the text.

behavior, schematically illustrated in figure 1.18b. In Zener's picture, the oxygen ion is closed shell (O^{2-}), but somehow hopping must occur via this ion. This can

happen if an electron jumps onto a Mn^{4+} ion (on its right, say) simultaneously with an electron hopping onto the oxygen ion from the Mn^{3+} on the left. This double hopping event requires that both hopping electrons have the same spin, that of the active spin orbital on the oxygen ion. If in addition the Mn ions are presumed to be "Hund's rule" ions in which all electron spins are aligned, then the hopping event requires both Mn ions to have parallel moments. This mechanism necessarily connects the parallel alignment of Mn moments (ferromagnetism) with hopping of carriers (metallic conduction) and nicely accounts for the experimental observation. The result is an effective positive exchange coupling induced by the carriers, named "double exchange" to contrast it with direct exchange and superexchange [88]. LSMO shows Colossal Magneto Resistance (CMR) at high magnetic fields (figure 1.19), a large field-induced variation of the resistance well studied in the past years [95, 96]. The effect is generally attributed to the double exchange mechanism in conjunction with the effects of a Jahn-Teller lattice distortion [97].

Despite the impressive magnitude of the resistance change, CMR is of limited

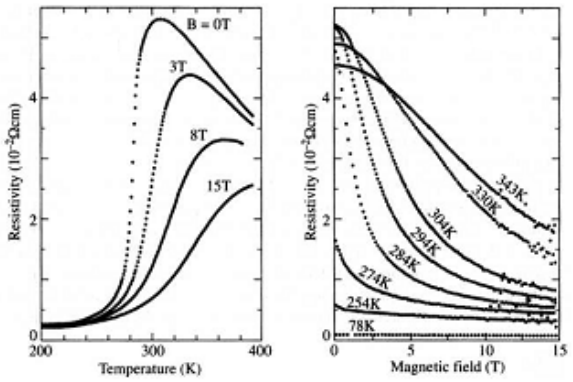

Figure 1.19: LSMO resistivity (a) as a function of temperature at different magnetic field applied and (b) as a function of magnetic field at different temperature [98].

use because of the huge fields needed to create it. For this reason reducing the field scale has been the goal of a number of research groups. Low field magnetoresistance effects have been found both in polycrystalline [100, 99] and epitaxially grown single-crystal LSMO films [99, 101, 102, 103, 104]. In polycrystalline films a MR up to 15% has been observed (figure 1.20a) at low temperature and it has been explained as the result of a spin dependent scattering at the grain boundary [99] or

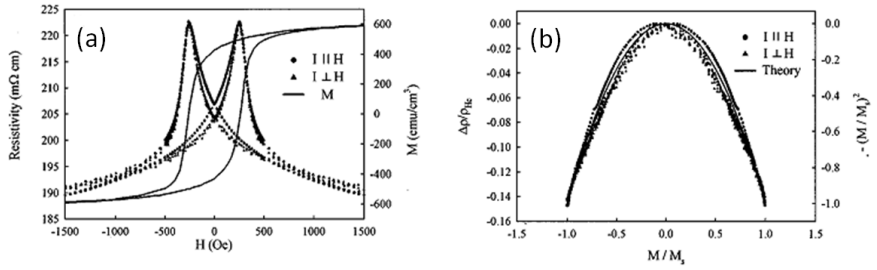

Figure 1.20: (a) MR as a function of magnetic field, measured at 10 K, for a 3 μm average grain size LCMO film for both field-parallel and field-perpendicular alignments. The magnetic hysteresis loop for the sample obtained at the same temperature using a SQUID magnetometer is also plotted. (b) MR vs magnetization ratio M/Ms for the above film. The solid curve is the $(M/M_S)^2$ fit as discussed in the text [99].

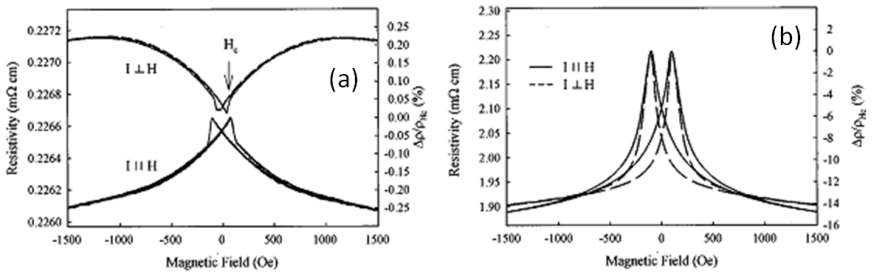

Figure 1.21: Comparison between the MR hysteresis loops of (a) epitaxial LSMO, and (b) polycrystalline LSMO film with 14 μm average grain size. Measurements are taken at 4.2 K for both current parallel to the field (I||H) and perpendicular to the field (I⊥H) are shown [99]. While AMR effect is clearly observable in the epitaxial film, it is not significant for the polycrystalline sample.

alternatively of an intergrain spin-polarized tunneling [100]. In both the scattering and the tunneling models, the resistivity ρ is expected to have a maximum at the coercive field and decrease as the relative orientation of the magnetization between grains changes with the application of a field, as observed. Also the expectation for the MR to be proportional to $(M/M_S)^2$, where M_S is the saturation magnetization, is fulfilled by the experimental curves (figure 1.20b). In epitaxial films usually a modest change in ρ (MR<1%) is observed, with a rather sharp drop from the peak value followed by a more gradual decrease at higher fields(figure 1.21a). A positive

MR is observed when I||H as opposed to a negative MR when I⊥H, indicating an anisotropic magnetoresistance (AMR) mechanism. A similar AMR behavior has been reported by O'Donnell et al. [101] for epitaxial LCMO films. They also pointed out that the magnetocrystalline anisotropy (MCA) plays a crucial role and the low-field magnetoresistance is given by a superposition of the two effects. In figure 1.21 a comparison between policrystalline and epitaxial film is shown.

1.3 Organic Spintronics

Organic spintronics is an emerging research field where organic semiconductors are applied as a medium to transport and control spin-polarized signals, with the aim to combine the advantages of organic electronics and spintronics. On the one hand, the organic materials open the way to cheap, low-weight, mechanically flexible, and bottom-up fabricated electronics. On the other hand, the control of the electron's spin (instead of or in addition to its charge), allows for non-volatile resistance devices, in which logic operations, storage and communication can be combined [45]. As mentioned above in paragraph 1.15 organic semiconductors are generally characterized by a low spin-orbit coupling and a weak hyperfine interaction, which results in a long spin relaxation time. For this reason they are in principle suitable materials for spintronics. Organic-based spin valve devices showing MR have been obtained by several groups [1, 2, 105, 106, 107], and the main results are summarized in the overview given below (paragraph 1.3.1). Moreover spin injection from a ferromagnetic electrode into an organic semiconductor was demonstrated by two-photon photoemission spectroscopy [7] and muon spin rotation [8] techniques as briefly described in paragraph 1.3.3. However it is still debated if the observed spin-valve signals should be attributed to spin injection and transport in the OSC [2, 108] or to tunneling through locally thin regions in the spacer layer [106, 109]. MR, indeed, cannot be unambiguously related to spin injection unless the Hanle effect is detected, as argued by several groups [9, 110] (see paragraph 1.3.2).

1.3.1 Organic spin valves: a brief overview

The first report on a magnetoresistive organic-based device was by Dediu et al. [1] in 2002. They studied a LSMO/T6/LSMO planar junction. LSMO elec-

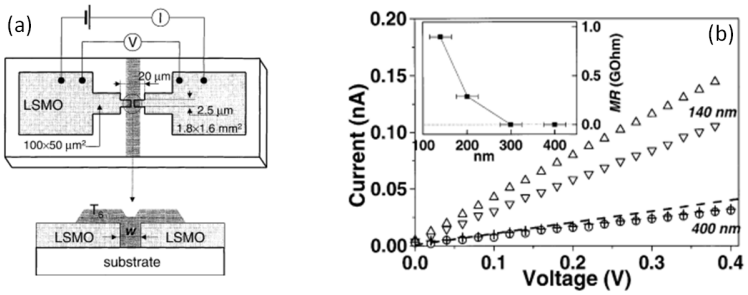

Figure 1.22: (a) Schematic top view and cross section of a hybrid LSMO/T6/LSMO junction. An epitaxial thin film of LSMO is deposited on matching substrates ($NdGaO_3$, $SrTiO_3$), and electrodes are fabricated by EB lithography. The separation w between the electrodes varies between 70 and 500 nm. T6 films (100-150 nm thick) are deposited on top of the electrodes by molecular beam deposition. (b) I-V characteristics as a function of the magnetic field H for 140 nm and 400 nm channel length w. Down triangle and circles correspond to H=0, while up triangles and crosses to H=3.4 kOe. The dashed line represents the expected slope for w=400 nm as calculated from the 140 nm junction assuming a linear resistance increase versus channel length. In the inset is reported the MR, defined as MR=R(0)-R(3.4 kOe), as a function of w [1].

trodes, nearly 100 nm thick, were fabricated by electron beam litography, and the sexithienyl (T6), a π-conjugated oligomer with a mobility ranging from 10^{-2} to 10^{-4} $cm^2V^{-1}s^{-1}$, was evaporated on top (figure 1.22a). As the geometry (and hence the coercive field) of the LSMO electrodes is the same, they did not succeed in switching the magnetization of each FM contact independently. However, they change the relative orientation from random, at low field, to parallel at higher field. A maximum resistance decrease of about 30 % from the random to the parallel configuration was observed at room temperature for a 140 nm channel, while no MR effect is observed for channels larger than 200 nm (figure 1.22b). It should be pointed out that the MR signal does not depend on the relative orientation between the applied field and the current.

In 2004 Xiong et al. [2] succeeded in fabricating a vertical organic device clearly showing a spin valve signal, with the resistance switching between the parallel and antiparallel magnetization state of the electrodes. They used the small π-conjugated molecule 8-hydroxy-quinoline aluminum (Alq3) as a spacer layer, sandwiched between a LSMO and a Co electrodes (figure 1.23a). A negative MR of 40% was observed at 11 K for a d=130 nm thick organic layer (figure 1.23b), vanishing be-

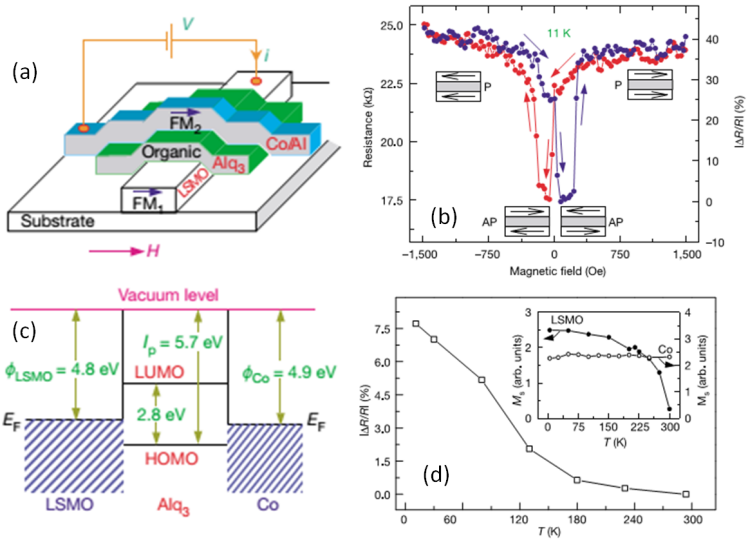

Figure 1.23: (a) Schematic representation of the device studied by Xiong et al. [2]. (b) GMR loop of a LSMO (100 nm)/Alq3(130 nm)/Co (3.5 nm) spin-valve device measured at 11 K. The blue (red) curve denotes GMR measurements made while increasing (decreasing)H. The insets schematically represent anti-parallel (AP) and parallel (P) configurations. (c) Schematic band diagram of the device reported in (a) in the rigid band approximation showing the Fermi levels and the work functions of the two FM electrodes, LSMO and Co, respectively, and the HOMO-LUMO levels of Alq3. (d) Temperature dependence of the device MR. The inset shows the temperature dependence of the electrode magnetization as a comparison [2].

low room temperature (figure 1.23d). A good conductivity was observed in these devices, despite the very low mobility values reported in literature for Alq3 (about 10^{-5} $cm^2V^{-1}s^{-1}$ for electrons and 10^{-6} $cm^2V^{-1}s^{-1}$ for holes [111]) and no injection barrier has been observed. This is not compatible with the schematic band diagram (figure 1.23c) reported, assuming holes injection from the anode Fermi level into the near HOMO level of the molecule through a tunnel barrier. The authors also pointed out that the evaporation of the top Co electrode causes pinholes and Co inclusions in the Alq3 layer over a distance d_0 of about 100 nm. Despite the ill-defined Co/Alq3 interface, an attempt to estimate the spin diffusion length l_s in organic layer was made by using a simple injection and diffusion model by using an extension of the Jullière model for magneto tunnel junction. Assuming no loss of spin memory at the Co/Alq3 interface and an exponential decay in the

$d - d_0$ neat region, the relative magnetoresistance is given by

$$\frac{\Delta R}{R} = \frac{R_{AP} - R_P}{R_P} = \frac{2P_1P_2e^{-(d-d_0)/l_s}}{1 - P_1P_2e^{-(d-d_0)/l_s}} \tag{1.29}$$

where P_1 and P_2 are the spin polarization of the FM electrodes. Considering P_1P_2=-0.32 and d_0=87 nm it was obtained l_s=45 nm at 11 K. The same model has been used also by Pramanik et al. [86] to estimate l_s in organic nanowire spin valve where a 30 nm thick Alq3 layer is sandwiched between cobalt and nickel electrodes. In this case they assume d-$d_0 \approx d$ and values up to 6 nm have obtained at low temperature. For the first time they addressed the question which spin relaxation mechanism is dominant in organic semiconductors, indicating the Elliott-Yafet mode as the primary.

After the pioneering work of Xiong et al. [2], the inversion of the spin-valve effect has been detected in LSMO/Alq3/Co devices by many other groups [112, 106, 113]. The effect has also has been observed in LSMO/Alq3/Al_2O_3/Co [107] and LSMO/Alq3/LiF/Co [37] devices showing that is independent of the material combination at the top interface. While at the beginning the negative MR was ascribed to the negative spin polarization of the Co d-band [2] the available knowledge on the spin polarization at both interfaces seriously contradicts the negative-MR data. It has been demonstrated that Co injects majority (up) spins for both Co/Alq3 and Co/Al_2O_3/Alq3 interfaces and manganites such as LSMO are widely accepted as majority (spin up) injectors [45]. A model was proposed for n-type OSC by Dediu et al. [107] which accepts the positive sign of the spin polarization for carriers coming from both LSMO and Co. However this widely reproduced inversion effect remains an open question for the organic spintronics.

The temperature dependence of the MR in LSMO/Alq3/Co has been investigated by several groups [106, 107, 112, 37, 114] and initially a maximum working temperature in the 210-250 K region was reported (blue and red makers in figure 1.24). An attempt to surpass this temperature range was performed by substituting LSMO with a high-temperature ferromagnetic element such as Fe [115]. Unfortunately, the temperature at which MR was recorded was even lower. In 2008 Dediu et al. [107] observed room-temperature MR in LSMO/Alq3/Al_2O_3/Co devices by improving the quality of both injecting interfaces, especially the top one, in which a thin insulating layer was added (green circles in figure 1.24). Moreover a comparative study [114] of various OSCs (Alq3, α-NPD, CVB) with a fixed set of

magnetic electrodes (LSMO and Co) has produced quite similar results for each of the materials studied: inverse spin-valve effect (around 10 % at low temperatures) and fast decrease of the MR with increasing temperature, vanishing between 210-240 K. It has been pointed out [114, 107] that MR decreases with tempera-

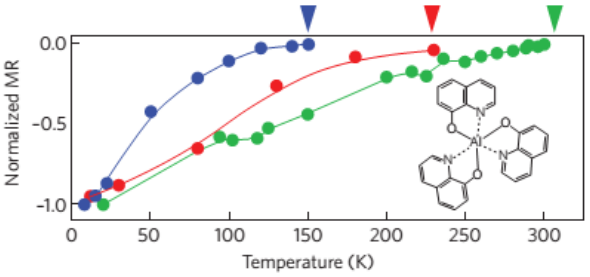

Figure 1.24: Temperature dependence of the normalized MR of different Alq3-based SV devices with LSMO and Co as magnetic electrodes. The reported spacer layer thicknesses are 130 nm (blue) [112], 160 nm (red) [114] and 100 nm [107]. Arrows indicate the temperature at which the corresponding MR signal goes to zero [45].

ture following exactly the surface magnetization of LSMO reported by Park et al. [90] and vanishing at its T_C. This behavior seems to indicate that the temperature dependence of these devices is completely dominated by the injection process, and the corresponding temperature dependence of the spin-transport losses inside OSCs must be very weak. Furthermore, the presence of an injection-dominated electronic-transport regime could partially explain the random thickness dependence of the MR reported in some articles [106, 113]. Other groups refuse this explanation, attributing the temperature dependence of the MR to spin relaxation into the OSC [8].

While the interest in spin injection and long-distance spin transport in organic semiconductors was growing, several groups also started to explore the possibilities of these materials as spin-tunnel barriers [45]. In 2004 Petta et al. [116] demonstrate spin-polarized tunneling trough an organic semiconductor fabricating Ni/octanethiol/Ni vertical tunnelling devices in a nanopore geometry with an octanethiol self-assembled monolayer. These devices showed MR up to 16% at 4.2 K, which vanished at about 30 K. The sign of the MR was observed to switch from positive to negative for different voltage values, but also from sample to sample at

the same voltage.
MR has been detected also in devices with a Langmuir-Blodgett monolayer film as the tunnel barrier [117, 118]. However, the presence of a continuous organic monolayer confined between the two ferromagnetic electrodes was not convincingly demonstrated, leaving the nature of the observed magnetoresistive effects open to question.
An important step forward for organic spin tunneling was the fabrication of devices by direct in situ UHV organic vapour deposition with shadow masking. Santos et al. [105] fabricated Co/Al_2O_3/Alq3/NiFe vertical tunneling devices (figure 1.25a). A positive TMR around 15% was recorded at 4.2 K, with a few percent still present at room temperature (figure 1.25b).

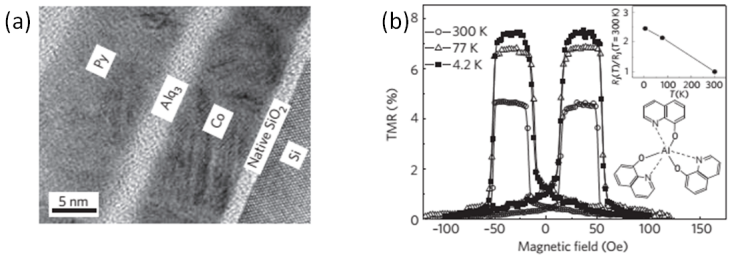

Figure 1.25: (a) Cross-sectional High Resolution TEM image of a MTJ, showing the continuous Alq3 barrier. (b) TMR for an Co(8 nm)/Al_2O_3(0.6 nm)/Alq3(1.6 nm)/Py(10 nm) junction measured with 10 mV bias. The inset shows the temperature dependence of R_J for this junction and the chemical structure of the Alq3 molecule [105].

It must be mentioned that some groups interpreted as tunneling also transport across thick organic layers, essentially by claiming transport only through defects in the organic layer [106, 119, 109].
This brief overview makes clear that a full understanding of the spintronic effects involved in OSC devices is still lacking. The most controversial issue is the low reproducibility of the published experimental results. For example, let's focus our attention on Alq3, the most popular OSC for spintronic applications. It should be noted that inverse MR is a well established result for the LSMO/Alq3/Co structure, both for groups claiming injection in the spacer layer [2, 108, 107] and for groups claiming tunneling between the two ferromagnetic electrodes [106, 119, 109]. At the same time positive MR values have been reported in tunneling devices [105]

and injection devices [120]. In addition, the device resistances obtained by different groups spread over several orders of magnitude, and an accurate comparative assessment is often prevented by the lack of information on such important device parameters as I-V curves, mobility, injection barriers and operating voltages, among others. Moreover, even when data are available, the theoretical models generally used to describe organic electronic and optoelectronic devices (Injection Limited Current, Space Charge Limited Current, Trap Charge Limited Current) often can not be applied, due to incompatible I-V curves and temperature dependence of the device resistance. So, in parallel with spin-transport studies, simpler charge transport also needs a deeper understanding. All these considerations indicate that the organic spintronics community should make an effort to elaborate common metrology rules to allow direct comparisons between different experiments and open a serious discussion about these controversial results and future challenges.

1.3.2 Hanle effect as a proof of spin transport in organic layer

MR signals have been measured in vertical organic spin valves by many groups [2, 105, 106, 107] and also injection of spin polarized electrons into the OSC layer has been detected by 2PPE spectroscopy and muon spin rotation techniques [7, 8]. However these experiments do not prove that spin injection is the cause of an electrical spin valve signal. MR can indeed arise due to other effects, such as tunnel through locally thin region of the organic barrier or fringe fields perturbation [121, 122, 106]. The detection of the Hanle effect has been accepted as the only reliable proof that a link exist between spin polarized injection into the OSC layer and the spin valve signal [123, 124, 53, 125]. The Hanle effect consists in the modulation and suppression of the MR signal due to precession and dephasing of spins in the presence of a magnetic field applied out of the device plane (figure 1.26a). It has been detected in metallic and inorganic semiconductor-based spin valves [126, 53, 125], and it was shown that the drift-diffusion model developed by Johnson and Silsbee [124] can be successfully employed to quantitatively study the effect. Let's consider an oblique magnetic field $\mathbf{B} = B_z\hat{z} + B_y\hat{y}$, where $\hat{z}$ indicates the axis perpendicular to the device plane while $\hat{y}$ is oriented in the device plane along the injector/detector magnetization. The spins of electrons traveling

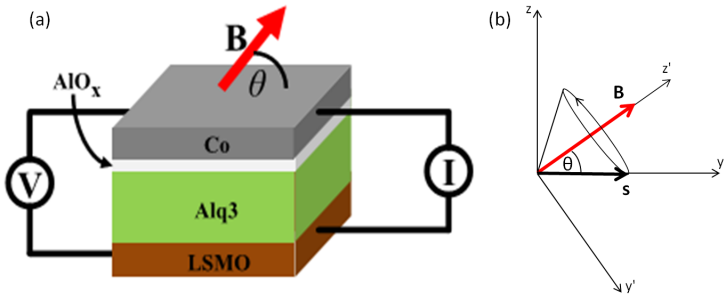

Figure 1.26: (a) Schematic of a studied spin valve with a out-of-plane magnetic field applied [9]. Vectorial representation of the applied magnetic field and electron spin. Spin precession around the field axis is indicated.

from an electrode to the other will precess around the field axis at the Larmor frequency

$$\omega_L = \frac{egB}{2m_e} \tag{1.30}$$

as illustrated in figure 1.26b. In Cartesian (x',y',z') coordinates, with the field B along z', the initial spin direction at the injector is $\mathbf{s_i}$=(0, sin θ, cos θ), where θ is the angle between the field and the injector magnetization. After precession over a transit time t, the final spin direction will be $\mathbf{s_f}$=(sin θ sin $\omega_L t$, sin θ cos $\omega_L t$, cos θ). The spin detector output is assumed to be proportional to the projection of final spin direction on the detector magnetization axis. Therefore, if the injector and detector are in the parallel configuration, the contribution from a single precessing electron is given by $\mathbf{s_i} \cdot \mathbf{s_f}$=sin$^2\theta$ cos $\omega_L t$+ cos$^2\theta$. Considering the random walk induced by diffusion, the expected total spin signal is the sum of all the projection contributions at different arrival times, weighted by the arrival time distribution:

$$GMR \propto \int_0^{+\infty} \frac{1}{\sqrt{4\pi Dt}} \cdot e^{-\frac{(d-vt)^2}{4Dt}} \cdot [sin^2\theta cos(\omega_L t) + cos^2\theta] e^{-t/t_s} dt, \tag{1.31}$$

where D is the diffusion constant, d the spacer layer thickness, and t$_s$ the spin lifetime. In materials in which the spin transport occurs rather incoherently (the variation of the transit time t_{trans} is large), spin dephasing can already be observed at small B$_z$ resulting in a quenching of the magnetoresistance i.e. a decrease of the difference between the resistances in the parallel (P) and antiparallel (AP) state (figure 1.27). In case of coherent spin transport, each precession can be observed as an oscillation in the resistance as a function of the applied magnetic field [127] while

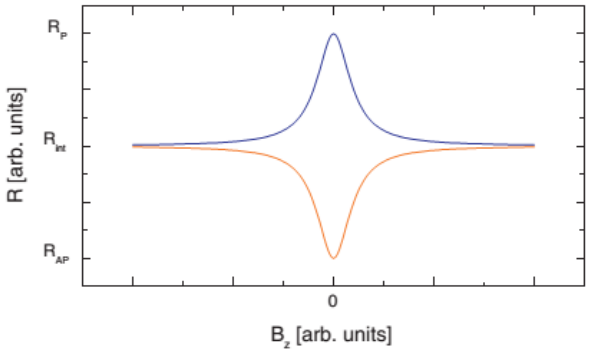

Figure 1.27: Theoretical traces of a device's resistance during experiments in a perpendicular magnetic field B_z for the previously prepared parallel (blue curve) and antiparallel (orange curve) spin valve configuration assuming incoherent transport. Here is represented the case of a negative MR ($R_{AP}<R_P$). As shown, the difference between the two curves is expected to decrease with increasing B_z [110].

large B_z must be applied in order to observe a decrease of the magnetoresistance. Charge transport in organic semiconductors takes place by hopping [128] and is highly incoherent. Therefore the former behavior is expected. However no change of the magnetoresistance as a function of B_z has been detected in organic spin valves, yet [110, 9]. In this work LSMO/Alq3/AlOx/Co spin valves (schematically illustrated in figure 1.26) have been investigated in order to detect the Hanle effect signature. The experimental details and discussion are given in chapter 5.

1.3.3 Beyond magnetoresistance

Although the main experimental efforts in the field of organic spintronics have so far been dedicated to the electrical detection of a magnetoresistance signal, other approaches have also been investigated. Two powerful techniques introduced recently in the field of organic spintronics, two-photon photoemission (2PPE) spectroscopy and muon spin-rotation technique, have succeeded in revealing the profile distribution of the spin polarization inside OSCs [45]. 2PPE spectroscopy experiments are performed with just a few OSC monolayers grown on top of an intrinsically spin-polarized ferromagnetic material [7]. Spin-polarized electrons from the metal are excited by the first energy pulse into an intermediate energy state. Some of the electrons propagate into the OSC where, with a certain probability, they can

be excited by the second photon causing the photoemission (figure 1.28a). The analysis of the average spin polarization of the photoemitted electrons allows for the definition of the exact scattered intensity along both the space and the energy profiles. The spin-polarized injection efficiency from Co into the first monolayer of the copper phthalocyanine (CuPc) was estimated to be close to 100% (that is, no losses with respect to the starting value). Noticeably, a weak decay of the polarization was registered for up to 16 monolayers (40% spin polarization remaining), although we must note that this experimental technique is less accurate for relatively thick layers.

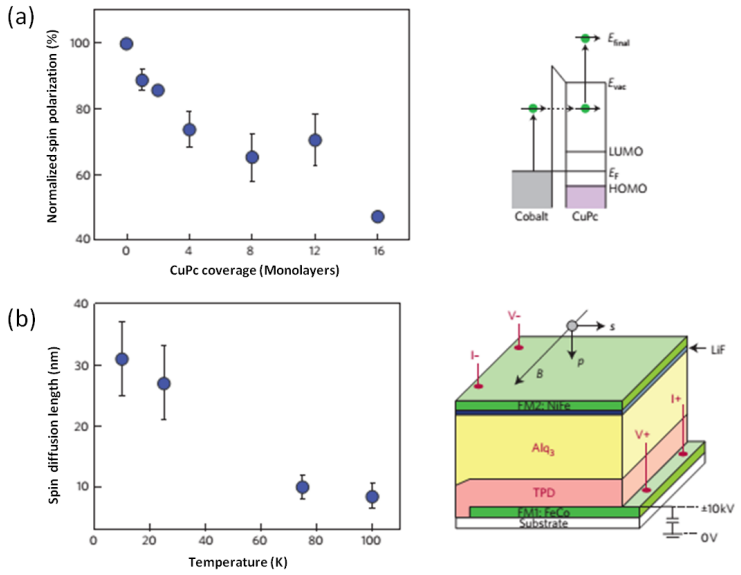

Figure 1.28: (a) On the left, normalized spin polarization as a function of CuPc thickness on a Co/CuPc junction. The values, obtained by two-photon photoemission spectroscopy [7], show a spin-injection efficiency of 85% from the Co substrate into the CuPc unoccupied molecular orbitals. On the right, schematic representation of the two photon photoemission spectroscopy technique. CuPc electrons are excited from the Co by an initial light pulse in intermediate states lying between the Fermi and the vacuum level of the hetero-junction. A second photon gives to some of those excited electrons enough energy to be photoemitted. (b) On the left, temperature dependence of the spin-diffusion length in Alq3 extracted from the muon spin-relaxation experiments reported by Drew et al. [8]. On the right, a schematic representation of the device is shown. B represents the magnetic field, p the muon momentum, s the initial muon polarization, FM1 and FM2 the ferromagnetic contacts.

In a second report, electrical injection was combined with low energy muon spin

rotation to study the spin-diffusion length (l_s) inside Alq3 in a standard vertical spin-valve device [8]. The stopping distribution of the spin-polarized muons was varied in the range 3-200 nm by controlling the implantation energy. A quantitative analysis determined the spin-diffusion length and its temperature dependence. On the one hand, the diffusion length reached a low temperature value of 35 nm: a lower value than the one estimated from electrical measurements ($>$ 100 nm), a discrepancy that could nevertheless be explained, bearing in mind the imperfect injection efficiency of the device being studied. On the other hand, the weak temperature dependence of the l_s is in good qualitative agreement with independent MR characterizations in Alq3-based devices [107].

A further alternative solution to the magnetoresistance measurements has been proposed recently by the research group of the professor Sirringhaus. They managed to pump a pure spin current into a highly-doped conductive organic material (PEDOT:PSS) [129] and into an undoped OSC (PBTTT) [130] by means of ferromagnetic spin-wave resonance (FMR) technique, and to convert this spin current into a transverse charge current through the spin-orbit-coupling-mediated inverse spin Hall effect (ISHE). The conversion of a spin current into an electric signal had been demonstrated before and used to study metallic systems [131, 132, 133, 134]. The mechanism is illustrated in figure 1.29, taken from Ref. [131]. The sample, in this case a $Ni_{81}Fe_{19}$(10nm)/Pt(7nm) bilayer film, is placed near the center of a microwave cavity at which the magnetic-field component of the microwave mode is maximized while the electric-field component is minimized. During measurement, the microwave mode with a frequency of f=9.45 GHz is exited in the cavity, and an external static magnetic field H is applied in the sample plane. When H and f fulfill the FMR condition, a pure spin current J_s with a polarization σ parallel to the external-field direction is resonantly injected into the Pt layer by spin pumping. Due to the strong SOC of the Pt, the electron trajectories are bent according to σ, producing an effective current J_c given by

$$J_c = D_{ISHE} J_s \times \sigma, \tag{1.32}$$

where D_{ISHE} is a coefficient representing the ISHE efficiency in a material. Using the lock-in technique, the FMR signal is measured as an electric-potential difference V_{ISHE} between the electrodes attached to the Pt layer. Watanabe et al. [130] inserted PBTTT spacer layers with different thicknesses d between NiFe and Pt

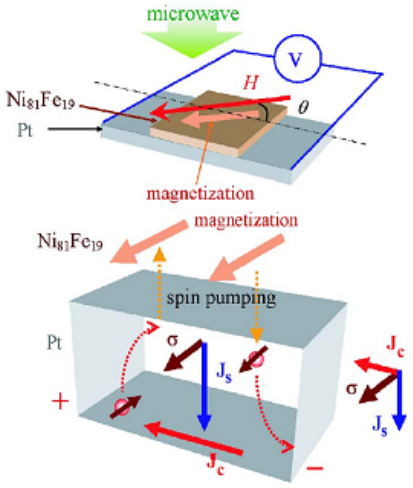

Figure 1.29: Schematic illustration of the spin pumping effect and the inverse spin-Hall effect (ISHE) in a NiFe/Pt bilayer film. J_s and J_c denote the spatial directions of a pure spin current generated by spin pumping and an electric current generated by ISHE, respectively. σ is the spin-polarization vector of the spin current J_s. The dotted arrows in the Pt layer describe electron motion bent by the spin-orbit interaction in the Pt layer, a motion responsible for ISHE [131].

(figure 1.30a). Showing that a signal V_{ISHE} can still be detected for d up to 400 nm (in the range 200 K-300 K), they demonstrated this material to have a long temperature-indipendent spin relaxation length (figure 1.30b). Recently another group [135] performed a similar experiment employing Alq3 as spacer layer, estimating a spin relaxation length $l_s \approx 50$ nm. As already pointed out by these groups, to generate the sizeable voltage signal in the Pt, the spin current transmitted through the polymer should be large, and to explain the observed values they need to assume a spin conductivity in these OSC that is several orders of magnitude higher than what is expected from the measured electrical conductivity. They justify this assumption by considering an exchange contributions to spin diffusion proposed by Yu [136]. In this theoretical paper it has been argued that, if the polaron density is large enough ($> 10^{17}$ cm^{-3} for Alq3), the exchange-induced spin motion, which is more rapid than the polaron hopping, becomes dominant. Thus the spin and charge transport in the organic material may be decoupled.

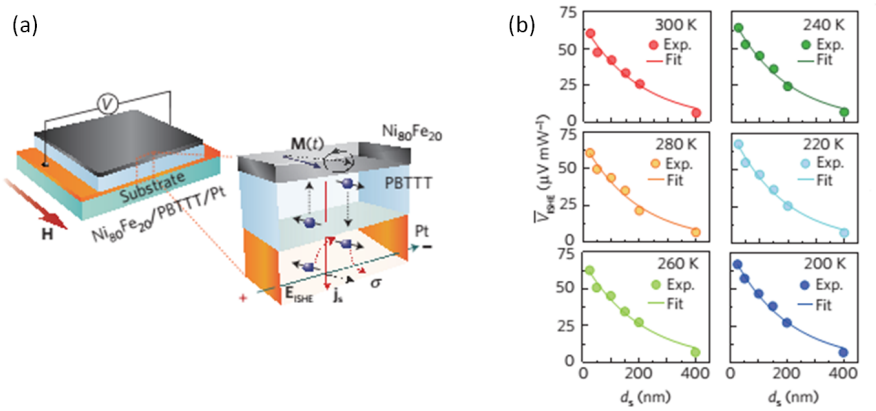

Figure 1.30: Schematic illustration of the spin pumping effect and the inverse spin-Hall effect (ISHE) in a NiFe/PBTTT/Pt trilayer device [130].

1.3.4 Spinterface

Since the publication of the pioneering works on organic spintronics [1, 2], in addition to the study of the energy-level-allignment at a metal/OSC interface (see paragraph 1.1.3), many efforts have been made in order to understand the spin-polarization properties of FM/OSC interfaces [41]. This gave rise to the so-called 'spinterface' science, term introduced by Sanvito [137].

Suzuki et al. [138] measured the spin polarization of metal (Mn, Fe, Cu, and Mg) and metal-free phthalocyanines on Fe(100) by means of Spin-Polarized Metastable Deexcitation Spectroscopy (SPMDS). They found that the spin polarization of both metal and metal-free phthalocyanines is antiparallel to the Fe substrate.

X-Ray Magnetic Circular Dichroism (XMCD) is considered an ideal method to probe the magnetization of different materials at an interface because of the unique element-resolved function. Scheybal et al. [139] reported the first XMCD study of OSC/ferromagnetic metal interfaces, demonstrating the existence of an exchange coupling between a large organic adsorbate manganese MnTPPCl and a ferromagnetic cobalt substrate. Their work was followed by many others [140, 141]. Zhan et al. [46] showed direct evidence for the spin polarization of organic molecular π-orbitals by N K-edge XMCD measurement of Alq3 sub-monolayers on Fe surfaces (figure 1.31a). Another powerful technique employed to investigate the spin-polarization properties of FM/OSC interfaces is the Spin-Polarized UPS

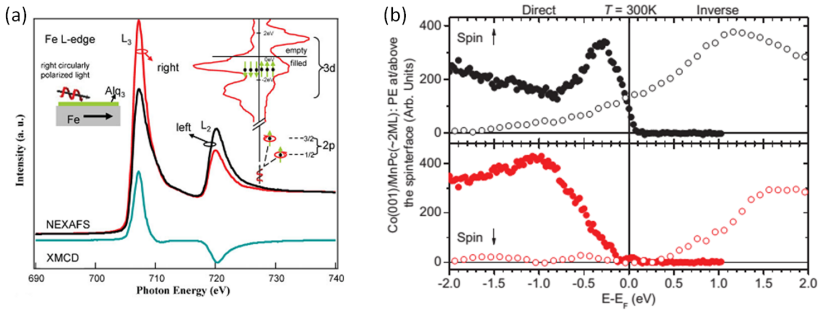

Figure 1.31: Examples of XMCD (a) and PE (b) spectra taken on hybridized FM/OSC interfaces. Fe L-edge X-ray absorption spectra for right circularly polarized X-rays with right (red) and left (black) magnetization and XMCD (cyan) of the substrate (300 K, 500 Gauss). The inset on the right shows a diagram to illustrate the Fe L-edge XMCD effect. Reproduced from Ref. [46]. (b) Spin-resolved difference spectra of direct (closed symbols; hν=520 eV) and inverse (open symbols) photoemission (PE) spectroscopy at room temperature of Co/MnPc (2.6(2.0) ML for direct(inverse) PE) revealing a P $\approx$ 180% at E_F. Reproduced from Ref. [142].

(SP-UPS). Using 2PPE spectroscopy, Cinchetti et al. [7] demonstrated an efficient spin injection from the Co substrate into the CuPc unoccupied molecular orbitals. Since then several other interfaces have been investigated, in particular Steil et al. [143], from the same group, studied Alq3 on Co (figure 1.31b). A recent work by Djeghloul et al. [142] showed highly efficient MnPc/Co and H_2Pc/Co spinterfaces by SP direct and inverse PE spectroscopy (figure 1.31b). In particular they measured a magnetic moment on the molecule's nitrogen π orbitals, confirming the ab-initio calculations.

However, as already argued by Barraud et al. [144] and Sanvito [137], the results obtained by means of the above introduced experimental techniques are averaged on a relatively large area (at least on the micrometric scale), while different portions of the device may contribute in drastically different ways to the magnetoresistance of the device. The properties of the device can, in fact, be dominated by narrow 'hotspots' where the density of the spin-polarized current is high, surrounded by large areas that transmit little current at all. Thus it is necessary to perform local measurements to obtain reliable information about the poorly understood phenomena occurring at the interface. Barraud et al. [144] indented an Alq3 layer with an atomic force microscope (AFM) cobalt tip, obtaining nanometric LSMO/Alq3/Co junctions. This allowed them to perform local I-V and R-H

measurements, obtaining positive magnetoresistance traces up to 300 % at low temperature (figure 1.32), a record percentage for organic SVs. In the same paper they

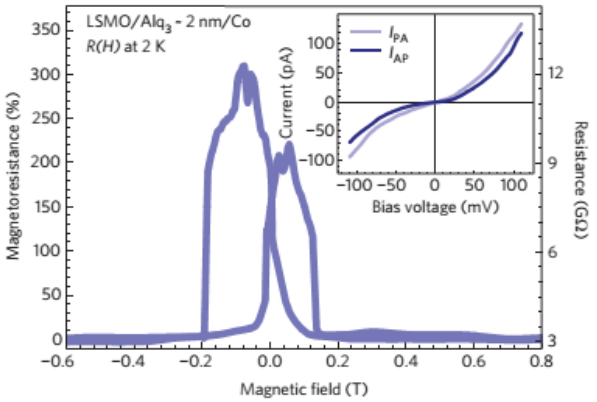

Figure 1.32: Magnetoresistance curve of a nanometric LSMO/Alq3/Co junctions obtained at 2 K and 5 mV. In the inset are shown the I-V curves recorded at 2 K in the parallel ($_{PA}$) and antiparallel (I_{AP}) magnetic configurations. Reproduced from Ref. [144].

also introduced a phenomenological model in order to explain the apparent discrepancies on the observed magnetoresistance signs in LSMO/Alq3/Co spin valves reported in the literature [2, 107, 145]. The basic idea is that a spin-dependent broadening Γ of the molecule states at the metal/organic interface occurs, modifying the spin-polarization at the Fermi level. This could lead to an increase of the effective spin polarization of the electrodes or even change their sign, so that a new effective spin-dependent interface including the first molecular layer has to be defined (figure 1.33). The model was then used by Sanvito [137], who introduced the term spinterface. The inversion of the spin polarization at the organic site due to the hybridization of the out-of-plane p_z orbitals with the d states of the metal was demonstrated experimentally by Atodiresei et al. [146] by means of spin-polarized scanning tunneling microscopy (SP-STM), as shown in figure 1.34. However such investigations on the LSMO/organic interface have not been carried out, yet.

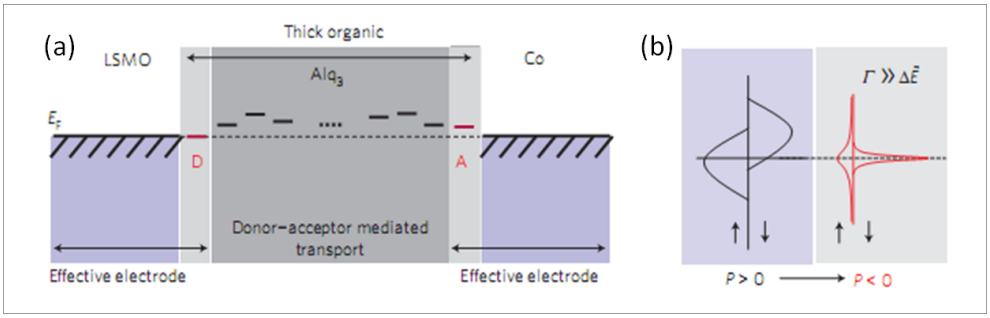

Figure 1.33: (a) Schematic drawing of the model of donor-acceptor-mediated transport. The donor (D) and acceptor (A) states coupled to the left and right leads are shown in red. Bulk Alq3 transmission between the donor and acceptor is summarized by series of molecular states in black. (b) Illustration of the spin-dependent interfacial molecular hybridization (SHIPS) obtained for strong coupling to a ferromagnetic electrode in the limit of $|\Gamma| \gg |\Delta\tilde{E}|$ with $|\tilde{E}| \sim 0$, where $\tilde{E}$ is the energy difference with respect to the Fermi level. A simple one-band DOS is considered for simplification. The level undergoes a spin-dependent broadening while being brought to resonance. Accordingly, its spin polarization at the Fermi level (dashed line) is reversed compared with the ferromagnetic electrode one [144].

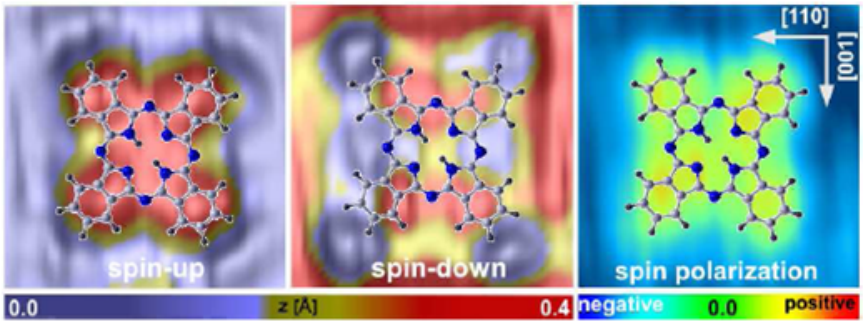

Figure 1.34: Experimental (22Å×22 Å) SP-STM images for H_2Pc adsorbed on 2 ML Fe/W(110) at V=+0.05 for both spin channels and spin polarization. H_2Pc molecules show a high locally varying spin-polarization ranging from attenuation to inversion with respect to the ferromagnetic Fe film [146].

Chapter 2

Memristors and memristive spin valves

2.1 Memristors

A memristor (short for memory-resistor) is a fourth fundamental circuit element, in addition to the already known resistor, capacitor and inductor. Its existence was theorized in 1971 by the engineer Leon Chua from symmetry arguments [3]. Chua argued that there exist four fundamental variables in a circuit: the electric current i, the voltage V, the charge q flowing in the circuit, and the magnetic flux ϕ. Since charge and current are governed by

$$i = dq/dt \tag{2.1}$$

and voltage and magnetic flux are governed by Faraday's law

$$V = d\phi/dt \tag{2.2}$$

it means there are four possible circuit elements that can connect the variables: the resistor ($R = dV/di$), the capacitor ($C = dq/dV$), the inductor ($L = d\phi/di$) and the fourth, never seen before, memristor ($M = d\phi/dq$). The relationship between circuit elements and variables is outlined in figure 2.1. From the memristor equation and using Faraday's law and the conservation of charge, we obtain

$$V = Mi. \tag{2.3}$$

If M is a constant then we have obtained nothing more than a normal resistor, but if M depends on q itself we obtain the general and more interesting formula

$$V = M(q)i. \tag{2.4}$$

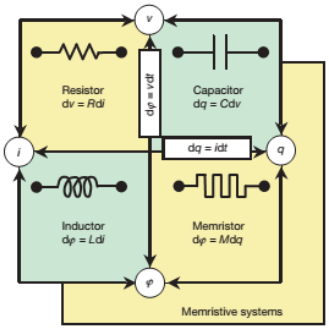

Figure 2.1: The four fundamental two-terminal circuit elements: resistor, capacitor, inductor and memristor [4].

The i-V characteristic of such a nonlinear relation between q and ϕ for a sinusoidal input is generally a frequency-dependent Lissajous figure, and no combination of nonlinear resistive, capacitive and inductive components can duplicate the circuit properties of a nonlinear memristor (although including active circuit elements such as amplifiers can do so) [3]. Because most valuable circuit functions are attributable to nonlinear device characteristics, memristors compatible with integrated circuits could provide new circuit functions such as electronic resistance switching at extremely high two-terminal device densities. The most basic mathematical definition of a current-controlled memristor for circuit analysis is the differential form

$$V = R(w)i \tag{2.5}$$

$$\frac{dw}{dt} = i \tag{2.6}$$

where w is the state variable of the device and R is a generalized resistance that depends upon the internal state of the device. In this case the state variable is just the charge, but no physical model was able to give this simple equation. In 1976 Chua and Kang generalized the concept of memristor to a much broader class of nonlinear dynamical systems they called memristive systems [147], described by the equations

$$V = R(w, i)i \tag{2.7}$$

$$\frac{dw}{dt} = f(w, i). \tag{2.8}$$

R and f can be functions of time but this analysis is restricted to the case of time independent devices. It is clear from these equation that we are essentially talking about devices that feature resistive switching. Even though non-volatile resistance switching effects were already known in the 60s [148, 149] a complete realization of a memristor device, had to wait until the recently published pioneering paper by Strukov et al. [4]. They also proposed a phenomenological model of a device that act as a memristor described by equation 2.4, based on the assumption that the observed hysteresis in the i-V characteristics requires some sort of atomic rearrangement that modulates the electronic current. On the basis of this proposition, they consider a thin semiconductor film of thickness D sandwiched between two metal contacts, as shown in figure 2.2. The total resistance of the device is de-

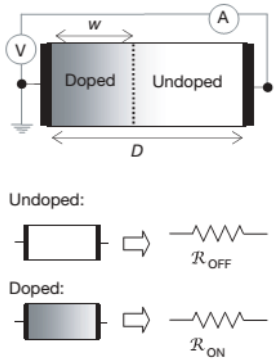

Figure 2.2: Schematic representation of a memristive device. D is the total thickness of the spacer layer, w is the thickness of the doped region [4].

termined by two variable resistors connected in series, representing respectively a region of thickness w with a high concentration of dopants ($R_{ON}w/D$) and the rest with a low density of dopants ($R_{OFF}(1 - w/D)$). The application of an external bias $V(t)$ across the device will move the boundary between the two regions by causing the charged dopants to drift. For the simplest case of ohmic electronic conduction and linear ionic drift in a uniform field with average ion mobility μ_V, the device can be described with the linear-drift model

$$V(t) = \left[R_{ON}\left(\frac{w}{D}\right) + R_{OFF}\left(1 - \frac{w}{D}\right)\right] i(t) \tag{2.9}$$

$$\frac{dw}{dt} = \mu_V \frac{R_{ON}}{D} i(t). \tag{2.10}$$

Inserting the integral of 2.10

$$w = \mu_V \frac{R_{ON}}{D} q(t) \tag{2.11}$$

in 2.9 and considering $R_{OFF} \gg R_{ON}$, the charge-dependent memristance of the system is obtained:

$$M(q) = R_{OFF} \left(1 - \frac{\mu_V R_{ON}}{D^2} q(t)\right). \tag{2.12}$$

It should be observed that, because of the factor $1/D^2$, for any materials this term will be 10^6 times larger in absolute value at the nanometer scale than it is at the micrometer scale. It is also interesting to note that in no part of this treatment was any magnetic field involved, even though the concept of the memristor itself revolves around the magnetic flux. The state variable described in equation 2.11 is proportional to the charge q that passes through the device until the boundary condition

$$0 \leq w \leq D \tag{2.13}$$

is fulfilled.

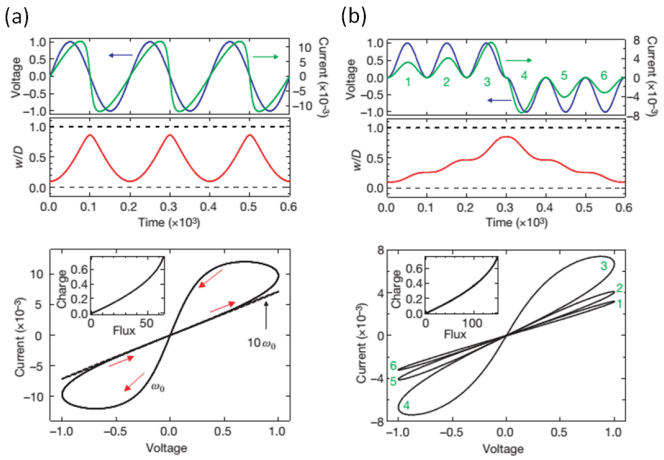

Figure 2.3: Simulations of a memristive device. In the top panels the applied voltage (blue), the resulting current and w/D(red) are plotted as a function of time. In (a) a sinusoidal bias voltage $V = V_o sin(\omega_o t)$ is applied, with $\omega_o = 2\pi D^2/\mu_V V_0$ and $R_{OFF}/R_{ON} = 160$. In (b) the applied voltage is $V = \pm V_o sin^2(\omega_o t)$ with $R_{OFF}/R_{ON} = 380$. The bottom panels show the i-V characteristics given respectively by the two bias voltages described above [4].

As long as the system remains in this regime, any symmetrical alternating-current

voltage bias results in double-loop i-V hysteresis that collapses to a straight line for high frequencies (figure 2.3a). Multiple continuous states will also be obtained if there is any sort of asymmetry in the applied bias (figure 2.3b). In any case the hysteresis loops are pinched at V=0, a fundamental condition to define a memristive system. Several boundary conditions can be imposed for the hard-switching case, that is when the value of w reaches either of the boundaries (large voltage excursions or long times under bias). If w remains constant until the voltage reverses polarity, the device satisfies the normal equations for a current-controlled memristive system 2.7 and 2.8.

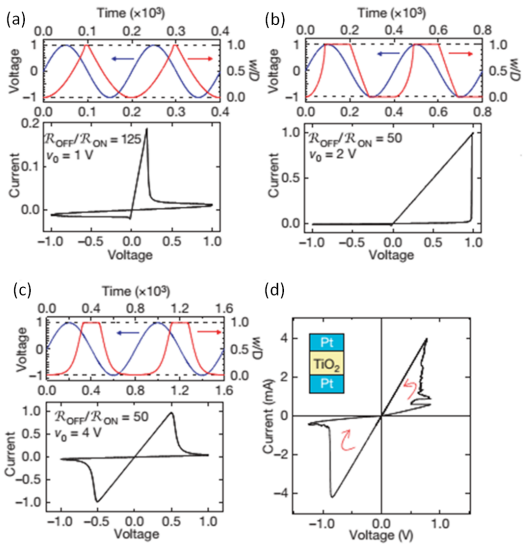

Figure 2.4: (a),(b) Simulated i-V characteristics in the linear ion drift approximation. (c)Simulated i-V characteristic for nonlinear ion drift. (d) Experimental i-V characteristic taken on a nanoscale $Pt/TiO_2/Pt$ junction [4].

In figure 2.4a,b two i-V curves are simulated for such a memristive device. In figure 2.4a the upper boundary is reached while the derivative of the voltage is negative, producing an apparent or "dynamical" negative differential resistance (NDR). It is simply a result of the charge-dependent change in the device resistance, and it is sensitive to time and device history, contrary to the "static" negative differential resistance. This can be observed by the strong dependence on the frequency of a sinusoidal driving voltage. For example when the boundary is reached much faster by doubling the magnitude of the applied voltage (figure 2.4b) the switching event

is a monotonic function of current. Despite the hard-switching case seems to be defined by a clear threshold voltage, the effect is actually dynamical. This means that any positive voltage V applied to the device in the OFF state will eventually switch it to the ON state after a time $\sim D^2 R_{OFF}/(2\mu_V V + R_{ON})$. It should be noted that the device will remain in the on state as long as a positive voltage is applied, but even a small negative bias will switch it back to the off state. In nanoscale devices, small voltages can yield enormous electric fields, which in turn can produce significant nonlinearities in ionic transport. This nonlinear drift condition when w is close to 0 or D can be expressed by multiplying the right side of equation 2.10 by a window function $w(D-w)/D^2$. In this case the switching is essentially binary because the ON and OFF states can be held much longer if the voltage does not exceed a specific threshold. Nonlinearity can also be expected in the electronic transport, which can be due to, for example, tunneling at the interfaces or high-field electron hopping. Figure 2.4c shows a simulated i-V characteristic for this condition, closely resembling the experimental i-V characteristic measured on a nanoscale $Pt/TiO_2/Pt$ junction (figure 2.4d).

2.2 Memristive spin valves

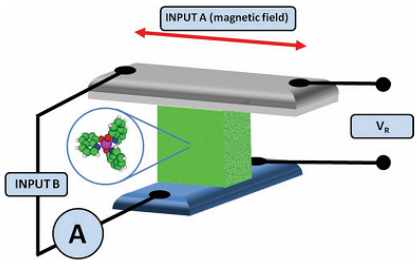

Figure 2.5: Schematic representation of the multifunctional device investigated by Prezioso et al. [6]. From the top: Co ferromagnetic electrode, followed by a thin AlOx tunnel barrier, a layer of the organic semiconductor Alq3 and finally the bottom $La_{0.7}Sr_{0.3}MnO_3$ ferromagnetic electrode. The device was measured in four contact mode by applying a bias voltage at INPUT B, reading the current generated with an ammeter A and measuring the effective voltage V_R produced at the sense contacts. The resistance is defined as $R = V_R/A$. The magnetoresistance is measured by applying a magnetic field parallel to the Co electrode.

Resistive switching have been reported also in organic LSMO/Alq3/AlOx/Co

spin valve devices [150, 5]. Furthermore in these works an interesting interplay between magnetic and resistive switching effects was shown to occur, allowing to control the spin-valve magnetoresistance (SVMR) by setting the device in different resistive states (figure 2.6).

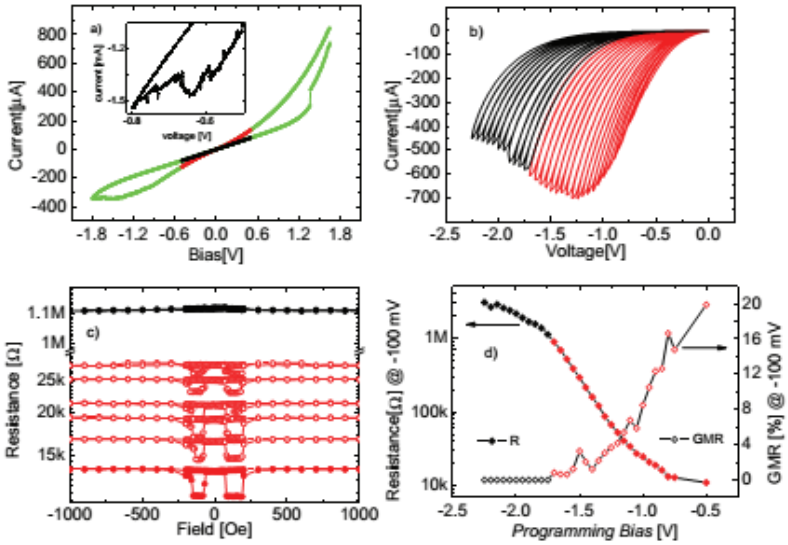

Figure 2.6: The measurements shown here were taken using a sample with a 200 nm thick Alq3 layer at 100 K. a) Typical memristor pinched I-V curve. Inset: high resolution I-V curve of the a NDR region. b) Sequence of I-V curves reaching increasingly higher (50 mV step) negative biases (programming bias). The red curves correspond to programming biases that leave the device with a GMR signal. The black curves reach programming biases high enough to destroy the GMR signal. c) GMR curves taken at -100 mV in the lowest memristance state (red points), intermediate state (red circles) and highest memristance state (black points). d) The resistance state at -100 mV, full diamonds, and the GMR magnitude, empty diamonds, are shown as a function of the applied programming bias (with the I-V curves from panel (b). The red and black colors correspond to the presence or otherwise of the GMR as in the other panels [6].

A step forward was the implementation of an IMP logic gate [6] based on a single multi-functional device. As shown in figure 2.5 the two inputs of the logic gate are the magnetic field (A) and the applied bias voltage (B). Boolean values are attributed to this inputs and to the output current as explained in figure 2.7. Electric switching for up to 10^4 cycles were detected showing a good stability, while the GMR effect disappears after a few tens of cycles.

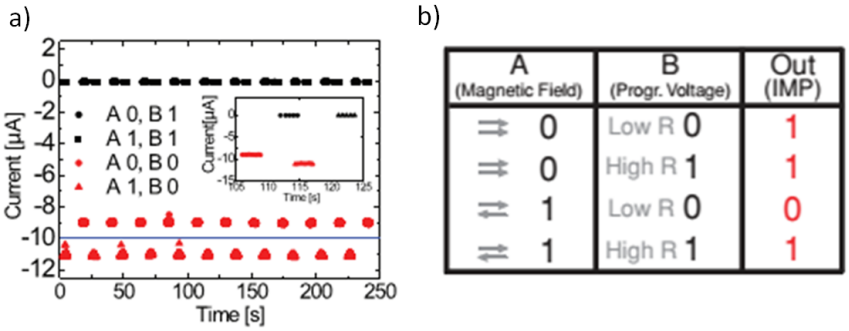

Figure 2.7: a) Inputs and detected output of MEM used as a logic IMP gate. Input A is represented by the magnetic field: the zero-value bit (0) corresponds to the parallel orientation of the electrode magnetization (in this case 3 kOe), while the value 1 is assigned to the antiparallel configuration. Input B corresponds to programming-bias pulses needed to set the device in the low-resistance state (value 0) or the high-resistance state (value 1). After the application of the input signals, the device is read at -100 mV and the measured current that represents the logic-gate output is reported in graph a). These are experimentally collected data, taken after the application of the proper input signals. By setting a threshold in the output current (the blue line in the graph), it is possible to assign 0 for currents more negative than the threshold and 1 for lower currents. A single cycle, represented by the four combinations of inputs, is shown in the Inset. The universal IMP logic-gate truth table (panel b) is reproduced by using only one single device.

Chapter 3

Experimental setup and device fabrication

In this thesis I studied LSMO/Alq3/AlOx/Co vertical spin valves. In this chapter I will describe the fabrication process and the equipment and techniques used to characterize the devices.

3.1 Electrical characterization

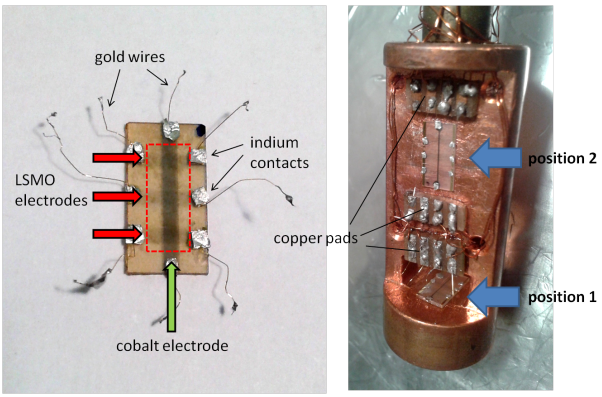

Figure 3.1: (a) Top view of a substrate with three devices, whose active region corresponds to the cross section between LSMO and cobalt electrodes. Organic layer is deposited inside the region indicated by the red dashed line. (b) Samples located on the cryostat sample holder. The copper pads connect the devices to the external plug. Position 1 and position 2 allow to rotate the sample respectively in plane and out of plane.

Figure 3.1a shows three spin-valve devices on a STO substrate. LSMO and cobalt electrodes are connected to gold wires with a diameter of 50 μm by means of indium. The samples are located on the cryostat sample holder and the wires are soldered to the copper pads (figure 3.1b), which connect the DUT (device under test) to the external plug. Electrical characterizations have been carried out by using a Keithley 236 Source Measure Unit (SMU). Figure 3.2 shows the SMU electrical scheme in the Source V-Measure I configuration, both for remote sense (4-points) and local sense (2-points) mode. An ammeter is connected between

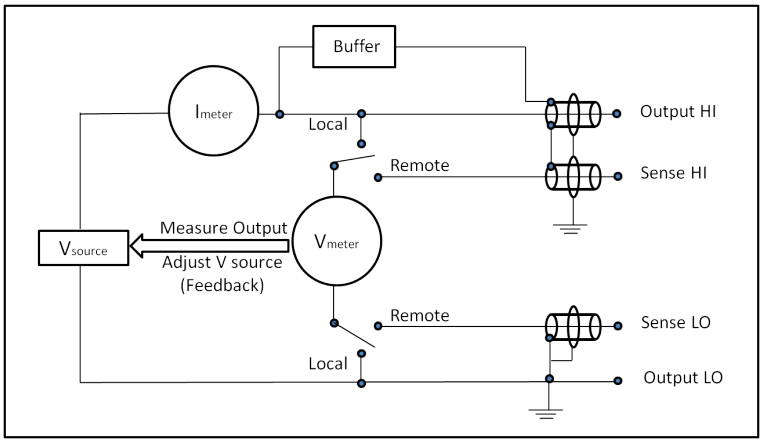

Figure 3.2: Electrical scheme of Keithley 236 SMU in the SourceV-MeasureI configuration. The instrument has an integrated feedback system: the measured voltage V_{meter} is compared with the programmed voltage level and, if they are not the same, V_{source} is adjusted accordingly. In local sense mode, V_{meter} measures the voltage at the output, while in the remote sense mode it measures the effective voltage across the DUT.

the voltage source (V_{source}) and Output HI. Sense circuitry is used to constantly monitor the output voltage and make adjustments to V_{source} as needed. V_{meter} measures the voltage at the output (local sense) or at the DUT (remote sense) and compares it to the programmed voltage level. If the sensed level and the programmed value are not the same, V_{source} is adjusted accordingly ensuring that the programmed voltage appears at the DUT. Triaxial cables (triax) are used to accurately measure low currents. Guard is kept at the same potential as the Output HI by the buffer circuit to eliminate the effects of the leakage current (and capacitance) that exists between the Output HI and the Output LOw. A keithley 708A switching system has been used to automatically redirect the signals from

the SMU to the desired electrodes as schematically represented in figure 3.3a. The

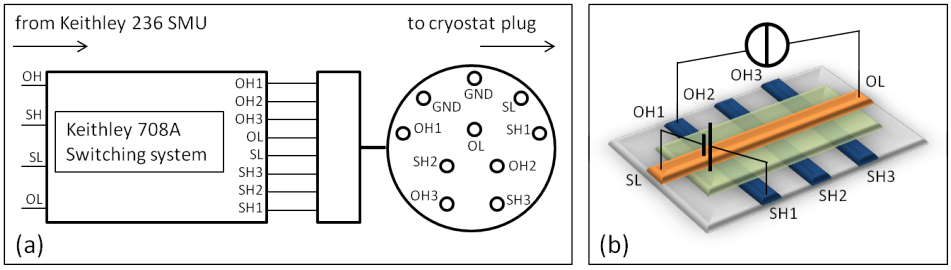

Figure 3.3: (a) Schematic representation of the circuitry connecting the SMU to the cryostat plug. The source signals (OH, OL) and the sense signals (SH, SL) from the SMU are sent to a Keithley 708A switching system which redirects them to the desired outputs (OH1, OH2, OH3, OL, SL, SH1, SH2, SH3). The core pins of the triax from the switching system are collected into the cryostat plug. (b) Device contacts corresponding to the pins of the cryostat plug. As an example device 1 in remote sense configuration is illustrated.

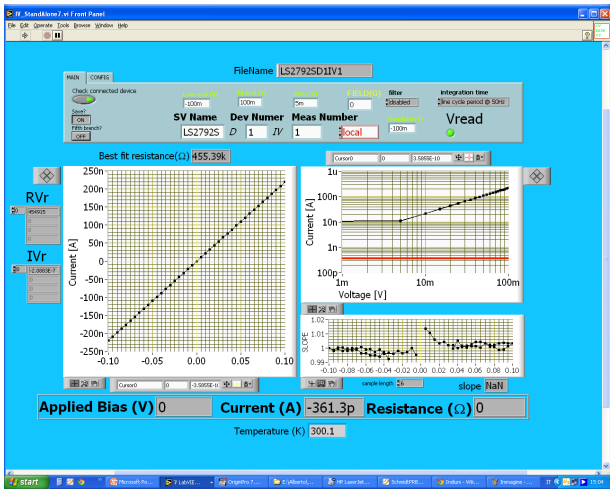

Figure 3.4: User interface of the LabView VI used to acquire I-V characteristics.

SMU and the switching system are connected in series to a PC through a GPIB to USB converter and I-V characteristics are acquired by means of a software developed in LabView programming environment (figure 3.4).

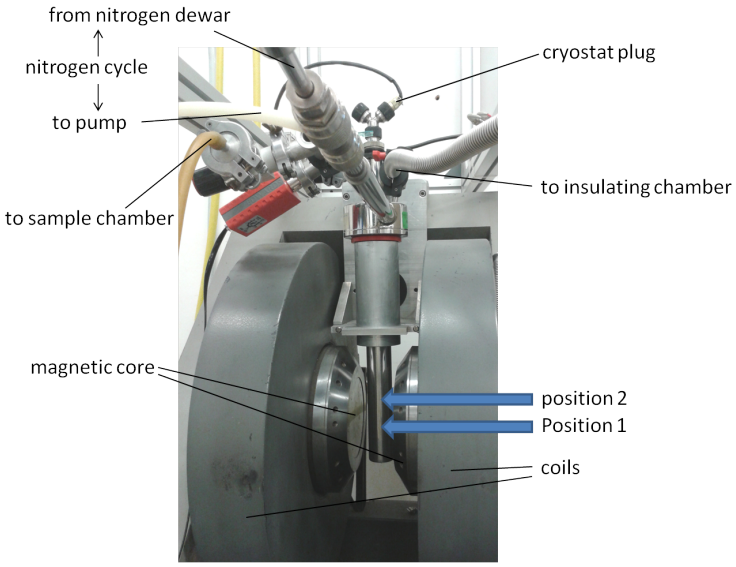

Figure 3.5: Experimental setup for magnetoresistive characterizations. The blue arrows indicate the position of the samples between the magnetic poles. The cryogenic system and the electromagnet are described in the text.

3.2 Magnetoresistive characterization

The sample holder is introduced into the inner chamber of a gas-exchange cryostat from Oxford Instruments, filled with nitrogen gas up to the pressure of 10^2 mbar. The outer chamber is kept at 10^{-5} mbar, in order to thermally insulate the system. The intermediate chamber is part of the nitrogen circuit: liquid nitrogen is pumped into the chamber from the dewar and the exhausted gas is pumped out, as described in figure 3.5. The samples can be cooled down to 77 K and heated up to 400 K at the desired rate (K/min) by means an Oxford ITC 503S temperature controller. The coils of the EPR electromagnet are connected to an Elind KL power supply through an high power switcher which allows to change the current direction. The right current-to-field conversion factor was obtained by calibrating the magnet with a gaussmeter. The high field homogeneity over a large volume guarantees that the same magnetic field is applied both to position 1 and to position 2 (figure 3.5). R-H characteristics have been taken by applying a fixed bias potential to the DUT and acquiring its resistance values as a function of magnetic field, typically ranging from -3 kOe to 3kOe (figure 3.6). MR as a function

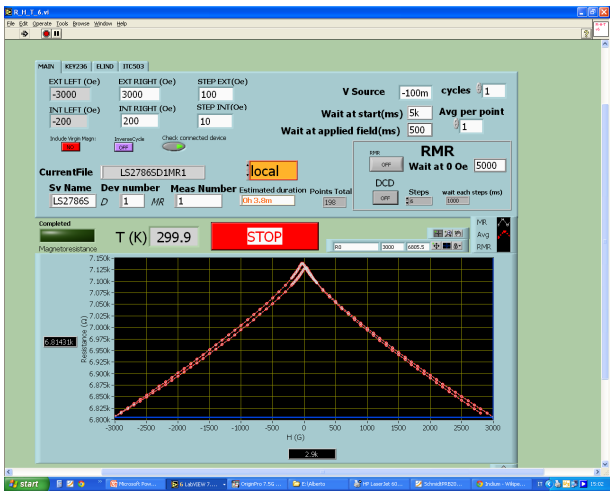

Figure 3.6: User interface of the LabVIEW VI used to acquire R-H characteristics.

of temperature are also measured: the sample is kept at a fixed bias potential and the difference between the resistance at zero and at applied field is taken, while the temperature is increased (decreased) at a controlled rate. Moreover, as mentioned before, the sample holder allows to rotate the sample in plane and out of plane (figure 3.7) making possible to study the MR as a function of angle.

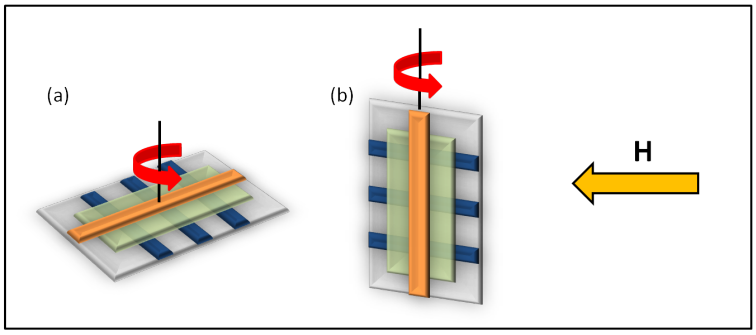

Figure 3.7: (a) Sample in position 1 can be rotated in plane. (b) Sample in position 2 can be rotated with a field component out of plane.

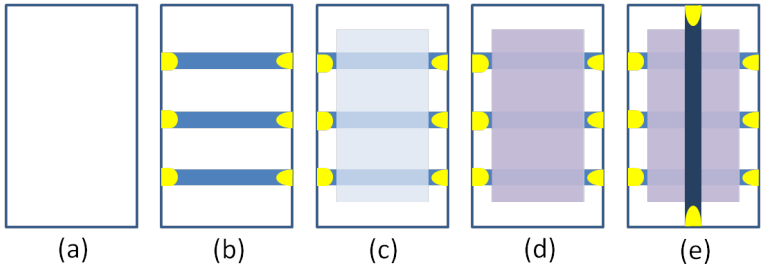

Figure 3.8: Fabrication steps for a spin-valve device. (a) STO substrate. (b) LSMO bottom electrodes with gold contacts on top. (c) Alq3 spacer layer (10 nm $<$ d $<$ 300 nm). (d) AlOx tunnel barrier (d $\approx$ 2 nm). (e) Co top electrode with gold contacts.

3.3 Device fabrication

The spin-valve devices are fabricated by shadow masking following the steps illustrated in figure 3.8. As a substrate a 10x5 mm^2 STO(100) single crystal from CRYSTAL GmbH is used. The crystal is cleaned by sonication in isopropanol.

LSMO bottom electrode

After this cleaning process the sample is located on the sample holder of a Channel Spark Ablation (CSA) system (figure 3.9). A stoichiometric $La_{0.7}Sr_{0.3}MnO_3$ target from Pi-KEM ltd is ablated by means of a pulsed electron beam and three 1x5 mm^2 LSMO stripes are then deposited on the substrate, previously covered with a shadow mask and heated up to 800 °C. In order to extract electrons for the beam an oxygen plasma is triggered as shown in figure 3.9. A negative high voltage (5-30 kV) power supply is directly connected to a hollow cathode (a) and a capacitor (b). The latter is grounded through an air gap (c) having a floating electrode wich is decoupled from the capacitor by charging resistor (d). Between the charging resistor and the floating electrode of the air gap a triggering anode plate (e) is located and inserted in the bulb (f). At a sufficient high voltage a spark brakes down the air gap (c), a rapid variation of the electric field between the hollow cathode and the anode plate ionizes the gas molecules in the bulb triggering plasma in the cathode cavity (a), where the amplification of the discharge happens. Because of the high resistance of the charging resistor, the capacitor discharge happens through the low impedance electron beam in the Pyrex channel(h).

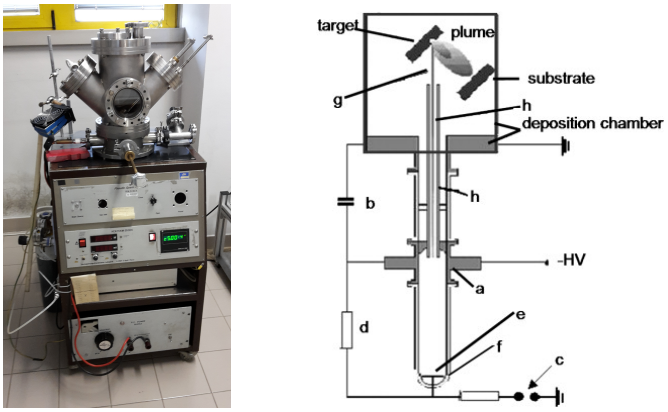

Figure 3.9: Scheme of the Channel Spark Ablation system. The generator consists of a transient hollow cathode (a) connected to a dielectric acceleration tube and the trigger. The dielectric tube is connected through a narrow exit to the transient hollow cathode and picks up the electron flow for the final acceleration which forms the electron beam. The inner wall of the deposition chamber is the actual anode. The trigger circuit consists of the air gap with a floating electrode (c), the charging resistor (d), bottom anode(e) [151].

The electron beam current would be continuous if the power supply could provide a sufficient current, but since its limited in current, the electron beam cannot be sustained and the discharge extinguishes up to the new spark in the air gap. As a consequence the beam assumes a pulsed character. The current supplied to charge the capacitors defines the charging time and, hence, the operating frequency. The high voltage and the capacitance determine the accumulated charge and the total energy. The energy distribution of the electrons in the beam and the length of the pulse is determined by the accelerating voltage and gas pressure [151]. After the deposition of bottom electrodes, the sample is exposed to air and introduced in a load lock chamber at a base pressure of 10^{-6} mbar, where gold contacts are evaporated on LSMO stripes as illustrated in figure 3.8b.

Alq3 spacer layer and AlOx tunnel barrier

The sample is then transferred into the main chamber and annealed at 250 °C for 30 min in order to restore the LSMO surface. Once the sample is cooled down to room temperature, the organic layer deposition can start. A Knudsen cell OME 40-2-25-S from MBE (figure 3.10)a is used to evaporate 99.995% pure Alq3 from Sigma Aldrich. The crucible is heated up to the temperature of 275 °C at a base

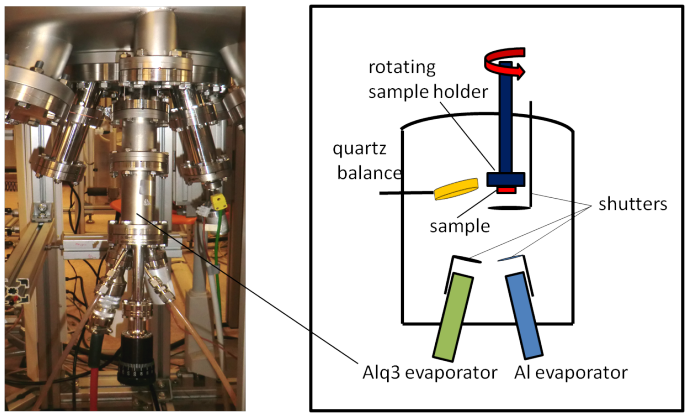

Figure 3.10: (a) Bottom part of the organic-deposition chamber. Both the Alq3 Knudsen cell and the aluminum evaporation cell can be observed. (b) Schematic representation of the chamber.

pressure of 10^{-8} mbar and the first shutter in front of the crucible is opened. An Inficon quartz crystal balance adjacent to the substrate is monitored by a Sycon Thickness Monitor STM-100. When a constant rate of 0.12 Å/s is reached a second shutter in front of the sample is opened. During the deposition process the substrate is rotated (0.14 rpm) in order to obtain a homogeneous film. When the desired thickness is obtained, both shutter are closed.
The AlOx tunnel barrier is prepared in a two step process. First the aluminum crucible is heated up to about 700 °C and a 2 nm thick aluminum layer is evaporated on top of the Alq3 layer at a rate of 0.15 Å/s, following the procedure described above. Then the sample is moved again in the load lock chamber, where the aluminum is exposed to a controlled oxygen pressure of 100 mbar for 15 min.

Cobalt top electrode

The sample is transferred in the metal-deposition chamber at a base pressure of 10^{-8} mbar. A mini e-flux e-beam evaporator from tectra GmbH is used to evaporate the cobalt top electrode. A coiled tungsten filament (ground potential) is placed in close vicinity of a cobalt rod with a diameter of 2 mm (kept at the positive potential of 2 kV). The thermionically emitted electrons are accelerated towards the rod producing a current of 8-10 mA with extremely high heating-power densities. High-purity cobalt (99.99+ %) is then evaporated on the sample as top electrode in the cross-bar geometry described in figure 3.8e. The same procedure

described for the organic layer deposition is followed. In this case a Sycon Thickness Monitor STM-1 is used to control the deposition rate (0.4 - 0.5 Å/s). Finally the sample is moved again in the load lock chamber, where gold contacts are deposited on cobalt.

Chapter 4

LSMO/Alq3/AlOx/Co spin-valves: two charge transport regimes

In the last years magnetoresistance (MR) effects have been observed in vertical spin-valve structures with tris-(8-hydroxynoquinoline) aluminum (Alq3) spacer layer thicker than 100 nm [2, 45]. However it is still debated if the observed spin-valve signals should be attributed to spin injection and transport in the organic layer [2, 108] or to tunneling through locally thin Alq3 regions [106, 109]. One of the main obstacles preventing a full understanding of the involved physical mechanisms is the low reproducibility of the published results. The reported device resistances span over several orders of magnitude, and an accurate comparative assessment is often prevented by the lack of information on important device parameters such as I-V curves, temperature dependence of the resistance, mobility, injection barriers and operating voltages, among others [45]. Several groups also pointed out that the obtained results can not be easily interpreted due to the inhomogeneity of the organic layer [106] and a poorly defined top metal/Alq3 interface: the evaporation of the top electrode can cause pinholes and metal inclusions in the organic layer over a distance of 100 nm [2]. All these considerations indicate that the organic spintronics community should make an effort to elaborate common metrology rules to allow direct comparisons between different experiments, and improve the reproducibility of the device characteristics.

Our group adopted a fabrication procedure which allowed us to obtain devices, typically with 200 nm Alq3 layer, showing a MR up to 22% at 100 K [5, 6]. However it did not guarantee a good control on the absolute value of the resistances. With

the aim to have a better reproducibility of our device parameters, we improved the surface roughness of the electrodes [151] and the homogeneity of the organic spacer layer. We studied several procedures for the organic layer growth, varying the deposition rate, the distance between the evaporator and the substrate, and introducing the substrate rotation during the deposition of the organic film. A smoother morphology of the the organic layer surface was obtained, as demonstrated by atomic force microscopy (AFM) analysis (figure 4.1), and well-defined interfaces between the organic barrier and the electrodes are generally observed in tranmission electron microscopy (TEM) images (figure 4.2). We also achieved

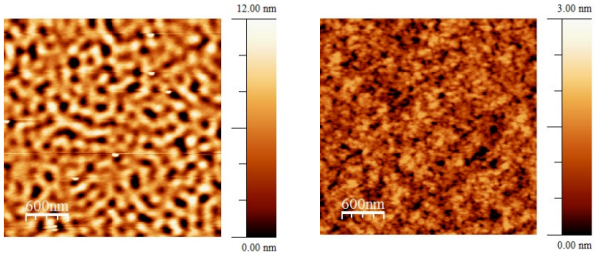

Figure 4.1: Comparison between AFM images performed on 200 nm of Alq3 deposited on a 15 nm thick LSMO film, respectively with a deposition rate of 0.08 Å/s and 0.12 Å/s. The surface roughness has been sensibly reduced.

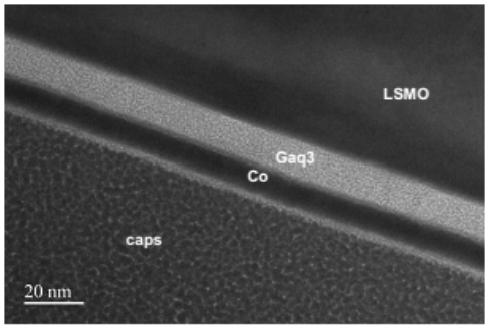

Figure 4.2: TEM image taken on device with a 15 nm thick Alq3 spacer layer showing sharp interfaces between the organic barrier and the electrodes. The image has been taken by K. O'Shea at the University of Glasgow.

a larger reproducibility of current-voltage (I-V) and resistance-applied magnetic field (R-H) characteristics. These improvements allowed us to carry out a careful

study on the thickness and temperature dependence of charge transport and magnetoresistive properties of Alq3-based spin valves. As will be shown below, two clearly distinguishable charge transport regimes have been individuated.

4.1 Charge transport as a function of thickness

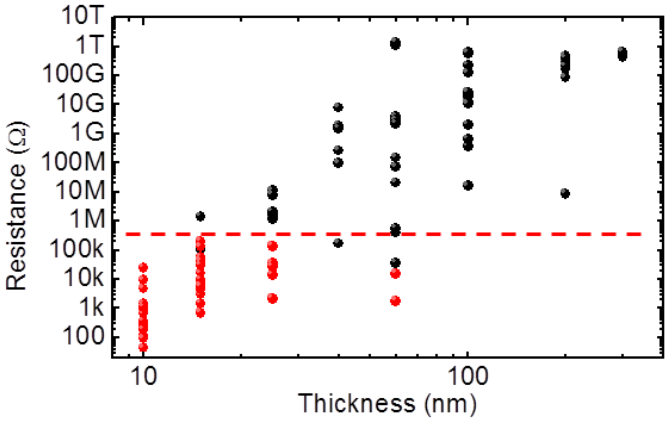

Figure 4.3: Resistances of the devices as a function of the organic layer thickness. Devices showing a spin valve signal (red circles) have been observed only below the resistance threshold indicated by the red dashed line. For low-resistance devices, the resistance values are measured at -0.1 V. High-resistance devices generally possess a bias offset and the resistance values reported are obtained by a linear fit of the I-V characteristics in the low bias region.

We studied LSMO/Alq3/AlOx/Co spin-valve devices with the organic spacer layer ranging from 10 nm to 300 nm and an active region of 1×1 mm^2. Figure 4.3 shows their resistances as a function of the Alq3 layer thickness. Despite the large dispersion of the absolute resistance values, two conduction regimes are clearly distinguishable by looking at the I-V characteristics (figure 4.4) and magnetoresistive effects. Generally speaking, thin devices (d$\leqslant$25nm) show resistances well below 1 MΩ even at low bias voltages, near-parabolic differential conductance (G - V, where G = dI/dV) traces, and a negative spin valve signal in the range from -0.5 V to 0.5 V (magnetoresistive devices are indicated by red circles in figure 4.3). On the other hand, the I-V characteristics of thicker devices possess an onset voltage below which hardly any current flows, and above which the current increases in a highly nonlinear fashion. No spin-valve signal has been detected in this conduction

Ref.	Device layout	d (nm)	Area (mm^2)	T (K)	V (mV)	R	R ($1mm^2$)
[152]	$Co/Al_2O_3/Alq3/Co$	20	0.1×0.1	2	20	86 MΩ	860 kW
[145]	LSMO/Alq3/MgO/Co	60	0.1×0.2	4.3		137.5 kΩ	2.75 kΩ
		12	0.1×0.2			1.16 kΩ	23 Ω
		12	$0.5{\cdot}10^{-3}$			60 MΩ	15 Ω
			$\times 0.5{\cdot}10^{-3}$				
[110]	LSMO/Alq3/CoFe	50	0.1×0.4	4.2	100	∼1.3 kΩ	52 Ω
				296		∼2.5 kΩ	100 Ω
[153]	Co/Ca/Alq3/Ca/NiFe	150	0.01×0.01	4.5	200	3.8 GΩ	380 kΩ
[109]	Fe/Alq3/Co	25		210	300		∼100 MΩ
[154]	LSMO/Alq3/Co	30	0.2×0.2	10	200	∼3 kΩ	∼120 Ω
[155]	LSMO/Alq3/Co	50	0.2×0.2	15	200	∼2 kΩ	80 Ω
	$LSMO/Al_2O_3/Alq3/Co$	50		10	230	∼360 kΩ	14 kΩ
[156]	Co/Alq3/Fe	64	0.8×0.8	120	200	300Ω	190 Ω
				300		1000Ω	640 Ω
[105]	$Co/Al_2O_3/Alq3/NiFe$	4	0.2×0.2	4.2	10	10^5 Ω	4 kΩ
				300		10^7 Ω	400 kΩ
[157]	$CoFeB/Al_2O_3/Alq3/Co$	4	0.3×0.3	300	1	1 Ω	90 kΩ
[158]	NiFe(LiF)/Alq3/FeCo	150	2×2	10	100	∼2.5 kΩ cm^2	250 kΩ
	NiFe/Alq3/FeCo	150	2×2	10	100	∼3.3 kΩ cm^2	330 kΩ
[108]	LSMO/Alq3/Co	93	∼1×2	10	500	160 MΩ	320 MΩ
[159]	CoFe/MgO/Alq3/CoFe	8		RT	10	15 MΩ mm^2	15 Ω
[160]	Co/Alq3/Fe	140	2×3	100	300	500 kΩ	3 MΩ
				294		200 kΩ	1.2 MΩ
[161]	LSMO/Alq3/Co	40	1×1	125	2	>10 kΩ	>10 kΩ
[2]	LSMO/Alq3/Co	130	2×3	11	2-3	10^4-10^5 Ω	60-600 kΩ
[162]	$Co/Al_2O_3/Alq3/C0$	96	1.5×3	80	<150	275 kΩ	1.2 MΩ

Table 4.1: Summary of recent results from the literature about Alq3-based vertical structure.

mode. Moreover, as shown in figure 4.4, thin devices typically have a metallic temperature dependence up to about 250 K, while the charge transport in thick devices results thermally activated. In the next paragraphs the two transport regimes are treated separately.

We also reviewed the data available from the literature about Alq3-based spin valves. Resistance values taken at low bias voltages have been summarized in table 4.1 and reported in figure 4.5, after being rescaled for the active area in order to be compared to our results. A good conductivity is generally shown at low vol-

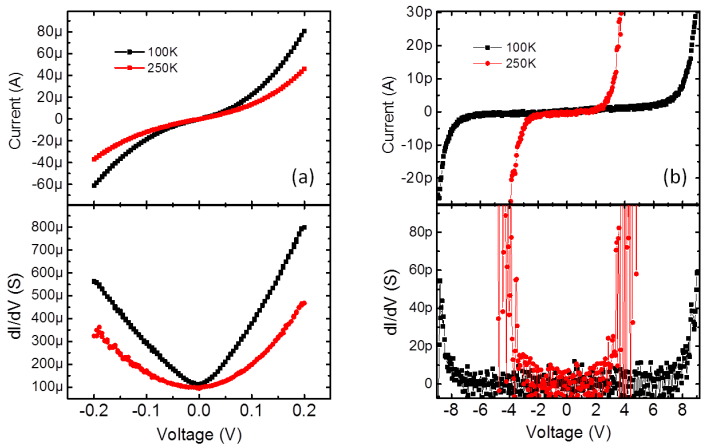

Figure 4.4: Comparison between I-V and G-V characteristics measured in devices with respectively a 15 nm(a) and a 60 nm(b) thick organic layer.

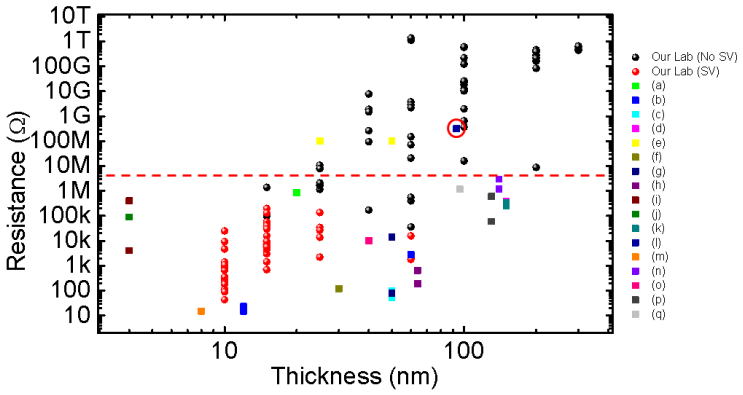

Figure 4.5: Comparison between the resistance values measured on our devices and those reported in the recent literature. With red and black circles are indicated our devices, respectively with and without SV signal. Squares represent the values from literature:
(a) Galbiati et al. [152], (b) Göckeritz et al. [145], (c) Grünewald et al. [110], (d) H.J.Jang et al. [153], (e) J.S.Jiang et al. [109], (f) S.W.Jiang et al. [154], (g) S.W.Jiang et al. [155], (h) Liu et al. [156], (i) Santos et al. [105], (j) Schoonus et al. [157], (k) Schulz et al. [158], (l) Sun et al. [108], (m) Szulczewski et al. [159], (n) Wang et al. [160], (o) Wang et al. [161], (p) Xiong et al. [2], (q) Zhang et al. [162]. The resistances have been normalized in order to be compared to our 1×1 mm^2 active area. All the magnetoresistive devices lie below the red dashed line, apart from the spin valves reported by Sun et al. [108] (red circle).

tages for magnetoresistive devices. Moreover, when G-V characteristics are given, they show a near-parabolic behavior similarly to our thin devices. This indicates that spin valve signals and the former conduction regime are generally closely related. We point out that in this regime no dependence of the resistance on the OS thickness can be found, as can be observed in figure 4.5, and both metallic and semiconductive temperature dependence have been observed.

4.2 Thick Alq3 spacer layer

4.2.1 Electrical characterization of thick devices

At low bias voltages (<1 V), thick devices show resistances up to 1 TΩ. For this reason we addressed the problem of the instrumental limit. In order to estimate this limit, we measured the Keithley 236 and Keithley 708 internal resistances in series with the external circuitry resistance. Figure 4.6 shows the I-V characteristics taken with no sample connected, at 100K and at 300K. Comparing these

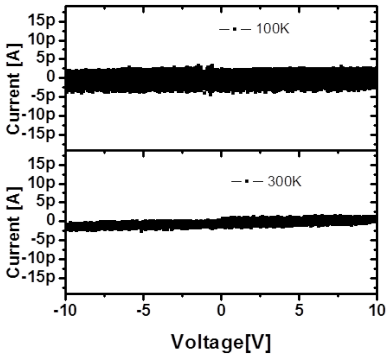

Figure 4.6: IV measurement taken with no sample connected. We measured the Keithley 236 and Keithley 708 internal resistances in series with the external circuitry resistance in order to estimate the instrumental limit at 100 K and at 300K.

characteristics with the ones of the most resistive samples, we are confident that the measurements have been carried out well below the instrumental limit. The linear fits conducted on the open-circuit's characteristics show, indeed, a resistance higher than a hundred TΩ.
The two key features of charge transport in high-resistance devices are the strong

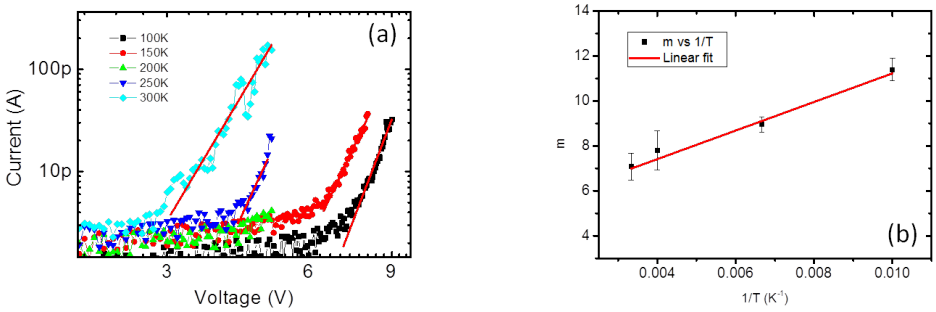

Figure 4.7: (a) I-V characteristics measured on a device with a 60 nm thick organic layer at several temperatures. Fit curves obtained from equation 4.2 are shown (red lines). (b) The parameter $m = T_t/T$ plotted as a function of 1/T. The slope of the linear fit represent the characteristic temperature T_t of the traps.

dependence of resistance on temperature and the non-linearity of the I-V characteristics, compatible with models commonly used for transport in organic material. Figure 4.7 shows the I-V characteristics at different temperatures of one such device. Above a threshold voltage, the current shows a power law dependence on the applied bias, and the exponent of the power law decreases at increasing temperatures. This is coherent with trapped charge limited current (TCLC), described in paragraph 1.1.2. In this model there is an exponential distribution of traps $N_t(E)$ below the LUMO of the molecule:

$$N_t(E) = \left(\frac{N_t}{kT_t}\right) exp\left(\frac{E - E_{LUMO}}{kT_t}\right), \tag{4.1}$$

where T_t is the characteristic temperature of the distribution and N_t is the total trap density. Above a threshold voltage, the current density-voltage characteristic is given by:

$$J_{TCLC} = N_{LUMO}\mu_n q^{1-m}\left(\frac{\epsilon m}{N_t(m+1)}\right)^m \left(\frac{2m+1}{m+1}\right)^{m+1} \frac{V^{(m+1)}}{d^{(2m+1)}} \tag{4.2}$$

where $m = T_t/T$ and N_{LUMO} is the density of the state in the LUMO band. The values for the parameter m, obtained by fitting the I-V characteristics (figure 4.7) with equation 4.2, have been plotted versus the reciprocal temperature. Performing a liner fit by setting both the intercept and the slope parameters free, we do not obtain a straight line through the origin, as should be expected from equation $m = T_t/T$. This deviation from the prediction of the model was already observed

by other groups [34]. In the example reported in figure 4.7b, we obtained a characteristic temperature of the traps T_t=(636 ± 57)K. This is equivalent to $E_t > 2\ k_BT$ at room temperature, indicating that most of the traps are deep traps as required by the model. A great variability of the trap depth have been obtained, with E_t ranging from $\sim 1\ k_BT$ to $\sim 4\ k_BT$ in our devices. A further test for the validity of the TCL model is the prediction that $V \propto d^2$ at constant current [26]. Such a proportionality has not been observed in our devices. A possible explanation is that the trap energy distribution varies from sample to sample, due to the fact that the fabrication parameters are not perfectly reproducible. It can also be attributed to the diffusion of the top electrode into the organic material, which can prevent a correct estimation of the spacer layer thickness d. As underlined by Burrows and coworkers [26], a small error in determining d leads to a disproportionately large change in J, making this fit subject to error. Furthermore, spatial non uniformities in the trap density are expected near the electrodes, due to the diffusion of the electrode material into the organic layer. Finally this model requires a mobility independent of the electric field. However this is not fulfilled by Alq3, as it is known from mobility measurements [163, 164].

In order to take into account the field dependence of the mobility, we analyzed the temperature dependent I-V characteristics also in the framework of trap-free SCLC model with a Poole-Frenkel like field dependent mobility, described above in paragraph 1.1.2. The current as a function of the bias voltage density becomes

$$I_{SCLC}^{PF} = \frac{9}{8} S\epsilon \frac{(V - V_{bi})^2}{d^3} \mu_{PF} \quad exp\left(-\frac{\Delta E}{k_B T_{eff}} + \frac{\beta_{PF}\sqrt{V - V_{bi}}}{k_B T_{eff}\sqrt{d}} \right) \tag{4.3}$$

where S is the active area of the device, V_{bi} is the built-in voltage, μ_{PF} is the Poole-Frenkel mobility pre-factor, ΔE is the activation energy at zero field, and β_{PF} is the so called Poole-Frenkel pre-factor. T_{eff} is the effective temperature, given by the relation

$$\frac{1}{T_{eff}} = \frac{1}{T} - \frac{1}{T_0} \tag{4.4}$$

where T is the absolute temperature and T_0 is an empirical parameter. The equation 4.3 can be simplified by grouping the physical parameters in A, B, C parameters:

$$I = A(V - C)^2 exp(B\sqrt{V - C}) \tag{4.5}$$

where

$$lnA = ln\left(\frac{9}{8}S\epsilon\frac{\mu_{PF}}{d^3}\right) + \frac{\Delta E}{k_B T_0} - \frac{\Delta E}{k_B T}, \tag{4.6}$$

$$B = -\frac{\beta_{PF}}{k_B T_0\sqrt{d}} + \frac{\beta_{PF}}{k_B T\sqrt{d}}, \tag{4.7}$$

$$C = V_{bi}. \tag{4.8}$$

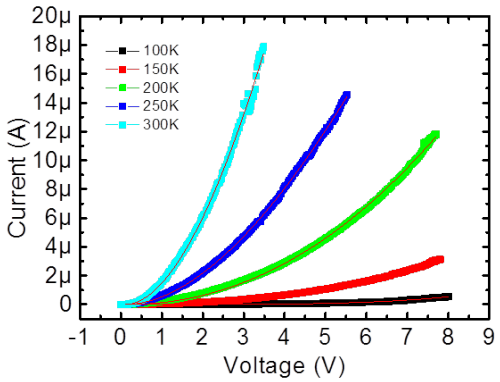

Figure 4.8: I-V characteristics measured on device with a 40 nm thick organic layer at several temperatures. Fit curves obtained from equation 4.5 are shown (red lines).

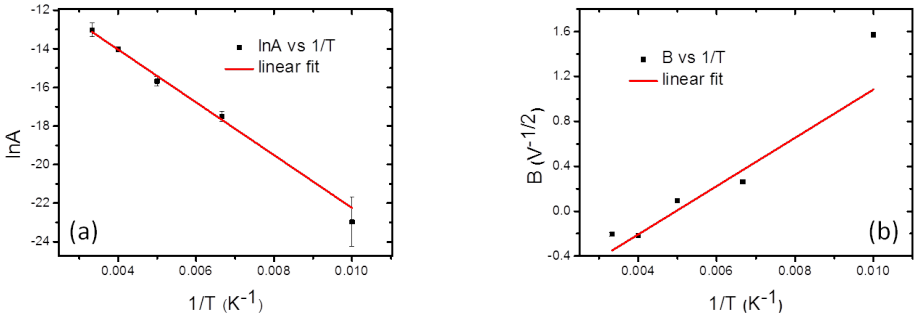

Figure 4.9: lnA (a) and B (b), obtained from fits in figure 4.8, plotted as a function of the inverse temperature. From the linear fits performed on these curves the physical parameters of equation 4.3 are extrapolated.

An example is given in figure 4.8, where the I-V characteristics at different temperatures are reported for a high-resistance device. The values for ln(A) and B,

obtained by fitting the curves with equation 4.5, have been plotted as a function of the inverse temperature (figure 4.9). From the linear fit in figure 4.9, the physical parameters of equation 4.3 are extrapolated: $\beta_{PF} = 5.93 \times 10^{-25} J(\frac{m}{V})^{\frac{1}{2}}$, $T_0 = 223K$, $\Delta E = 1.89 \times 10^{-20} J$, equivalent to $\sim 120\, meV$, $\mu_{PF} = 3.54 \times 10^{-8} \frac{cm^2}{Vs}$, consistent with values from the literature about Alq3 [165, 34]. Thus both the models we used are able to describe the behavior of our high resistance devices, even if sometimes the voltage range of validity is limited, and in general it is not possible to choose one of them unambiguously.
In figure 4.10a the resistance values of thick devices, measured in the low voltage region, are plotted as a function of thickness.

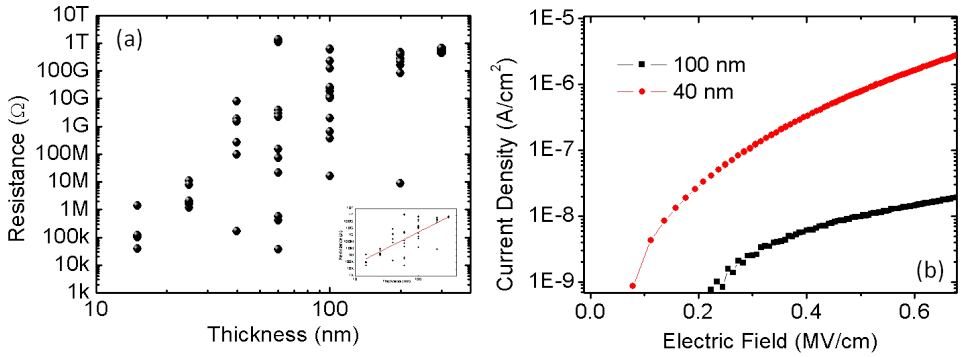

Figure 4.10: (a) Resistances of the devices taken in the low voltage region (<1 V) plotted as a function of thickness. In the inset a power law fit is shown. (b) Richardson-Schottky plots of two different samples measured at 100 K.

We tried to estimate the thickness dependence of the resistance by fitting the reported values (inset of figure 4.10a) finding a power law with an exponent $m \simeq 5$. However, the high dispersion of the resistance values does not allow any speculation, and an injection limited regime, theoretically independent on the thickness, can not be ruled out. We considered both Fowler-Nordheim (FN) tunneling and Richardson-Schottky (RS) thermionic emission. The former model can be excluded because of the small temperature dependence predicted, which is in contrast to the observed behavior. The latter predict a linear dependence of log(J) on the square root of the electric field [34]. The RS plots reported in figure 4.10b clearly show that the the current does not obey such a linear dependence in our devices. More-

over, at a fixed voltage, the current as a function of temperature is expected to follow the law $ln\left(\frac{J_{RS}}{T^2}\right) \propto \frac{1}{T}$, which is also not fulfilled by our data.
To conclude, the I-V characteristics of high-resistance samples indicate a thermally activated transport, showing features compatible with the models commonly used to describe organic devices (TCLC and SCLC enhanced by a field and temperature dependent mobility). The high dispersion of the resistance values as a function of thickness prevent us from establishing if the transport is bulk limited or interface limited, even if the two classical model for injection in semiconductors (FN and RS) have been ruled out. As argued by several groups [34, 32], in fact, the only reliable proof to distinguish between the two regimes is the thickness dependence of the current density at a fixed applied field.

4.2.2 Absence of magnetoresistive effects in thick devices

Magnetoresistive characterizations have been carried out as described in paragraph 3.2. In figure 4.11 are reported the typical MR curves taken on a thick device at -0.1 V. As shown, no magnetoresistance effects can be observed in the

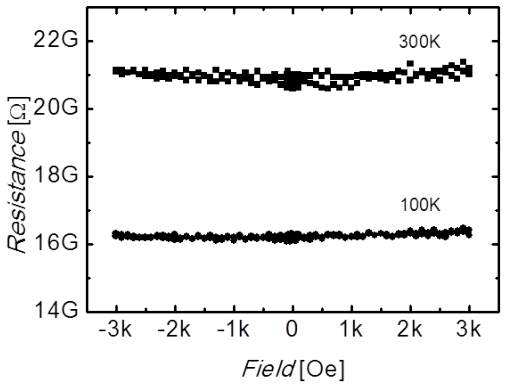

Figure 4.11: MR curves measured at the reading bias of -0.1 V on a device with a 60 nm thick Alq3 layer at different temperature. No spin valve signal was observed, even at bias voltages up to 8 V.

field range from -0.3 T to 0.3 T. We obtained the same result for all the investigated bias voltages, up to 8 V.

4.3 Thin Alq3 spacer layer

4.3.1 Electrical characterization of thin devices

Thin devices typically have a good conductivity even at low bias voltages (∼mV), as can be observed in the I-V characteristics and in G-V traces reported in figure 4.12. This rules out any injection barrier, contrary to what is expected

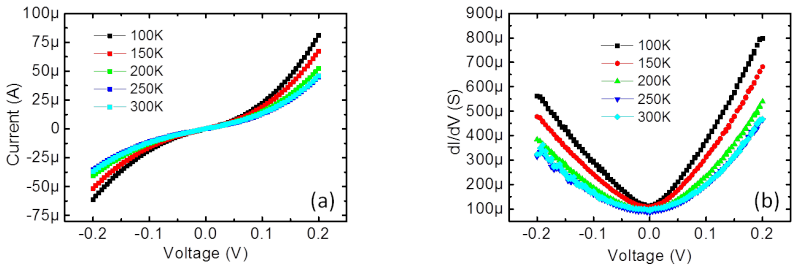

Figure 4.12: (a) I-V characteristics measured on a device with a 15 nm thick Alq3 layer at different temperatures. (b) Differential conductance G(=dI/dV) as a function of V.

both for LSMO/Alq3 and Alq3/Co interfaces. Moreover G-V curves show approximately a parabolic dependence on voltages, suggesting that the charge transport could be attributed to a tunneling mechanism. In figure 4.13 the traces measured at 100 K and 300 K have been normalized and fitted with the model of Brinkman, Dynes, and Rowell (BDR) [166]. They considered an elastic tunneling through a trapezoidal barrier in the WKB approximation, obtaining the expression:

$$\frac{G(V)}{G(0)} = 1 - \left(\frac{A_0 \Delta\varphi}{16\bar{\varphi}^{3/2}}\right) eV + \left(\frac{9}{128}\frac{A_0^2}{\bar{\varphi}}\right)(eV)^2 \tag{4.9}$$

where $\Delta\varphi = \varphi_2 - \varphi_1$ is the difference between the work functions of the electrodes (barrier asymmetry), A_0=$4(2m)^{1/2}$ $d/3$ $\hbar$, and G(0)=(3.16× 10^{10} $\bar{\varphi}^{1/2}/d$)exp(-1.025)$d\bar{\varphi}^{1/2}$. At room temperature the curve is in good agreement with the model, however at low temperatures the voltage dependence deviates from the parabolic behavior. Such a deviation from the parabolic dependence at low temperatures can be explained by using an inelastic tunneling model, involving multiple steps. The differential conductance traces have been fitted by using Glazman and Matveev (GM) model [167] (shown in figure 4.14a) , which is commonly used to describe inelastic tunneling through a grain boundary region [168]. According to this theory

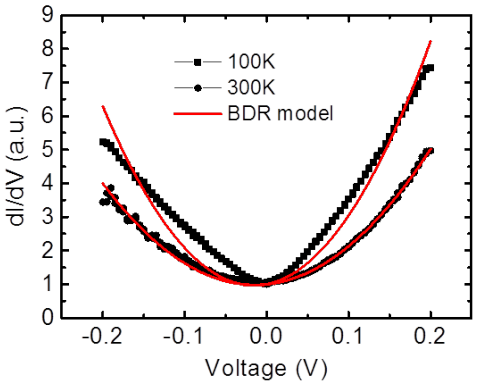

Figure 4.13: Normalized G(V) curves fitted with BDR model. For clarity only the extreme temperature 100 K and 300 K have been reported.

(for $eV \gg k_BT$)the I-V characteristics are given by

$$J = J_0V + J_{7/3}V^{7/3} + J_{7/2}V^{7/2} + ... \tag{4.10}$$

The voltage dependence of conductance G may be written as

$$G = G_0 + G_{4/3}V^{4/3} + G_{5/2}V^{5/2} + ... \tag{4.11}$$

where the terms in the right-hand side of Eq. 4.10 and Eq. 4.11 show tunneling via one, two, and three impurity states, respectively. Elastic tunneling contribution is similar to that via an impurity state and is included in the first term. As shown in figure 4.14a this model fits quite well the experimental curves but neglects the barrier asymmetry, assuming the two electrodes made of the same material. In our devices the difference between the work functions of the electrodes is not negligible, and a negative bias voltage shift of the differential conductance can be observed. In order to take it into account a linear term has been added to the equation 4.11, becoming

$$G = G_0 + G_{lin}V + G_{4/3}V^{4/3} + G_{5/2}V^{5/2} + ... \tag{4.12}$$

Figure 4.14b shows the fit performed using the equation 4.12. The fact that I-V characteristics at higher temperature are more nonlinear than those at lower temperatures may be understood in terms of the temperature dependence of the parameters $G_0, G_{4/3}, G_{5/2}$ (figure 4.14c). At higher temperatures, multistep tunneling contributions (that have higher exponents of voltage) increase, and this

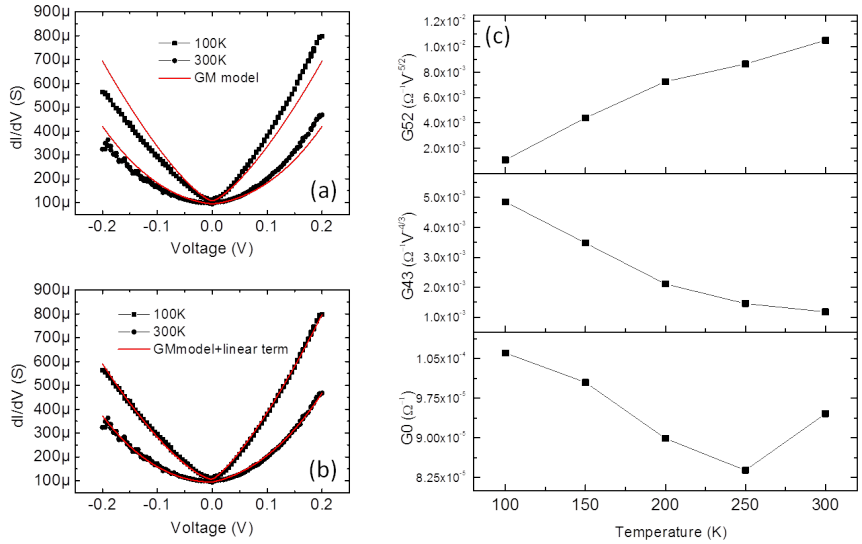

Figure 4.14: G(V) traces taken on a thin device (15 nm thick organic layer) fitted respectively with (a) equation 4.11 and (b) equation 4.12. (c) Fitting parameters obtained from (b) plotted as a function of temperature.

leads to increased nonlinearity of the I-V characteristics [168].
Since the observed tunneling regime is compatible with a barrier thickness of about 2-3 nm, this indicates that shortenings take place in the organic barrier, nominally 15 nm thick in the device studied above.

4.3.2 Resistance as a function of temperature and parallel circuit model

The analysis of the I-V characteristics shown above demonstrates that the charge transport in thin devices can be described as tunneling through a disordered barrier. However the temperature-dependent resistance measurements suggest the presence of metallic paths across the junction. Usually the R(T) curves, indeed, show a positive derivative dR/dT over a wide range of temperatures, usually below room temperature (RT). This does not fulfill the third of the Rowell's criteria [169], commonly used to prove the absence of pinholes in a tunnel junction:

1. the exponential thickness dependence of the current;

2. the parabolic shape of the differential conductance as a function of voltage;

3. the downward temperature dependence of the conductivity.

Moreover, because of the large dispersion of the resistance values as a function of thickness, we can not clearly identify an exponential thickness dependence of the current. Finally it has been pointed out that the purely classical pinhole conduction can mimic both the thickness dependence and the non linear behavior of the I-V characteristics attributed to a tunneling process [170, 171]. For these reasons metallic filaments have been taken into account in the following analysis in order to explain the peculiar temperature dependence of the junction resistance and properly modeling the structure of thin devices.
Looking at the R(T) of the device in figure 4.15, it can be observed that dR/dT changes sign from positive to negative at a crossover temperature, which is typically in the range 220 K - 230 K. From the comparison with the R(T) of the relative LSMO electrode, we rule out that the smooth peak is due to the metal-insulating transition of the bottom electrode. In fact, this transition always occurs at much larger temperatures in our LSMO films (usually above 350 K). Moreover the device peak is not always at the the same distance on the T-axis from the peak of the corresponding LSMO electrode. It should be mentioned that this feature in R(T) characteristics has already been observed in magneto tunnel junction (MTJ) with an LSMO electrode [172, 173, 174] and Viret et al. [173] argued that it can be attributed to an oxygen-deficient layer at LSMO surface, based on the reduction of the transition temperature in underdoped manganite. However, as pointed out by Galceran et al. [175], an upward shift in temperature of the R(T) peak under the application of a high mangetic field should be expected in this case, due to the CMR effect (see paragraph 1.2.4). The absence of any shift with 9 T applied strongly suggests that the peak has a different origin. Moreover a change in the sign of dR/dT has been observed also in organic spin-valves with Fe instead of LSMO as bottom electrode [119], and in MgO-based MTJ with CoFe films as electrodes [176]. We interpret the peak as the result of a competition between metallic and thermally-activated transport across the junction. Here I point out that the microscopic nature of the metallic-like filaments is not clear, yet. Both metal-metal nanocontacts [177, 178] and delocalized states across the disordered AlOx barrier [179] can occur. The model introduced below just gives

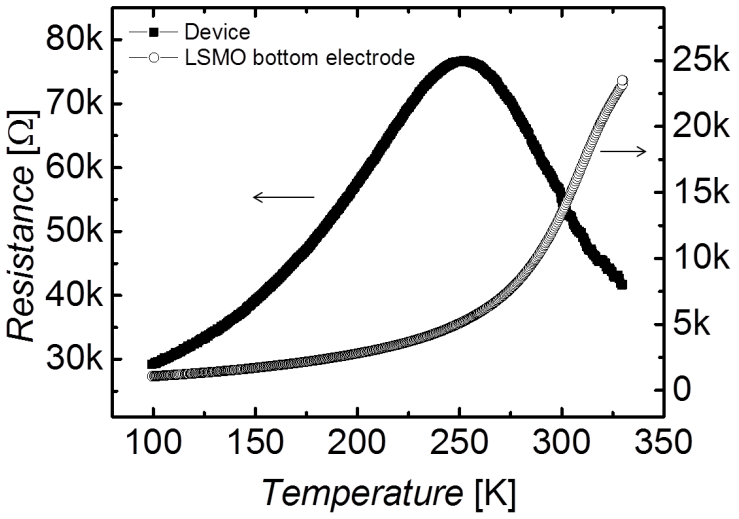

Figure 4.15: R(T) measured on a device with a 15 nm thick Alq3 layer (black squares) and on the corresponding LSMO electrode (empty circles). The fit obtained from equation 4.18 is shown.

a phenomenological description based on the analysis of the R(T) characteristics. Ventura and coworkers [176] developed a simple model to describe the effect of metallic pinholes on their MgO-based magneto-tunnel-junctions (MTJs). They consider a tunnel resistance (R_t) and a metallic resistance (R_m) in parallel, so that the total resistance is given by

$$\frac{1}{R(T)} = \frac{1}{R_t(T)} + \frac{1}{R_m(T)}. \tag{4.13}$$

They assumed $R_t(T)$ and $R_m(T)$ to be linear functions of temperature, respectively

$$R_t(T) = R_{to} + \alpha_t T \tag{4.14}$$

and

$$R_m(T) = R_{mo} + \alpha_m T, \tag{4.15}$$

where R_{to} and R_{mo} are the resistances at T=0 K and α_t and α_m the slopes for the two channels. However this assumption does not hold for our R(T) characteristics, due to their non linearity at low temperatures. For this reason we replaced the linear resistivity attributed to the metallic filaments with the Bloch-Grüneisen

formula, which accounts for electron-phonon scattering:

$$\rho_{BG}(T) = \rho_o + \rho_{el-ph}(T), \tag{4.16}$$

with

$$\rho_{el-ph}(T) = \alpha_{el-ph}\left(\frac{T}{T_D}\right)^5 \int_0^{\frac{T_D}{T}} \frac{x^5}{(e^x-1)(1-e^{-x})}dx. \tag{4.17}$$

α_{el-ph} is a constant $\propto \lambda_{tr}\omega_D/\omega_p^2$, where λ_{tr} is the electron-phonon coupling constant, ω_D is the Debye frequency and ω_p is the plasma frequency. T_D is the Debye temperature. The fitting equation is then obtained by

$$R(T) = \left(\frac{1}{R_t(T)} + \frac{1}{R_{BG}(T)}\right)^{-1}, \tag{4.18}$$

where R_{BG} is given by the resistivity in equation 4.16 multiplied by a geometrical factor included in the free parameters. As can be observed in figure 4.16a, the curve

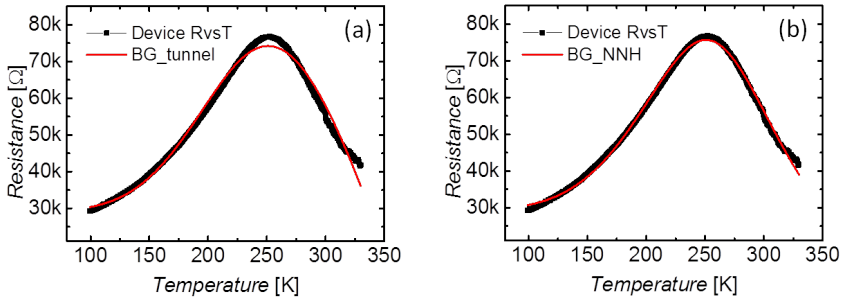

Figure 4.16: The R(T) shown in figure 4.15 has been fitted by using two different equivalent circuit models. A metallic channel with a temperature dependence given by the Bloch-Grüneisen formula (eq. 4.16) is considered in parallel with (a) a tunnel resistance (eq. 4.14) and (b) a neighrest-neighbor-hopping-like temperature dependent channel (eq. 7.3). A good agreement with the experimental result has been found with the second model.

is not perfectly described by the equation 4.18. In fact, the term $R_t(T)$ can not take into account the deviation from linearity observed at temperature T > 300 K. Moreover we obtained $R_{to} = (3.5 \pm 0.1) \cdot 10^5\ \Omega$ and $\alpha_t = (-935\ \pm\ 40)\ \Omega\ K^{-1}$, which give a ratio $R_t(0K)/R_t(300K)\ >\ 5$, much higher than the one observed in Al_2O_3/Alq3 tunnel junctions by Santos et al. [105]. This means that a mechanism with a stronger temperature dependence must occur. Typically, in this temperature range, the nearest neighbor hopping (NNH) model is used to describe

both disordered inorganic systems and organic materials [180]. Then the tunnel resistance R_t in equation 4.18 has been replaced by

$$R_{NNH}(T) = R_o exp\left(\frac{T_o}{T}\right), \tag{4.19}$$

A good agreement with the measured curve has been found, as shown in figure 4.16b. For the metallic channels we obtained a Debye temperature $T_D = (1442 \pm 27)\ K$, which is much higher than the typical Debye temperature of Co [181] and LSMO [182], but compatible with the one measured in polycrystalline AlOx [183]. This might indicate that conductive paths occur through the insulating AlOx barrier. Low-energy extended electron states in thin and disordered oxide barrier, indeed, have been observed [179]. However one should be cautious while comparing the bulk temperature reported in the literature and the one relative to the conductive filaments. On the other hand the obtained activation energy for the NNH regime is $\Delta E_{NNH} = (174 \pm 10)\ meV$, which is compatible with the values from the literature about Alq3 [32].
Thus, thin devices can be described as a parallel between filaments with a metallic temperature dependence, presumably conductive path in the insulating AlOx barrier, and a hopping channel in the organic bulk.

4.3.3 Magnetoresistance in thin devices

Devices belonging to this conduction regime typically show spin-valve signals in the voltage range from about -0.5 V to 0.5 V, with absolute values up to 22% at 100 K. Here the MR amplitude is defined as (R_{max}-R_{min})/R_{max}, as illustrated in figure 4.17. The magnetoresistive properties of our devices have been deeply studied in the last years [150, 107, 5, 6, 9], and the negative sign of the magnetoresistance is a well consolidated result, reproducing the observations of many other groups which studied the same structure (LSMO/Alq3/Co) [2, 161, 106, 108]. However it should be mentioned that several others found also positive MR [145]. In addition, it has been pointed out that the MR sign can change depending on to the bias voltage [154, 155]. A comprehensive explanation for these controversial results is still lacking, but several theoretical models have been proposed. As already shown in paragraph 1.3.4, Barraud et al. [144] suggested that the hybridized molecular states at the interface can result strongly modified with respect to the

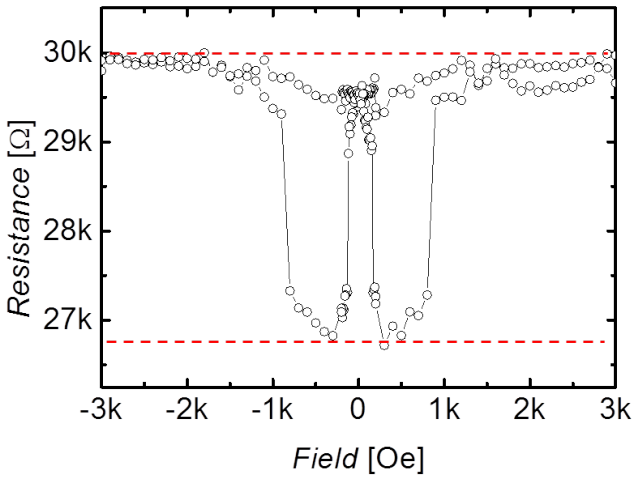

Figure 4.17: MR curve measured on a device with a 15 nm organic layer at a bias voltege of -0.1 V and a temperature T = 100 K. The red dashed lines indicate R_{max} and R_{min}.

bulk states, and new peaks in the DOS could appear at the Fermi level E_F. This new DOS determines the spin-polarization of the injected current, which can be dramatically different, and even reversed, compared with the polarization of the electrodes. Another model has been proposed by Kim [184], who carried out a theoretical study of the inverse TMR effect in magneto tunnel junctions (MTJs). In the weak tunneling limit, he finds the ordinary positive TMR. The sign changes as the transmission probability becomes large close to a unity. Thus the result might be relevant to the MTJs with a pinhole or a quantum point contact. This study is not strictly related to organic devices. In fact, the inverse MR is still an open question also for inorganic spintronics.

De Teresa et al. [185] studied oxide barriers ($SrTiO_3$ (STO), AlOx, STO/AlOx) sandwiched between LSMO and Co electrodes, showing negative MR with STO and positive with AlOx. The result was ascribed to the bonding effects at the transition metal/barrier interface. This made us exclude a direct tunneling through the AlOx barrier in our devices [9], otherwise a positive MR should be expected. However, in a recent comparative study we carried out on LSMO/AlOx/Co MTJs (not published yet), we found both positive and negative magnetoresistance (figure 4.18), indicating that a direct tunneling through the oxide barrier can not be

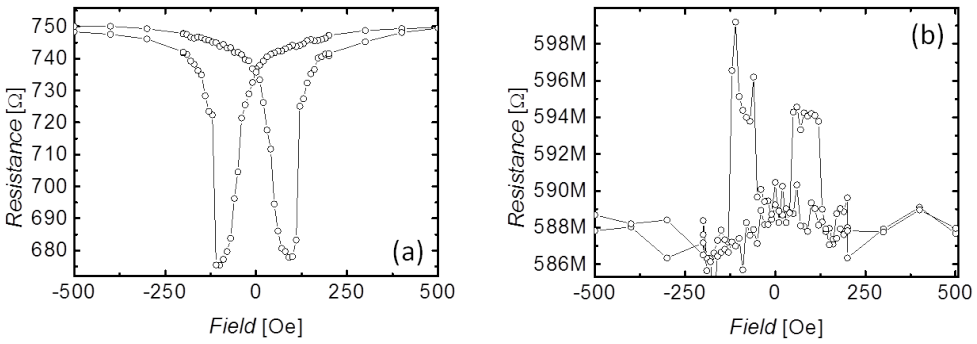

Figure 4.18: MR curves of LSMO/AlOx(5 nm)/Co devices grown on the same substrate, taken at V=-0.1 V and T=100K.

ruled out in thin organic devices. Moreover, while MTJs with a positive MR have a resistance on the order of hundreds of MΩ (figure 4.18b), the one with the negative resistance has a resistance in the order of kΩ (figure 4.18a). This would be compatible with the picture of Kim [184]. A similar explanation can be found in the theory for ballistic magnetoresistance (BMR) across conductive nanocontacts, proposed by Garcia et al. [177, 178]. For the simplest case of identical ferromagnetic electrodes at both sides of the nanocontact,

$$BMR = \frac{R_{AP} - R_P}{R_P} = \frac{2P^2}{1 - P^2} \times F(\lambda, k_F), \tag{4.20}$$

where R_{AP} and R_P are the resistance for the parallel and antiparallel configuration, $P = (N_\uparrow(E_F) - N_\downarrow(E_F))/(N_\uparrow(E_F) + N_\downarrow(E_F))$ is electron polarization assuming that electrons s and d have the same ballistic transmissivity, approximately unity, through the contact. F is a function describing the domain-wall scattering or nonspin conservation in the current; the arguments are respectively the domain wall width λ and the Fermi vector k_F. When λ is very small (a few atomic layers), then $F \sim 1$ and the equation 4.21 becomes identical to the Julliere's formula [50] for TMR

$$TMR = \frac{2P^2}{1 - P^2}. \tag{4.21}$$

Garcia and coworkers [178] argued that it is not possible to experimentally distinguish between BMR and TMR by means of magnetoresistance measurementes and I-V characteristics because they are due to the same physical principals (they

are both ballistic process) and are obtained by matching the wave functions of both sides of the contact. However, from a theoretical point of view, if one takes into account that for the nanocontact the transmissivity t is almost 1 while in tunneling it decays exponentially with the junction thickness, a different electron polarization can emerge for the two regimes. Indeed, for $3d$ metals, band-structure calculations show that $N_{s\uparrow}(E_F) > N_{s\downarrow}(E_F)$ [186] and can justify the posistive polarization of cobalt for tunneling, when s electrons dominates. On the other hand, $N_{d\downarrow}(E_F) \gg N_{d\uparrow}(E_F), N_{s\uparrow}(E_F), N_{s\downarrow}(E_F)$ [186], and given that $t_s \sim t_d \sim 1$ for the conductive nanocontact, the negative spin polarization can be explained. Despite further investigations are needed to confirm the result in figure 4.18 and quantitatively describe the underlying mechanism, this represents a plausible picture for the description of our devices, especially considering the metallic temperature dependence of the resistance.

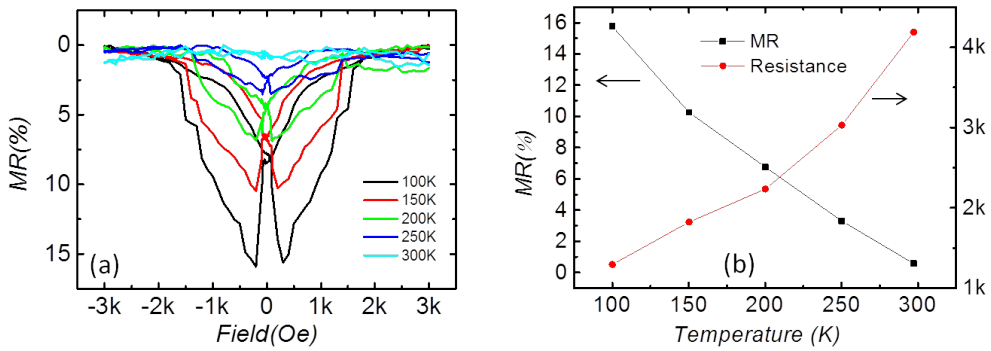

Figure 4.19: (a) MR curves taken on a low-resistance device at different temperatures. (b) The MR values are plotted as a function of temperature and compared to the resistance values of the device.

Typically MR values decrease at increasing temperature vanishing below RT, as illustrated in figure 4.19, and a clear correspondence between metallic behavior in R(T) and the presence of a SV signal was observed for all the studied devices (figure 4.19b). Considering the parallel circuit model used above to describe thin devices, this correspondence strongly suggests that the metallic channels are responsible for magnetoresistive effects. This guess is further supported by the analysis carried out in the paragraph 7.2, where it is shown that the MR can be

increased or decreased by turning ON and OFF the metallic channels by means of electrical switching. In the last years, our group [107] showed that the temperature dependence of the magnetoresistance data agree very well with that of the LSMO surface magnetization (SM) measured by Park et al. [90], as illustrated in figure 4.20. The SM represents the magnetization from the top 5 Å in a standard

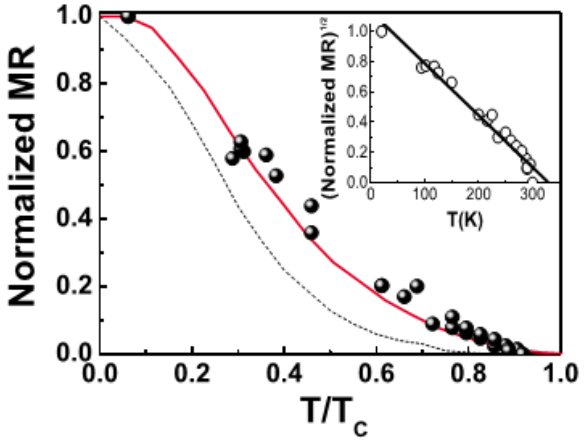

Figure 4.20: Comparison between spin-valve magnetoresistance MR (dots), the $La_{0.7}Sr_{0.3}MnO_3$ surface magnetization SM (solid line), and the polarized charge-carrier density PCCD (dotted line) data from Ref. [90]. The latter consists of the convolution of SM and the density of states at the Fermi energy. Both magnitudes are plotted in reduced temperature scale normalized to the Curie temperature T_C. The inset shows the linearized data [107].

LSMO film, as determined by spin-polarized photoemission spectroscopy and it is effectively the parameter of interest for device behavior. Even if from this study a different physical picture emerged with respect to the one proposed in ref. [107], the agreement between the device MR(T) and SM curve of the LSMO is still a consistent explanation for the temperature dependence of the spin-valve magnetoresistance.

To complete the picture, another controversial observation related to the switching fields should be mentioned. In fact, theoretically, the switching fields of the spin valve should correspond to the coercive fields H_c of the electrodes, as illustrated above in figure 1.13. However the former are often found to deviate from the expected values. As an example, in figure 4.21 are reported the MR of the electrodes relative to the device in figure 4.17. As can be observed, H_c(LSMO)=$\pm$40 *Oe*

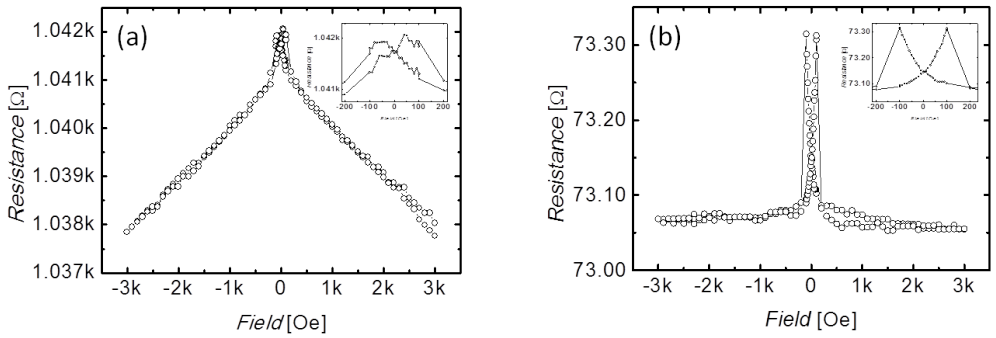

Figure 4.21: MR curve taken on the LSMO (a) and cobalt (b) electrodes of the device shown above. The curves are taken at the same bias voltage (-0.1 V) and temperature (100 K) as the device. As pointed out in the text the coercive fields of the electrodes do not correspond to the device switching field as one could expect.

and H_c(Co)=$\pm$100 Oe , while the internal H_c of the device are $\sim \pm 140$ Oe and the external $\sim \pm 800$ Oe in this case (figure 4.17). This can be qualitatively explained taking into account that conduction occurs via localized metallic paths, as discussed above. As a consequence the polarization of the injected electrons depends on the magnetic properties of this defects, which in principle can have local coercive field different from the average coercive field of the electrode, producing unexpected switching fields. This explanation is supported by the fact that the switching fields vary from device to device, while the coercive fields of the electrodes are the same. Moreover different switching fields are sometimes clearly distinguishable in the same device as discrete steps (figure 4.19a), and we interpreted this feature as the result of different sub-devices working in parallel [9].
To conclude, this analysis demonstrates that SV signals can be explained as TMR or BMR occurring across shortened regions of the organic bulk. This picture is compatible with the absence of Hanle effect, as will be argued in chapter 5. However it does not exclude that organic molecules can play an active role at the metal/organic interface. Indeed, the effects of the organic-induced hybridization on the electrode polarization are still an open question.

Chapter 5

Hanle effect missing in organic spin valves

Our spin valve devices have been carefully investigated [9] in order to detect the Hanle effect signature, which is accepted as the only reliable proof that spin transport across the OSC layer occurs. We considered the previously introduced expression for the GMR signal (see paragraph 1.3.2):

$$GMR \propto \int_0^{+\infty} \frac{1}{\sqrt{4\pi Dt}} \cdot e^{-\frac{(d-vt)^2}{4Dt}} \cdot [sin^2\theta cos(\omega_L t) + cos^2\theta] e^{-t/t_s} dt, \qquad (5.1)$$

where D is the diffusion constant, d the spacer layer thickness, and t_s the spin lifetime. Assuming a highly incoherent transport in the Alq3 spacer layer, the integral with the $\cos(\omega_L t)$ term vanishes and the GMR is proportional to $\cos^2\theta$. Therefore, if one applies the magnetic field perpendicular to the plane of the device (θ=90°), no GMR should be observed in this transport regime, as $\cos^2(90°)$=0. To verify this, we first set the magnetoresistive device respectively in the parallel (P) and antiparallel state (AP) by means of the procedure illustrated in figure 5.1. Then we measured the resistance in the two state by sweeping a magnetic field perpendicular to the device plane from -15 mT to +15 mT. It is not possible to predict whether the spin precession has the same effect on the individual resistances. However their difference should diminish when Hanle precession takes place [110]. In our case, as shown in figure 5.2, P and AP state are not affected by the perpendicular field, in other words the Hanle effect is not detected. These results confirm those presented in a paper we have recently published [9], as shown in figure 5.3. GMR was also measured as a function of θ (θ=0°, 45°, 60°), as shown in figure 5.4. No dependence of the GMR on θ has been observed, apart from the switching fields, which scale with 1/cos θ. This is due to the reversal

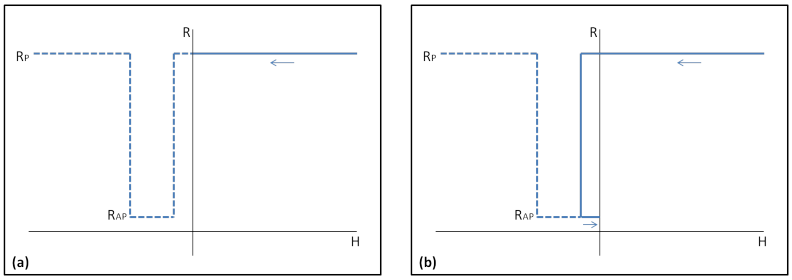

Figure 5.1: Schematic representation of the field sweeps required for the preparation of the parallel (a) and antiparallel (b) states of the device, starting from the positive saturation. Dashed lines represent the complete trace of the negative spin-valve signal ($R_{AP}<R_P$). The parallel state (a) is obtained by sweeping the in plane magnetic field from 3000 Oe to 0. The antiparallel state is obtained by decreasing the field from 3000 Oe to small negative values until the device resistance is switched.

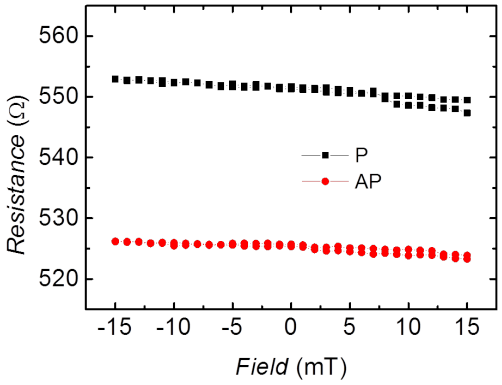

Figure 5.2: P and AP resistive state as a function of magnetic field applied perpendicular to the plane of the device.

magnetization process and is not related to the Hanle effect. The fact that the MR changes between R_{AP} to R_P in more than one step has been explained by describing the spin valve as a parallel of spintronic sub-devices, as schematically illustrated in the figure.

One possible reason for the absence of Hanle effect could be that the magnetization of the electrodes is aligned to the applied magnetic field. In this case the spin of the electrons would also be aligned to the applied magnetic field, and no precession could take place. This possibility has been ruled out by measuring the magnetization of Co on Si/Alq3(50 nm)/AlOx(2.5 nm) and a LSMO film with a

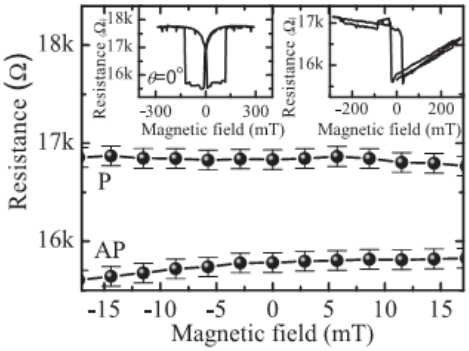

Figure 5.3: Resistance in the parallel (P) and antiparallel (AP) state of the device, with magnetic field applied at angle θ =90° from the plane of device. The top left inset shows the MR with the field in the plane of the device, while the inset on the top right shows the complete MR for θ=90°. The linear behavior at high field is due to the tilting out of plane of the magnetization of the electrodes [9].

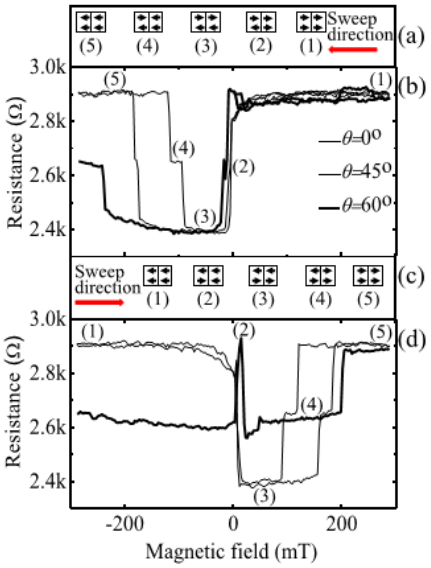

Figure 5.4: In (a) and (c) the boxes are a schematic representation of the device as the combination of two parallel sub-devices. The arrows indicate the orientation of the magnetization in each sub-electrode. Each sub-electrode has a different coercive field. In (b) and (d) MR at θ=0, θ=45°, θ=60° are shown. The unusual look of the MR for θ=60° is due to the fact that one of the switching field exceed the available range [9].

superconducting quantum interference device (SQUID) magnetometer (figure 5.5). At θ=90° and 20 mT, which is the upper limit of the magnetic field in figure 5.3, the out-of-plane magnetization of LSMO and Co is indeed negligible.

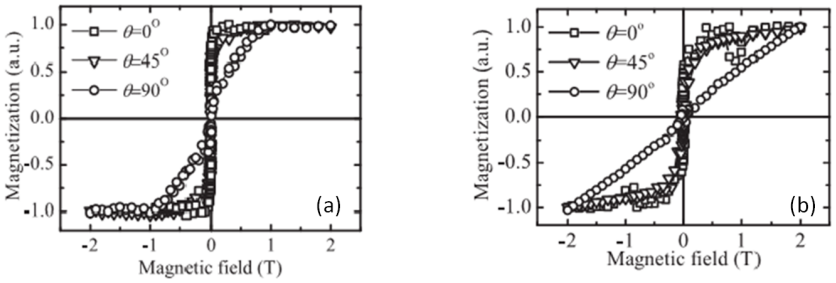

Figure 5.5: Hysteresis loops obtained by SQUID magnetometry at 100 K for a 20 nm thick LSMO film (a) and for a 20 nm thick Co film grown on a AlOx(2.5 nm)/Alq3 (50 nm)/Si (b) with the magnetic field applied at different angles with respect to the film plane [9].

Moreover electron paramagnetic resonance (EPR) in Alq3 [187] has demonstrated spin precession of unpaired electrons in a non collinear magnetic field, showing that there are no fundamental reasons to exclude the presence of the Hanle effect in organic semiconductors. At this point the only possible explanation seems to be a short transit time compared to the precession time. Starting from the Larmor frequency expression, the precession time can be calculated as

$$t_{prec} = \frac{2\pi m_e}{eB_z} \tag{5.2}$$

Considering g=2, at a field of 20 mT the time for a full precession is ≈1.8 ns. With an accuracy of 10%, using $\cos(\omega_L t)$=90%, ω_L=3.52×10^{9}rad/s, the electrons would need to take less than ≈0.13 ns to cross the organic layer (d=200 nm for the device reported in ref. [9]) in order for the spin precession to go undetected. From the equation

$$t_{trans} = \frac{d}{v} = \frac{d}{\mu E} = \frac{d^2}{\mu V_{bias}}, \tag{5.3}$$

with an applied bias V_{bias}=-100 mV, this requires μ = 30 cm^{2}V^{-1}s^{-1}. The obtained value is orders of magnitude far from the measured mobility for Alq3, μ ≈10^{-6}cm^{2}V^{-1}s^{-1} [188]. This picture would be untenable even in the case of very thin organic regions, but still sufficiently thick to prevent direct tunneling across the Alq3 barrier (thicker than few monolayer). Similar estimation have

been done also by Grünewald et al. [110]. These results suggest the presence of TMR which can be caused by direct tunneling between the ferromagnetic electrodes at pinholes. This possibility was initially ruled out [9] because hot spots in which LSMO contacts directly the AlOx/Co top layer were expected to show positive MR [185]. However a recent comparative study which we carried out on LSMO/AlOx/Co MTJ (not published yet) demonstrates that negative MR can be observed even in this configuration, as already shown in figure 4.18. Tunneling process can thus be considered as a plausible reason for the absence of the Hanle effect in vertical organic spin valves. This explanation is compatible with parallel circuit model proposed in paragraph 4.3.2 giving a coherent physical picture.

Chapter 6

Distinguishing device MR and electrode-induced artifacts

As shown above, magnetoresistance (MR) effects have been observed only in low resistance devices, where locally thin Alq3 regions or metallic filaments occur. It has been argued that artifacts can originate from the inherent shortcomings of the cross bar configuration when the resistance of the device is small compared to that one of the electrodes [189]. In particular it has been shown that an increase (decrease) in the resistance of an electrode induces a decrease (increase) in the measured device resistance. Thus, if the electrodes are ferromagnetic (FM), their MR can show as a MR of the opposite sign in the device. As a bottom electrode we employed $La_{0.7}Sr_{0.3}MnO_3$ (LSMO) films, which in some cases are observed to have a resistance comparable or larger than the device resistance. For this reason we addressed the problem of distinguishing between tunnel magnetoresistance (TMR) and artifacts induced by the bottom electrode. With this aim in mind, I carefully studied the magnetoresistive properties of the LSMO films.

6.1 LSMO magnetoresistive characterization

In the last years our group studied in detail the LSMO deposition parameters to provide a set of optimal growth conditions [151]. TEM and AFM images reported in figure 6.1 demonstrate that atomically flat films with a well defined crystal structure have been obtained. The magnetic properties of LSMO films have been investigated by MOKE and SQUID techniques [151, 9] and the tran-

sport properties have been also deeply studied [190].

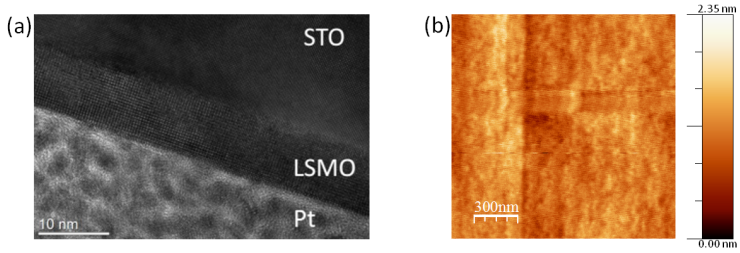

Figure 6.1: (a) TEM image performed on a 9 nm thick LSMO film epitaxially grown on a STO substrate by K. O'Shea, University of Glasgow. (b) AFM image taken on the same film [151].

I focused on the LSMO magnetoresistive properties measuring thin films R-H characteristics and studying their temperature dependence. The sketch in figure 6.2

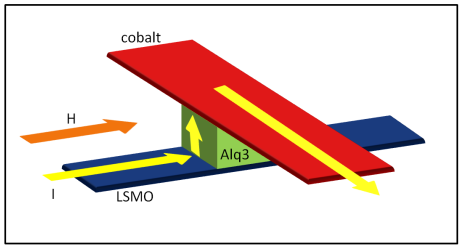

Figure 6.2: Schematic representation of a working device. The yellow arrows indicate the path of the current I. The magnetic field H is applied in the device plane, parallel to the LSMO stripe.

schematically represents a spin valve device while carrying out a R-H measurement. As shown, the magnetic field is oriented parallel to the direction of the current in the LSMO electrode ($I \parallel H$). With the aim to compare the bottom electrode MR curve with that of the device, two points (figure 6.3a) and four points (figure 6.5a) R-H characteristics of thin LSMO film have been measured in the $I \parallel H$ configuration. The two points MR curve (figure 6.3b) shows an almost linear field dependence of the resistance, typical for the well studied colossal magnetoresistance (CMR) effect. The amplitude of the CMR signal has been defined here as indicated by the red lines and studied as a function of temperature (figure 6.4). The manganite Curie temperature (T_C), defined as the linear extrapolation to zero of the MR part right to the peak [151], is larger than 320 K,

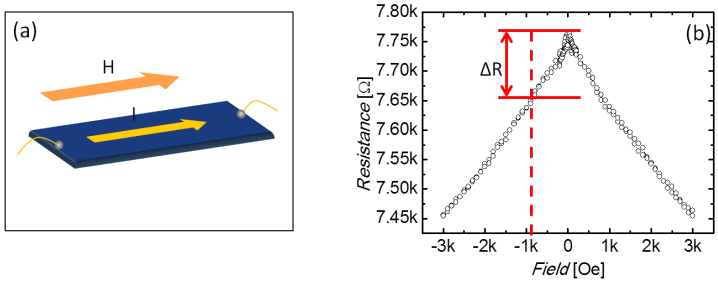

Figure 6.3: (a) Schematic representation of an LSMO stripe connected in a two point configuration. The magnetic field H is applied parallel to the current I. (b) CMR signal measured on a 9 nm thick LSMO film at 100 K. The CMR signal amplitude is here defined as CMR=ΔR/R, where ΔR=R(0)-R(800 Oe) as indicated by the red lines.

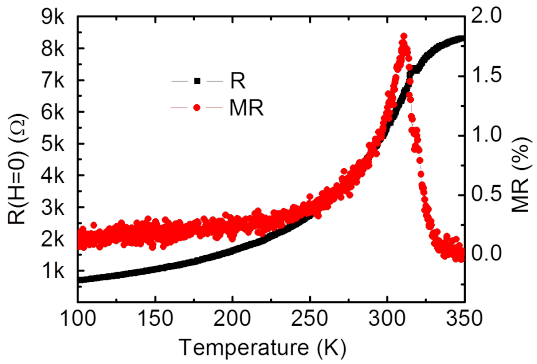

Figure 6.4: Resistance (R) and magnetoresistance (MR) measured on a 9 nm thick LSMO film plotted as a function of temperature. MR is defined in figure 6.3b.

while the R(T) curve shows a metal-insulator transition above 350 K, indicating that the films are potentially suitable for room temperature applications. On the other hand, the R-H characteristics performed in a four points configuration allowed us to observe a sharp deviation from the CMR linear behavior in the low field regime (H<600 Oe), as illustrated in figure 6.5c. Such low-field features have already been observed both in polycrystalline [100, 99] and single crystal LSMO films [102, 101, 99]. For polycrystalline films it has been explained as the effect of a field dependent scattering at the grain boundaries [99] or, alternatively, of an intergrain spin-polarized tunneling [100]. Li and coworkers [99] also showed that

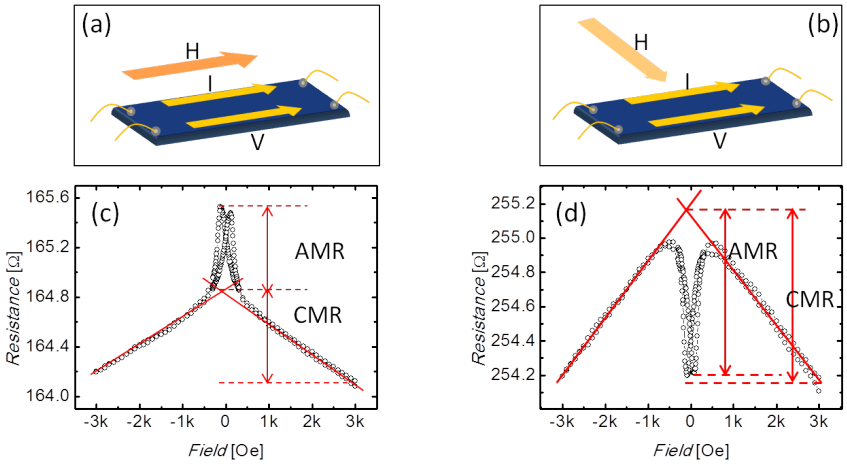

Figure 6.5: Schematic representation of an LSMO thin film connected in a four point configuration with a magnetic field applied (a) parallel to the current direction ($I \parallel H$) and (b) perpendicular to that ($I \perp H$). (c)(d) R-H characteristics measured at 200 K respectively in (a) and (b) orientation. It can be clearly observed an AMR contribution superimposed to the CMR signal. The red lines describe how the two magnetoresistive contributions have been disentangled.

in these systems the effect is almost independent on the relative orientation of the current and the applied field, indicating that the mechanism of anisotropic magnetoresistance (AMR) is not significant in polycristalline films. On the contrary, the epitaxial films display a positive MR when $I \parallel H$ as opposed to a negative MR when $I \perp H$. Moreover, while the low-field MR observed in polycrystalline films can reach values up to 15%, in epitaxial films it is usually well below 1%. Our films clearly show an AMR effect with a relative value below 1% (figure 6.5c-d). On the one hand this behavior further confirm the well defined crystal structure of our film. On the other hand these low field features may appear similar to the reversed MR curves measured on the devices and could be thought as responsible for them.

6.2 Comparison with the device magnetoresistance

As already mentioned, it has been argued that the MR of FM electrodes can show as a MR of the opposite sign in the device. According to Riminucci et al. [189] this artifacts may become relevant when the electrode resistance and

the semiconductor layer resistance are comparable. They modeled the cross bar configuration device with the simple one-dimensional (1D) n loops resistor network shown in figure 6.6. The measured resistance is defined as $R = V/i$, where V and

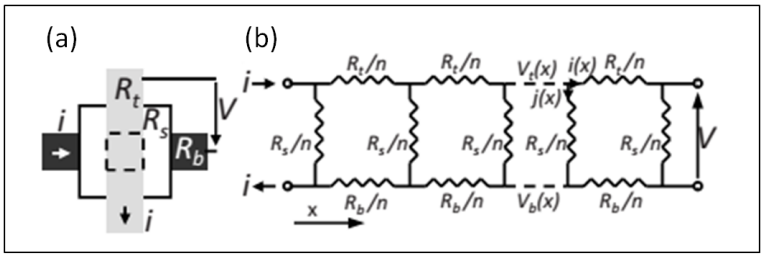

Figure 6.6: (a) Schematic diagram of the cross-bar layout of the device. Rt is the resistance of the top electrode (light gray), Rs is the resistance of the semiconducting layer (white), and Rb is the resistance of the bottom electrode (dark gray). The active area at the intersection of the top and bottom electrodes is outlined by the dashed line. (b) Resistor model of the device. n is the number of loops in the discrete model, i(x) is the current flowing in plane along the electrodes, j(x) is the current per unit length perpendicular to plane across the semiconducting layer, Vt(x) is the voltage drop on the top electrode and Vb(x) is the voltage on the bottom electrode [189].

i are the voltage and the injected current. In order to obtain R as a function of the electrode resistances, the differential equations to be solved are given, for the continuum case, by

$$\begin{cases} \frac{dV_t(x)}{dx} = -\frac{R_t}{L} i(x) \\ \frac{dV_b(x)}{dx} = \frac{R_b}{L} i(x) \\ V_t(x) - V_b = R_s \times L \times j(x) \\ \frac{di(x)}{dx} = -j(x) \end{cases}$$

where L is the width of the electrodes. Using the boundary condition i(0)=i and i(L)=0, the solution for the measured resistance is given by

$$R \equiv \frac{V_t(L) - V_b(L)}{i} = R_s \frac{\sqrt{\frac{R_t+R_b}{R_s}}}{sinh\left(\sqrt{\frac{R_t+R_b}{R_s}}\right)} \tag{6.1}$$

The simulation in figure 6.7b shows the effect that the MR of a FM electrode (figure 6.7a) has on the measured device MR according to Eq. 6.1. In figures 6.7c-d are reported respectively a MR measured on a LSMO thin film in a four points configuration and a typical MR measured on a low resistance ($\sim$ 80 Ω) device at

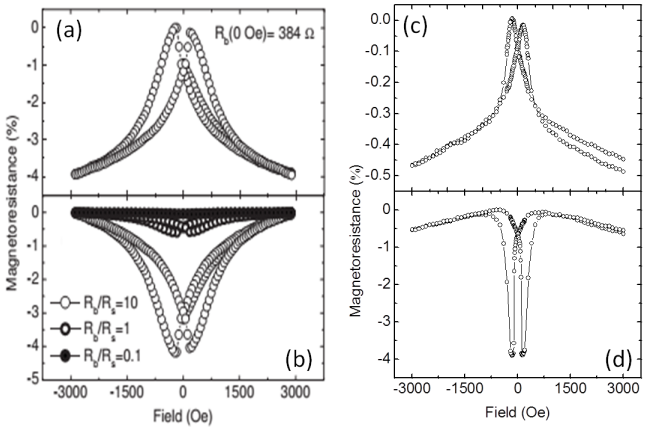

Figure 6.7: (a) MR of a LSMO bottom electrode measured at 20 K. (b) Simulated device MR (according to eq. 6.1) for different ratio R_b/R_s [189]. (c) MR of an LSMO thin film at 100 K. (d) MR of a low resistance device with $R_b/R_s \sim 1$.

100 K. By the comparison between the two R-H characteristics we can rule out that the device MR is an electrode-induced artifact for several reasons:

1. As in the reported example, the LSMO electrode MR is always well below 1 % while the measured device MR can reach values up to 20 %. According to the model presented above, such huge artifacts would be possible only if the ratio between the bottom electrode and the semiconductor resistance were well above $R_b/R_s > 100$, that is not our case. It should be mentioned that high MR signals have been detected also in devices where $R_s > 200k\Omega$ and $R_b < 1k\Omega$.

2. The reverse shape of the electrode MR is not reproduced in the high field region (1500 Oe - 3000 Oe).

3. As illustrated in figure 6.5, the sign of the electrode AMR is reversed by rotating the device in plane of 90°, while the sign of the device MR does not depend on the angle.

4. Finally, the LSMO magnetoresistance has been studied as a function of temperature and a radically different temperature dependence have been observed, respectively, for the AMR signal and the device MR (figure 6.8).

The maximum of the CMR contribution has been extrapolated from the linear behavior of the higher field region. The AMR signal is taken as the difference between the so-obtained CMR maximum and the positive (negative) resistance peak (figure 6.5). The so-isolated AMR signal has been plotted as a function of temperature and compared to the device MR(T) in figure 6.8. While the AMR is almost constant within experimental error (in the range where it is detectable), the device MR typically shows a nearly-quadratic dependence on temperature.

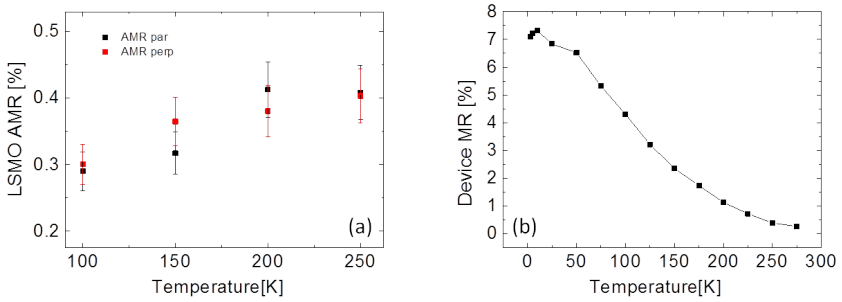

Figure 6.8: Comparison between the temperature dependence of the LSMO AMR signal (a) and a typical MR signal measured on a thin device (b). As argued in the text, two radically different behavior are observed.

Chapter 7

Memristive switching in thin devices

Memristive effects have been studied in our organic spin valves for several years [150, 5, 6]. As already mentioned in paragraph 2.2, electrical switching up to 10^4 cycles were detected, showing a good stability. Moreover an interesting interplay between magnetic and resistive switching was demonstrated. However the physical mechanisms behind these electrical switching are not clear, yet. In this chapter I describe the memristive effects in the framework of the parallel circuit model proposed in paragraph 4.3.2 by analyzing the temperature dependence of the junction resistance before and after the resistive switching. The effects of the latter on the magnetoresistive properties of the devices are also taken into account.

7.1 Resistive switching and parallel circuit model

Thin devices in their pristine state usually show a peculiar R(T) characteristic with a smooth peak in the temperature range from 220 K to 300 K. It has already been shown that this behavior can be described as the superposition of metallic and thermally activated charge transport mechanisms (see the parallel circuit model in paragraph 4.3.2). In figure 7.1a,c,e the R(T) characteristics of three devices in their pristine state are reported. Samples A, B and C are LSMO/Alq3(15 nm)/AlOx/Co spin-valve structure grown on the same substrate. They were cooled down from room temperature to 100 K at a rate of 0.3 K/min while measuring their resistance at a bias voltage of -0.1 V. At 100 K the devices have been set respectively in different resistive states before measuring their R(T) from 100 K to 330 K (figure 7.1b,d,f). The sample A is left in the pristine state as a reference. No

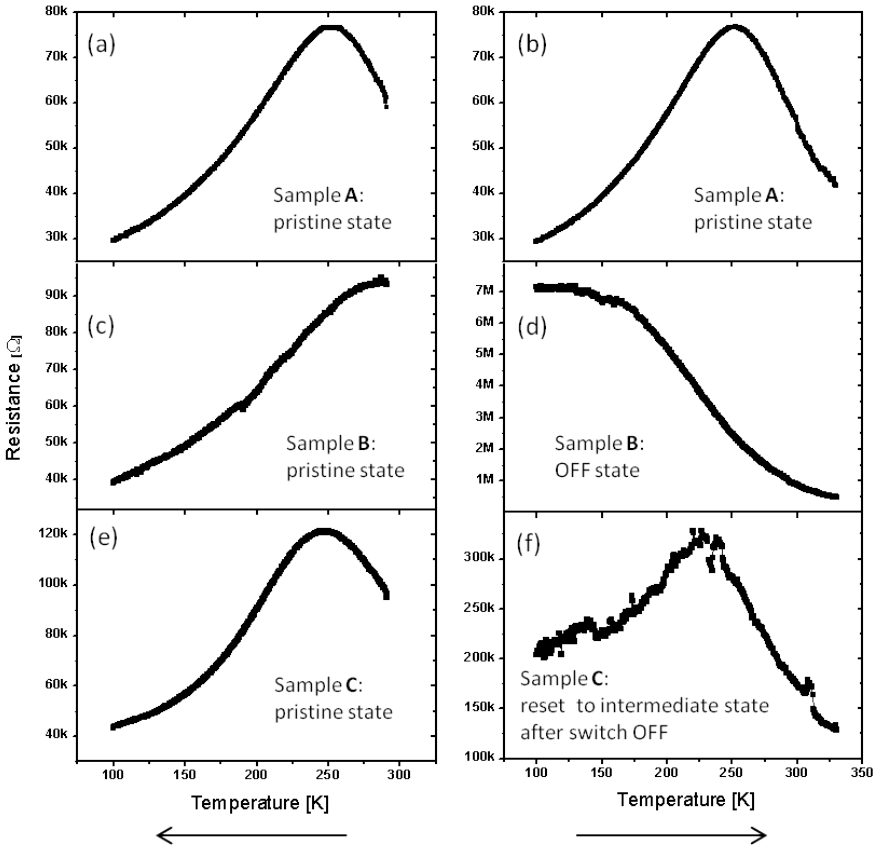

Figure 7.1: (a), (c) and (e) show the R(T) characteristics for three devices in the low resistance pristine state. (b), (d) and (f) show the R(T) of the same devices in different resistive states. In particular (b) sample A is left in the pristine state as a reference, (d) sample B is set in a high resistance state, (f) sample C is set in a high resistance state and then brought back in an intermediate state. The curves have been taken at a rate of 0.3 K/min. The arrows indicate the sweep direction.

differences can be observed between the downward and upward sweeps in this case, showing a good thermal stability in this range of temperature. The sample B was set in a high resistance state by applying a negative bias voltage to the LSMO electrode up to -2 V. The step-by-step voltage sweep employed is shown in figure 7.2. After this switch-OFF procedure the resistance at 100 K is two

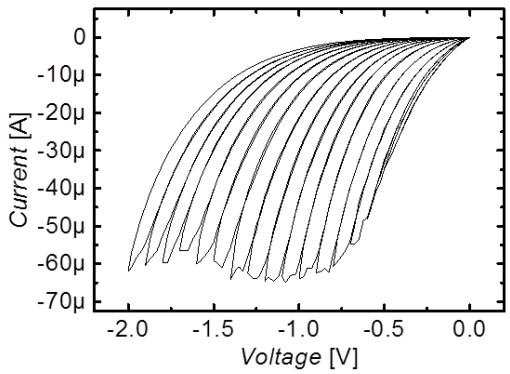

Figure 7.2: Voltage sweep employed to set the device B in a high resistance state. Consecutive I-V characteristics are measured from 0 to -V_{max} with a voltage step of 5 mV, by increasing progressively V_{max} by 100 mV at each I-V curve up to -2 V.

orders of magnitude higher than the virgin state resistance, and the R(T) results dramatically modified (figure 7.1d). Indeed, no metallic behavior (dR/dT>0) can be observed in the entire temperature range. Now, at low temperature, the resistance shows an almost linear behavior, with a negative derivative dR/dT, and a nearly exponential decrease from about 220 K to 330 K, suggesting a hopping mechanism to take place. Based on these observations, I used again the parallel circuit model (paragraph 4.3.2), this time considering a hopping channel (NNH model) in parallel to a tunnel (linear) channel. The fitting equation is then given by

$$R(T) = \left(\frac{1}{R_t} + \frac{1}{R_{NNH}} \right)^{-1}, \tag{7.1}$$

where

$$R_t = R_{to} + \alpha_t T \tag{7.2}$$

and

$$R_{NNH} = R_o exp(T_o/T). \tag{7.3}$$

The equation 7.1, as shown in figure 7.3, perfectly describes the measured R(T) characteristic. I obtained $R_{to} = 7.9\ M\Omega$ and $\alpha_t = -6.84\ k\Omega\ K^{-1}$, which give a ratio $R_t(0K)/R_t(300K) \sim 1.35$, compatible with a tunnel through an insulating barrier [105]. The tunnel regime is further confirmed by the I-V characteristics, which can be well described by the multi-step tunneling GM model (see

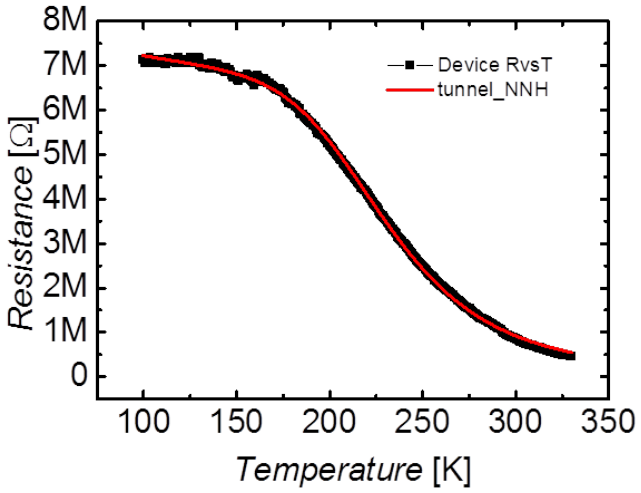

Figure 7.3: Resistance as a function of temperature measured on the sample B in its OFF state. The fit obtained from equation 7.1 is shown (red line).

paragraph 4.3.1). The activation energy obtained for the hopping mechanism is $\Delta E_{NNH} = (167 \pm 10) meV$, corresponding to that found in the pristine state within the error. This indicates that the conduction properties of the NNH channels have not been modified. On the other hand R_o results increased by a factor $\sim$ 15, which can be interpreted as a reduction of the effective area corresponding to this channel.

The sample C was set in a high resistance state comparable to the OFF state of the sample B by means of the same step-by-step switch-OFF procedure (figure 7.4a). Then a low resistance state was restored by means of a positive voltage sweep (figure 7.4b), demonstrating the reversibility of the switching process. After this RESET-process the sample was heated up to 330 K while measuring its resistance at -0.1 V. As can be observed in figure 7.1f, the R(T) characteristic shows a positive derivative dR/dT up to 230 K, indicating that the metallic behavior has been recovered. It can be noticed that the new low-resistance state is not exactly equivalent to the pristine state: the absolute value of the resistance is increased and the peak is shifted towards lower temperatures. Indeed, the devices can be set in many intermediate resistive states, as demonstrated by the voltage sweep in the figures 7.2 and 7.4.

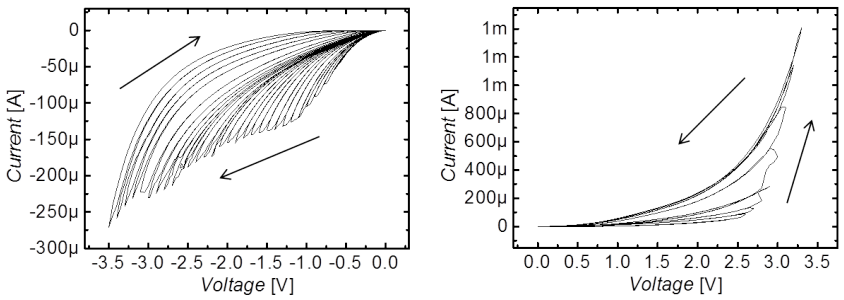

Figure 7.4: Voltage sweeps employed to (a) set the device C in a high resistance state and (b) restore a low resistance state. The procedure has already been described in figure 7.2.

In the framework of the parallel circuit model, it means that, during a switching process, metallic-like channels are turned into localized tunnel junctions and vice versa. On the other hand we found an apparent reduction of the effective area relative to the NNH channel. Even if this aspect needs to be better understood, we have reason to believe that switching events take place mainly where shortenings in the organic layer are provided by localized defects, (TEM image in figure 7.5), allowing the LSMO to directly contact the AlOx/Co top layer. Indeed a comparative study we carried out on a LSMO/AlOx/Co MTJ (whose MR is shown in figure 4.18a) showed comparable memristive effects, as shown in figure 7.6.

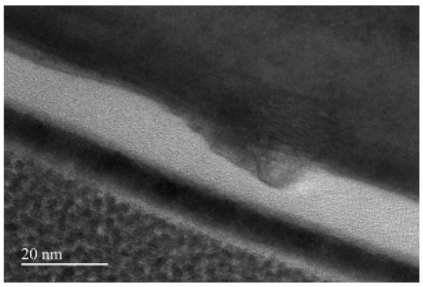

Figure 7.5: TEM cross section of a device with a 15 nm thick Alq3 layer. A defect of the bottom electrode is shown, producing a shortening in the organic barrier. The image has been taken by K. O'Shea at the University of Glasgow.

Many other groups demonstrated that a reversible breakdown can be induced in an

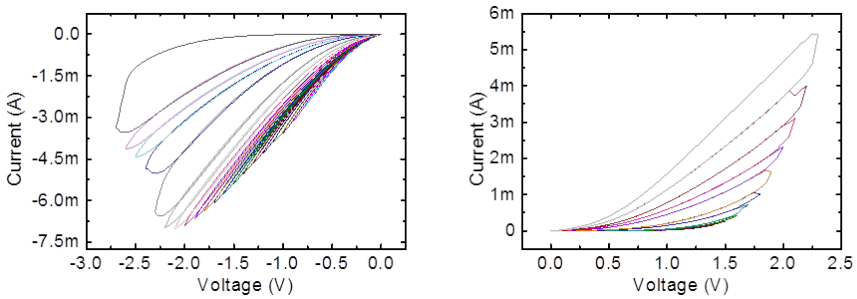

Figure 7.6: Voltage sweeps setting a LSMO/AlOx(5nm)/Co magneto-tunnel junction in a high-resistance OFF state (a) and restoring the low-resistance ON state (b). The memristive behavior is comparable to that measured on the organic LSMO/Alq3/AlOx/Co spin valve shown in figure 7.2 and 7.4.

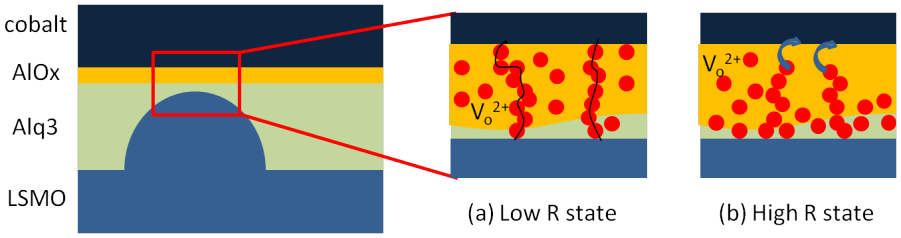

Figure 7.7: Schematic representation of a shortened region in the organic barrier. (a) In the low resistance state percolation paths of oxygen vacancies makes possible metallic conduction (continuous line) through the disordered barrier. (b) By applying a negative bias to the LSMO electrode, oxygen vacancies are moved away from the top electrode and the percolation paths are interrupted. In this configuration charge transport can only take place through a tunneling mechanism (blue arrows).

amorphous AlOx barrier by applying a bias [191, 192, 193], even if the underlying mechanism is still debated. I qualitatively describe the device as a parallel of memristive metal/AlOx/metal junctions, by assuming that electrical switching proceeds by means of the drift of positively charged oxygen vacancies acting as dopants to form (turn ON) or disperse (turn OFF) locally conductive channels through the electronic barrier [4, 194, 195], as schematically illustrated in figure 7.7.
Other switching mechanisms have been proposed in the literature for organic devices: charge trapping in the organic bulk [196] and charge trapping and/or dipole reorganization at one interface inducing variations in the injection barrier [197].

The former can be ruled out because of the long data retention times, as already argued by Cölle et al [198]. Indeed, some of our devices have been measured several times over a period of months, sweeping the temperature from room temperature to 100 K and vice versa, and the resistive state was retained between consecutive measurements. Studies with techniques such as thermally stimulated current show that these trapped charges are released at temperatures below room temperature with applied voltages below 1 V and even at zero bias [199]. Therefore bulk charge trapping cannot explain the long retention times. The latter can be ruled out by analyzing the impedance spectra of a device in different resistive states. The Cole-Cole plot in the two states (figure 7.8) can be described as a series of a resistance representing the two electrodes (measured in a two point configuration), and a parallel RC circuit. The formation of an interface layer should be accompanied by a change in the device capacitance. However identical values for the capacitance were found in different resistive states, indicating that the memory effect is due to resistive switching.

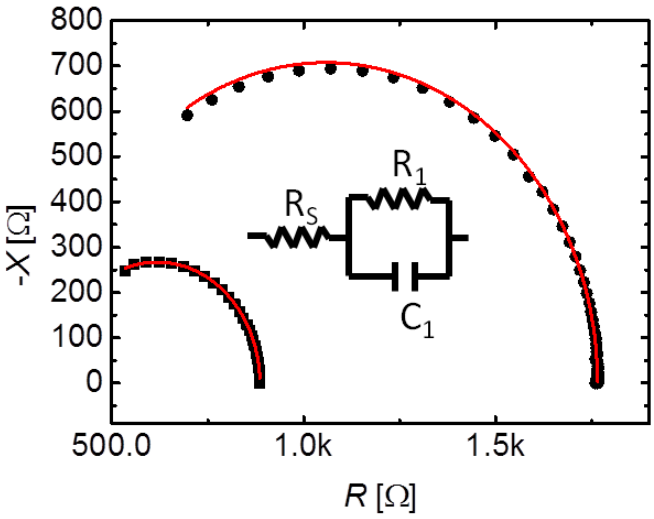

Figure 7.8: Cole-Cole plot taken in the pristine state (black squares) and in a higher resistive state (black circles). Modeling the device with the equivalent circuit represented in the figure, the fits (red lines) gives the same values for the capacitance in the two states, C_1=100pF, compatible with the geometrical capacitance. This shows that the memory effect is due to resistive switching.

7.2 Resistive switching and magnetoresistance

As already mentioned in paragraph 2.2, the interesting interplay between memristive switching and magnetoresistance in our devices has been carefully studied in the last years [5, 6]. Here this interplay is analyzed in the framework of the parallel circuit model, by studying the MR of the sample C before and after the switching process (figure 7.9). The low-resistance pristine state shows a clear SV signal at 100 K, in this case >11%. This signal can be progressively reduced by means of the negative voltage sweep already described above. In the high resistive state shown in figure 7.9c it can not be detected. Finally the SV signal can be restored by applying a positive voltage sweep, as shown in figure 7.9e. Thus it has been demonstrated that MR can be turned ON and OFF by means of electrical switching, which are described in the paragraph 7.1 as the formation and dispersion of metallic-like channels across the junction. This analysis further indicates that SV signals and metallic filaments are strictly related. As already stated in paragraph 4.3.3, however, it was shown [177] that conductive BMR and TMR can not be experimentally distinguished by means of magnetoresistive measurement. Moreover, even when the metallic behavior prevails in the R(T) curve, it does not exclude tunnel injection in correspondence to some defects. Therefore both BMR and TMR should be considered as a possible mechanism to explain the SV signals. On the other hand, the absence of a SV signal in the OFF state can be explained by considering that now the number of the conductive channels, responsible for the magnetoresistive effects, has been strongly reduced, as demonstrated by the R_{OFF} temperature dependence in figure 7.3. Even if the low temperature behavior indicates that tunnel channel are still present, the field-induced resistance variations are too small to be detected as a relative variation of the total resistance.

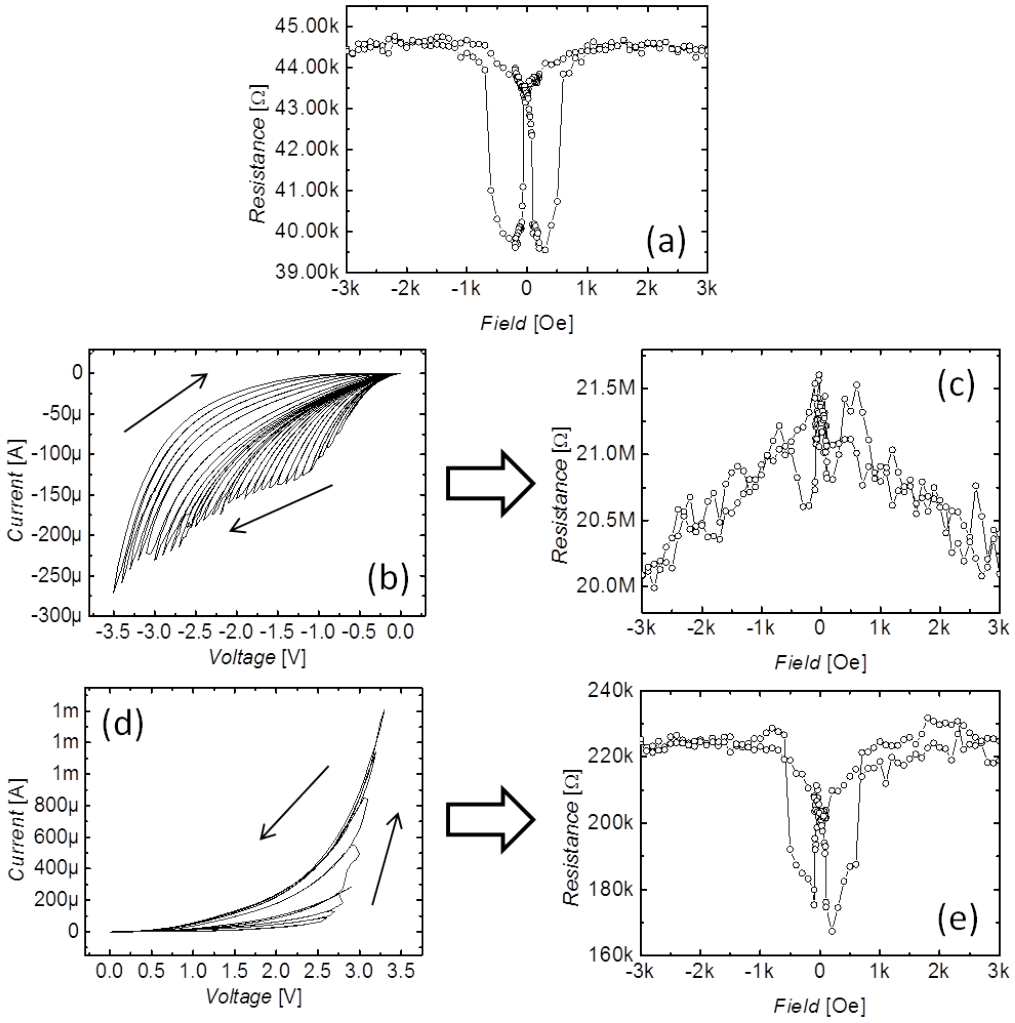

Figure 7.9: Study of the MR of sample C as a function of the resistive state. (a) MR in the pristine state. (b) Switch-OFF voltage sweep setting the sample in a high resistance state. (c) MR in the so-obtained high resistance state. (d) RESET voltage sweep bringing back the sample to a lower resistance state. (e) MR in the recovered low resistance state. All the MR have been measured at -0.1 V and 100 K.

Conclusions

I studied charge and spin transport in $La_{0.7}Sr_{0.3}MnO_3$/Alq3/AlOx/Co organic spin valves, showing an interesting interplay between magnetoresistive effects and memristive switching. I-V and R-H characteristics have been analyzed as a function of the organic-spacer-layer thickness (10 nm-300 nm) and temperature (100 K-330 K). This preliminary study showed that the samples can be grouped into two clearly distinguishable conduction regimes. By fixing a thickness threshold approximately around 25 nm, I divided them into thin and thick devices as shown in table 7.1, where the main differences between the two regimes are listed.

thin devices	**thick devices**
injection at low voltages (∼mV) (R ∼ 100 Ω-100 $k\Omega$)	no injection below a threshold voltage up to several V (R∼GΩ)
near-parabolic differential conductance	highly non-linear I-V characteristics above the voltage threshold
metallic temperature dependence of the resistance up to room temperature	thermally activated conduction
SV signal detected in the voltage range - 0.5 V-0.5 V	no SV signal detected up to 8 V
reversible resistive switching (up to $R_{OFF}/R_{ON} > 10^2$)	no memristive effects observed

Table 7.1: Differences between the two conduction regimes individuated respectively for thin (<25 nm) and thick devices.

The I-V characteristic of thin devices can be described by a multi-step tunneling through a disordered Alq3/AlOx barrier, indicating the presence of shortenings across the organic bulk. On the other hand, the behavior of thick devices is compatible with models for charge transport in organic materials, however it was not

possible to establish if the current is space charge limited or injection limited due to the high dispersion of the data as a function of thickness. The correspondence between magnetoresistive effects and the former conductive regime is confirmed by a comparison with the literature about Alq3-based spin valves, even if a semiconductive temperature dependence has been found in some works.
Then I took into account the presence of metallic paths across the junction to explain the positive sign of the derivative dR/dT up to room temperature, showing that thin devices can be modeled by an equivalent circuit where a metallic channel described by the Bloch-Grüneisen formula and a nearest neighbor hopping (NNH) channel act in parallel. In the framework of this model, a coherent description for the interplay between MR and memristive switching can be given. Indeed, I showed that during a switching process, metallic-like channels are turned into localized tunnel junctions and vice versa. On the other hand, the conductive properties of organic bulk of the device, which I assume to be described by the NNH channel, are not affected. The SV signal observed in the ON state can be progressively reduced by switching the device in the OFF state, proofing that metallic pinholes and MR effects are related. As a consequence SV signals can be explained as tunnel magnetoresistance (TMR) or ballistic magnetoresistance (BMR) occurring across shortened regions of the organic bulk. This explanation is compatible with the absence of Hanle effect, also demonstrated in this work.
To conclude, this work demonstrates that SV signals can be explained without resorting to spin injection and transport into the organic layer. However it does not exclude that organic molecules can play an active role at the metal/organic interface. Indeed, the effects of the organic-induced hybridization on the electrode polarization are still an open question. Moreover, recent works from the literature pointed out that MR signals can be detected for pure spin current, overcoming the problem of short circuits.

Bibliography

[1] V. Dediu, M. Murgia, F.C. Matacotta, C. Taliani, and S. Barbanera. Room temperature spin polarized injection in organic semiconductor. *Solid State Communications*, 122(3 - 4):181 – 184, 2002.

[2] Z.H. Xiong, D. Wu, Z. V. Vardeny, and J. Shi. Giant magnetoresistance in organic spin-valves. *Nature*, 427(6977):821–824, 2004.

[3] L.O. Chua. Memristor-the missing circuit element. *Circuit Theory, IEEE Transactions on*, 18(5):507–519, 1971.

[4] D.B. Strukov, G.S. Snider, D.R. Stewart, and R.S. Williams. The missing memristor found. *nature*, 453(7191):80–83, 2008.

[5] M. Prezioso, A. Riminucci, I. Bergenti, P. Graziosi, D. Brunel, and V.A. Dediu. Electrically programmable magnetoresistance in multifunctional organic-based spin valve devices. *Advanced Materials*, 23(11):1371–1375, 2011.

[6] M. Prezioso, A. Riminucci, P. Graziosi, I. Bergenti, R. Rakshit, R. Cecchini, A. Vianelli, F. Borgatti, N. Haag, M. Willis, A.J. Drew, W.P. Gillin, and V.A. Dediu. A single-device universal logic gate based on a magnetically enhanced memristor. *Advanced Materials*, 25(4):534–538, 2013.

[7] M. Cinchetti, K. Heimer, J.P. Wüstenberg, O. Andreyev, M. Bauer, S. Lach, C. Ziegler, Y. Gao, and M. Aeschlimann. Determination of spin injection and transport in a ferromagnet/organic semiconductor heterojunction by two-photon photoemission. *Nature materials*, 8(2):115–119, 2009.

[8] A.J. Drew, J. Hoppler, L. Schulz, F.L. Pratt, P. Desai, P. Shakya, T. Kreouzis, W.P. Gillin, A. Suter, N.A. Morley, et al. Direct measurement of the

electronic spin diffusion length in a fully functional organic spin valve by low-energy muon spin rotation. *Nature materials*, 8(2):109–114, 2009.

[9] A. Riminucci, M. Prezioso, C. Pernechele, P. Graziosi, I. Bergenti, R. Cecchini, M. Calbucci, M. Solzi, and A.V. Dediu. Hanle effect missing in a prototypical organic spintronic device. *Applied Physics Letters*, 102(9):092407, 2013.

[10] W.Brutting. *Physics of Organic Semiconductors*. WILEY-VCH, Weinheim, 2005.

[11] S. R. Forrest. The path to ubiquitous and low-cost organic electronic appliances on plastic. *Nature*, 428(6986):911–918, 2004.

[12] H. Bässler and A. Köhler. Charge transport in organic semiconductors. In *Unimolecular and Supramolecular Electronics I*, pages 1–65. Springer, 2012.

[13] V. Coropceanu, J. Cornil, D. A. da Silva Filho, Y. Olivier, R. Silbey, and J.L. Brédas. Charge transport in organic semiconductors. *Chemical reviews*, 107(4):926–952, 2007.

[14] H. Bässler. Charge transport in disordered organic photoconductors. *phys. status solidi b*, 175(1):15–56, 1993.

[15] N. Tessler, Y. Preezant, N. Rappaport, and Y. Roichman. Charge transport in disordered organic materials and its relevance to thin-film devices: A tutorial review. *Advanced Materials*, 21(27):2741–2761, 2009.

[16] A. Miller and E. Abrahams. Impurity conduction at low concentrations. *Phys. Rev.*, 120:745–755, Nov 1960.

[17] S.V. Novikov, D.H. Dunlap, V.M. Kenkre, P.E. Parris, and A.V. Vannikov. Essential role of correlations in governing charge transport in disordered organic materials. *Physical Review Letters*, 81(20):4472, 1998.

[18] C. Tanase, P.W.M. Blom, D.M. De Leeuw, and E.J. Meijer. Charge carrier density dependence of the hole mobility in poly (p-phenylene vinylene). *physica status solidi (a)*, 201(6):1236–1245, 2004.

[19] V. I. Arkhipov, P. Heremans, E. V. Emelianova, G. J. Adriaenssens, and H. Bässler. Weak-field carrier hopping in disordered organic semiconductors: the effects of deep traps and partly filled density-of-states distribution. *Journal of Physics: Condensed Matter*, 14(42):9899, 2002.

[20] W. F. Pasveer, J. Cottaar, C. Tanase, R. Coehoorn, P. A. Bobbert, P. W. M. Blom, D. M. de Leeuw, and M. A. J. Michels. Unified description of charge-carrier mobilities in disordered semiconducting polymers. *Phys. Rev. Lett.*, 94:206601, May 2005.

[21] R. Coehoorn, W. F. Pasveer, P. A. Bobbert, and M. A. J. Michels. Charge-carrier concentration dependence of the hopping mobility in organic materials with gaussian disorder. *Phys. Rev. B*, 72:155206, Oct 2005.

[22] I. I. Fishchuk, V. I. Arkhipov, A. Kadashchuk, P. Heremans, and H. Bässler. Analytic model of hopping mobility at large charge carrier concentrations in disordered organic semiconductors: Polarons versus bare charge carriers. *Phys. Rev. B*, 76:045210, Jul 2007.

[23] A. Rose. Space-charge-limited currents in solids. *Phys. Rev.*, 97:1538–1544, Mar 1955.

[24] P.Mark M.A.Lampert. *Current injection in solids.* Academic Press, New York, 1970.

[25] P.N. Murgatroyd. Theory of space-charge-limited current enhanced by Frenkel effect. *Journal of Physics D: Applied Physics*, 3(2):151, 1970.

[26] P. E. Burrows, Z. Shen, V. Bulovic, D. M. McCarty, S. R. Forrest, J. A. Cronin, and M. E. Thompson. Relationship between electroluminescence and current transport in organic heterojunction light emitting devices. *Journal of Applied Physics*, 79(10), 1996.

[27] Kwok K. Ng S.M. Sze. *Physics of Semiconductor Devices.* WILEY-INTERSCIENCE, Hoboken, New Jersey, 2007.

[28] S. Barth, U. Wolf, H. Bässler, P. Müller, H. Riel, H. Vestweber, P.F. Seidler, and W. Riess. Current injection from a metal to a disordered hopping system.

iii. comparison between experiment and monte carlo simulation. *Physical Review B*, 60(12):8791, 1999.

[29] U. Wolf, V.I. Arkhipov, and H. Bässler. Current injection from a metal to a disordered hopping system. i. monte carlo simulation. *Physical Review B*, 59(11):7507, 1999.

[30] Y.N. Gartstein and E.M. Conwell. High-field hopping mobility in molecular systems with spatially correlated energetic disorder. *Chemical physics letters*, 245(4):351–358, 1995.

[31] A.L. Burin and M.A. Ratner. Temperature and field dependence of the charge injection from metal electrodes into random organic media. *The Journal of Chemical Physics*, 113(10):3941–3944, 2000.

[32] M. Baldo and S. Forrest. Interface-limited injection in amorphous organic semiconductors. *Phys. Rev. B*, 64:085201, Aug 2001.

[33] J.J.M. Van Der Holst, M.A. Uijttewaal, B. Ramachandhran, R. Coehoorn, P.A. Bobbert, G.A. De Wijs, and R.A. De Groot. Modeling and analysis of the three-dimensional current density in sandwich-type single-carrier devices of disordered organic semiconductors. *Physical Review B*, 79(8):085203, 2009.

[34] W. Brütting, S. Berleb, and A.G. Mückl. Space-charge limited conduction with a field and temperature dependent mobility in Alq light-emitting devices. *Synthetic Metals*, 122(1):99 – 104, 2001. Proceedings of the E-MRS 2000 Spring Meeting, Symposium I.

[35] H. Ishii, K. Sugiyama, E. Ito, and K. Seki. Energy level alignment and interfacial electronic structures at organic/metal and organic/organic interfaces. *Advanced Materials*, 11(8):605–625, 1999.

[36] S. Braun, W. R. Salaneck, and M. Fahlman. Energy-level alignment at organic/metal and organic/organic interfaces. *Advanced Materials*, 21(14-15):1450–1472, 2009.

[37] A. Riminucci, I. Bergenti, L.E. Hueso, M. Murgia, C. Taliani, Y. Zhan, F. Casoli, M.P. de Jong, and V. Dediu. Negative spin valve effects in manganite/organic based devices. *arXiv preprint cond-mat/0701603*, 2007.

[38] X. Crispin, V. Geskin, A. Crispin, J. Cornil, R. Lazzaroni, W. R. Salaneck, and J.L. Bredas. Characterization of the interface dipole at organic/metal interfaces. *Journal of the American Chemical Society*, 124(27):8131–8141, 2002.

[39] J. Hwang, A. Wan, and A. Kahn. Energetics of metal–organic interfaces: new experiments and assessment of the field. *Materials Science and Engineering: R: Reports*, 64(1):1–31, 2009.

[40] Y.Q. Zhan, M.P. De Jong, F.H. Li, V. Dediu, M. Fahlman, and W.R. Salaneck. Energy level alignment and chemical interaction at Alq 3/Co interfaces for organic spintronic devices. *Physical Review B*, 78(4):045208, 2008.

[41] Y. Zhan and M. Fahlman. The study of organic semiconductor/ferromagnet interfaces in organic spintronics: A short review of recent progress. *Journal of Polymer Science Part B: Polymer Physics*, 50(21):1453–1462, 2012.

[42] I.G. Hill, A. Kahn, Z.G. Soos, and R.A. Pascal Jr. Charge-separation energy in films of π-conjugated organic molecules. *Chemical Physics Letters*, 327(3):181–188, 2000.

[43] I.G. Hill, A. Kahn, Z.G. Soos, and R.A. Pascal Jr. Charge-separation energy in films of π-conjugated organic molecules. *Chemical Physics Letters*, 327(3):181–188, 2000.

[44] Y.Q. Zhan, I. Bergenti, L.E. Hueso, V. Dediu, M.P. de Jong, and Z.S. Li. Alignment of energy levels at the Alq3/$La_{0.7}Sr_{0.3}MnO_3$ interface for organic spintronic devices. *Physical Review B*, 76(4):045406, 2007.

[45] V.A. Dediu, L.E. Hueso, I. Bergenti, and C. Taliani. Spin routes in organic semiconductors. *Nature materials*, 8(9):707–716, 2009.

[46] Y. Zhan, E. Holmström, R. Lizárraga, O. Eriksson, X. Liu, F. Li, E. Carlegrim, S. Stafström, and M. Fahlman. Efficient spin injection through exchange coupling at organic semiconductor/ferromagnet heterojunctions. *Advanced Materials*, 22(14):1626–1630, 2010.

[47] S. Lach, A. Altenhof, K. Tarafder, F. Schmitt, M. Ali, M. Vogel, J. Sauther, P. M Oppeneer, C. Ziegler, et al. Metal-organic hybrid interface states of

a ferromagnet/organic semiconductor hybrid junction as basis for engineering spin injection in organic spintronics. *Advanced Functional Materials*, 22(5):989–997, 2012.

[48] W. Thomson. *Proc. R. Soc.*, 8:546, 1857.

[49] P. M. Tedrow and R. Meservey. Spin polarization of electrons tunneling from films of fe, co, ni, and gd. *Phys. Rev. B*, 7:318–326, Jan 1973.

[50] M. Julliere. Tunneling between ferromagnetic films. *Physics Letters A*, 54(3):225 – 226, 1975.

[51] M. N. Baibich, J. M. Broto, A. Fert, F. Nguyen Van Dau, F. Petroff, P. Etienne, G. Creuzet, A. Friederich, and J. Chazelas. Giant magnetoresistance of (001)Fe/(001)Cr magnetic superlattices. *Phys. Rev. Lett.*, 61:2472–2475, Nov 1988.

[52] G. Binasch, P. Grünberg, F. Saurenbach, and W. Zinn. Enhanced magnetoresistance in layered magnetic structures with antiferromagnetic interlayer exchange. *Phys. Rev. B*, 39:4828–4830, Mar 1989.

[53] X. Lou, C. Adelmann, S.A. Crooker, E.S. Garlid, J. Zhang, K.S. M. Reddy, S.D. Flexner, C.J. Palmstrøm, and P.A. Crowell. Electrical detection of spin transport in lateral ferromagnet–semiconductor devices. *Nature Physics*, 3(3):197–202, 2007.

[54] G. Schmidt, D. Ferrand, L.W. Molenkamp, A.T. Filip, and B.J. Van Wees. Fundamental obstacle for electrical spin injection from a ferromagnetic metal into a diffusive semiconductor. *Physical Review B*, 62(8):R4790, 2000.

[55] J. S. Moodera, L. R Kinder, T.M. Wong, and R. Meservey. Large magnetoresistance at room temperature in ferromagnetic thin film tunnel junctions. *Physical Review Letters*, 74(16):3273, 1995.

[56] S.S.P. Parkin, C. Kaiser, A. Panchula, P.M. Rice, B. Hughes, M. Samant, and S.H. Yang. Giant tunnelling magnetoresistance at room temperature with MgO(100) tunnel barriers. *Nature materials*, 3(12):862–867, 2004.

[57] S. Yuasa, T. Nagahama, A. Fukushima, Y. Suzuki, and K. Ando. Giant room-temperature magnetoresistance in single-crystal fe/mgo/fe magnetic tunnel junctions. *Nature materials*, 3(12):868–871, 2004.

[58] W.H. Butler, X.G. Zhang, T.C. Schulthess, and J.M. MacLaren. Spin-dependent tunneling conductance of Fe/ MgO/Fe sandwiches. *Physical Review B*, 63(5):054416, 2001.

[59] J. Mathon and A. Umerski. Theory of tunneling magnetoresistance of an epitaxial Fe/ MgO/Fe(001) junction. *Phys. Rev. B*, 63:220403, May 2001.

[60] J.F. Gregg, I. Petej, E. Jouguelet, and C. Dennis. Spin electronics - a review. *Journal of Physics D: Applied Physics*, 35(18):R121, 2002.

[61] N.F. Mott. The electrical conductivity of transition metals. 153(880):699–717, 1936.

[62] W.J.M. Naber, S. Faez, and W.G. van der Wiel. Organic spintronics. *Journal of Physics D: Applied Physics*, 40(12):R205, 2007.

[63] M. Johnson and R.H. Silsbee. Interfacial charge-spin coupling: Injection and detection of spin magnetization in metals. *Phys. Rev. Lett.*, 55:1790–1793, Oct 1985.

[64] T. Valet and A. Fert. Theory of the perpendicular magnetoresistance in magnetic multilayers. *Phys. Rev. B*, 48:7099–7113, Sep 1993.

[65] Albert Fert et al. The origin, development and future of spintronics. *Nobel lecture*, 2007.

[66] A. Fert and H. Jaffrès. Conditions for efficient spin injection from a ferromagnetic metal into a semiconductor. *Phys. Rev. B*, 64:184420, Oct 2001.

[67] E.I. Rashba. Theory of electrical spin injection: Tunnel contacts as a solution of the conductivity mismatch problem. *Phys. Rev. B*, 62:R16267–R16270, Dec 2000.

[68] A. Fert, J.M. George, H. Jaffres, and R. Mattana. Semiconductors between spin-polarized sources and drains. *Electron Devices, IEEE Transactions on*, 54(5):921–932, 2007.

[69] A. Fert and S.F. Lee. Theory of the bipolar spin switch. *Phys. Rev. B*, 53:6554–6565, Mar 1996.

[70] A. Fert and H. Jaffrès. Conditions for efficient spin injection from a ferromagnetic metal into a semiconductor. *Phys. Rev. B*, 64:184420, Oct 2001.

[71] I. Žutić, J. Fabian, and S. Das Sarma. Spintronics: Fundamentals and applications. *Rev. Mod. Phys.*, 76:323–410, Apr 2004.

[72] Spin coherence in semiconductors: storage, transport and reduced dimensionality. *Physica E: Low-dimensional Systems and Nanostructures*, 9(1):194 – 201, 2001. Proceedings of the Eleventh International Winterschool on New Developments in Solid State Physics,.

[73] R.J. Elliott. Theory of the effect of spin-orbit coupling on magnetic resonance in some semiconductors. *Phys. Rev.*, 96:266–279, Oct 1954.

[74] N.W. Ashcroft and N.D. Mermin. *Solid State Physics*. Saunders College, Philadelphia, 1976.

[75] M.I. D'Yakonov and V.I. Perel'. Spin Orientation of Electrons Associated with the Interband Absorption of Light in Semiconductors. *Soviet Journal of Experimental and Theoretical Physics*, 33:1053, 1971.

[76] A.G. Aronov, G.E. Pikus, and A.N. Titkov. Spin relaxation of conduction electrons in p-type ill-v compounds. *Sov. Phys. JETP*, 57:680, 1983.

[77] M.I. Dyakonov and V.I. Perel. Hyperfine interaction in optical orientation of electrons in semiconductors. *Soviet Journal of Experimental and Theoretical Physics*, 36:995, 1973.

[78] I.A. Merkulov, A.L. Efros, and M. Rosen. Electron spin relaxation by nuclei in semiconductor quantum dots. *Phys. Rev. B*, 65:205309, Apr 2002.

[79] G. Szulczewski, S. Sanvito, and M. Coey. A spin of their own. *Nature materials*, 8(9):693–695, 2009.

[80] A.R. Rocha, V.M. Garcia-Suarez, S.W. Bailey, C.J. Lambert, J. Ferrer, and S. Sanvito. Towards molecular spintronics. *Nature materials*, 4(4):335–339, 2005.

[81] S. Sanvito and A. R. Rocha. Molecular-spintronics: the art of driving spin through molecules. *Journal of Computational and Theoretical Nanoscience*, 3(5):624–642, 2006.

[82] Z.G. Yu. Spin-orbit coupling and its effects in organic solids. *Physical Review B*, 85(11):115201, 2012.

[83] V.I. Krinichnyi. 2-mm waveband electron paramagnetic resonance spectroscopy of conducting polymers. *Synthetic Metals*, 108(3):173 – 222, 2000.

[84] F. J. Jedema, A.T. Filip, and B.J. Van Wees. Electrical spin injection and accumulation at room temperature in an all-metal mesoscopic spin valve. *Nature*, 410(6826):345–348, 2001.

[85] P. A. Bobbert, W. Wagemans, F. W. A. van Oost, B. Koopmans, and M. Wohlgenannt. Theory for spin diffusion in disordered organic semiconductors. *Phys. Rev. Lett.*, 102:156604, Apr 2009.

[86] S. Pramanik, C.G. Stefanita, S. Patibandla, S. Bandyopadhyay, K. Garre, N. Harth, and M. Cahay. Observation of extremely long spin relaxation times in an organic nanowire spin valve. *Nature Nanotechnology*, 2(4):216–219, 2007.

[87] G.A. Prinz. Magnetoelectronics. *Science*, 282(5394):1660–1663, 1998.

[88] W.E. Pickett and D.J. Singh. Electronic structure and half-metallic transport in the $La_{1-x}Sr_xMno_3$ system. *Physical Review B*, 53(3):1146, 1996.

[89] J.Y.T. Wei, N.C. Yeh, and R.P. Vasquez. Tunneling evidence of half-metallic ferromagnetism in $La_{0.7}Ca_{0.3}MnO_3$. *Physical review letters*, 79(25):5150, 1997.

[90] J.H. Park, E. Vescovo, H.J. Kim, C. Kwon, R. Ramesh, and T. Venkatesan. Magnetic properties at surface boundary of a half-metallic ferromagnet $La_{0.7}Sr_{0.3}MnO_3$. *Physical review letters*, 81(9):1953, 1998.

[91] Origin of high transport spin polarization in $La_{0.7}Sr_{0.3}MnO_3$.

[92] G.H. Jonker and J.H. Van Santen. Ferromagnetic compounds of manganese with perovskite structure. *Physica*, 16(3):337 – 349, 1950.

[93] H. Fujishiro, T. Fukase, and M. Ikebe. Charge ordering and sound velocity anomaly in lsmo). *Journal of the Physical Society of Japan*, 67(8):2582–2585, 1998.

[94] C. Zener. Interaction between the *d*-shells in the transition metals. ii. ferromagnetic compounds of manganese with perovskite structure. *Phys. Rev.*, 82:403–405, May 1951.

[95] T. Yoshinori. *Colossal magneto-resistive oxides*. Gordon and Breach Science, Amsterdam, Netherlands, 2000.

[96] G Jeffrey Snyder, Ron Hiskes, Steve DiCarolis, MR Beasley, and TH Geballe. Intrinsic electrical transport and magnetic properties of $La_{0.7}Ca_{0.3}MnO_3$ and $La_{0.7}Sr_{0.3}MnO_3$ mocvd thin films and bulk material. *Physical Review B*, 53(21):14434, 1996.

[97] A.J. Millis, P.B. Littlewood, and B.I. Shraiman. Double exchange alone does not explain the resistivity of $La_{1-x}Sr_xMnO_3$. *Phys. Rev. Lett.*, 74:5144–5147, Jun 1995.

[98] S.Blundell. *Magnetism in Condensed Matter*. Oxford University Press Inc., New York, 2001.

[99] X.W. Li, A. Gupta, G. Xiao, and G.Q. Gong. Low-field magnetoresistive properties of polycrystalline and epitaxial perovskite manganite films. *Applied Physics Letters*, 71(8), 1997.

[100] H.Y. Hwang, S.W. Cheong, N.P. Ong, and B. Batlogg. Spin-polarized intergrain tunneling in $La_{2/3}Sr_{1/3}MnO_3$. *Phys. Rev. Lett.*, 77:2041–2044, Sep 1996.

[101] J. O'Donnell, M. Onellion, M.S. Rzchowski, J.N. Eckstein, and I. Bozovic. Low-field magnetoresistance in tetragonal $La_{1-x}Ca_xMnO_3$ films. *Phys. Rev. B*, 55:5873–5879, Mar 1997.

[102] J.N. Eckstein, I. Bozovic, J. O'Donnell, M. Onellion, and M.S. Rzchowski. Anisotropic magnetoresistance in tetragonal $La_{1-x}Ca_xMnO_\delta$ thin films. *Applied physics letters*, 69(9):1312–1314, 1996.

[103] J.B. Yau, X. Hong, A. Posadas, C.H. Ahn, W. Gao, E. Altman, Y. Bason, L. Klein, M. Sidorov, and Z. Krivokapic. Anisotropic magnetoresistance in colossal magnetoresistive $La_{1-x}Sr_xMnO_3$ thin films. *Journal of Applied Physics*, 102(10):103901, 2007.

[104] E. Favre-Nicolin and L. Ranno. Anisotropic magnetoresistance in manganite films. *Journal of Magnetism and Magnetic Materials*, 272-276, Part 3(0):1814 – 1815, 2004. Proceedings of the International Conference on Magnetism (ICM 2003).

[105] T. S. Santos, J. S. Lee, P. Migdal, I. C. Lekshmi, B. Satpati, and J. S. Moodera. Room-temperature tunnel magnetoresistance and spin-polarized tunneling through an organic semiconductor barrier. *Phys. Rev. Lett.*, 98:016601, Jan 2007.

[106] W. Xu, G.J. Szulczewski, P. LeClair, I. Navarrete, R. Schad, G. Miao, H. Guo, and A. Gupta. Tunneling magnetoresistance observed in $La_{0.7}Sr_{0.3}MnO_3$/organic molecule/Co junctions. *Applied Physics Letters*, 90(7):–, 2007.

[107] V. Dediu, L.E. Hueso, I. Bergenti, A. Riminucci, F. Borgatti, P. Graziosi, C. Newby, F. Casoli, M. P. De Jong, C. Taliani, and Y. Zhan. Room-temperature spintronic effects in Alq_3-based hybrid devices. *Phys. Rev. B*, 78:115203, Sep 2008.

[108] D. Sun, L. Yin, C. Sun, H. Guo, Z. Gai, X.G. Zhang, T.Z. Ward, Z. Cheng, and J. Shen. Giant magnetoresistance in organic spin valves. *Phys. Rev. Lett.*, 104:236602, Jun 2010.

[109] J.S. Jiang, J.E. Pearson, and S.D. Bader. Absence of spin transport in the organic semiconductor Alq_3. *Phys. Rev. B*, 77:035303, Jan 2008.

[110] M. Grünewald, R. Göckeritz, N. Homonnay, F. Würthner, L.W. Molenkamp, and G. Schmidt. Vertical organic spin valves in perpendicular magnetic fields. *Physical Review B*, 88(8):085319, 2013.

[111] S.W. Liu, J.H. Lee, C.C. Lee, C.T. Chen, and J.K. Wang. Charge carrier mo-

bility of mixed-layer organic light-emitting diodes. *Applied Physics Letters*, 91(14):142106, 2007.

[112] S. Majumdar, H.S. Majumdar, R. Laiho, and R. Österbacka. Comparing small molecules and polymer for future organic spin-valves. *Journal of alloys and compounds*, 423(1):169–171, 2006.

[113] H. Vinzelberg, J. Schumann, D. Elefant, R.B. Gangineni, J. Thomas, and B. Büchner. Low temperature tunneling magnetoresistance on (La,Sr)/MnO_3/Co junctions with organic spacer layers. *Journal of Applied Physics*, 103(9):093720, 2008.

[114] F.J. Wang, C.G. Yang, Z.V. Vardeny, and X.G. Li. Spin response in organic spin valves based on $La_{0.7}Sr_{0.3}mnO_3$ electrodes. *Physical Review B*, 75(24):245324, 2007.

[115] F.J. Wang, Z.H. Xiong, D. Wu, J. Shi, and Z.V. Vardeny. Organic spintronics: The case of Fe/Alq3/Co spin-valve devices. *Synthetic Metals*, 155(1):172 – 175, 2005.

[116] J. R. Petta, S. K. Slater, and D. C. Ralph. Spin-dependent transport in molecular tunnel junctions. *Phys. Rev. Lett.*, 93:136601, Sep 2004.

[117] Y. Ando, J. Murai, T. Miyashita, and T. Miyazaki. Spin dependent tunneling in 80nife/lb film with ferrocene and tris(bipyridine)ruthenium derivatives/co junctions. *Thin Solid Films*, 331(1 - 2):158 – 164, 1998.

[118] T.X. Wang, H.X. Wei, Z.M. Zeng, X.F. Han, Z.M. Hong, and G.Q. Shi. Magnetic/nonmagnetic/magnetic tunnel junction based on hybrid organic langmuir-blodgett-films. *Applied physics letters*, 88(24):242505–242505, 2006.

[119] R. Lin, F. Wang, J. Rybicki, M. Wohlgenannt, and K. A. Hutchinson. Distinguishing between tunneling and injection regimes of ferromagnet/organic semiconductor/ferromagnet junctions. *Phys. Rev. B*, 81:195214, May 2010.

[120] Y. Liu, S.M. Watson, T. Lee, J.M. Gorham, H.E. Katz, J.A. Borchers, H.D. Fairbrother, and D.H. Reich. Correlation between microstructure and mag-

netotransport in organic semiconductor spin-valve structures. *Phys. Rev. B*, 79:075312, Feb 2009.

[121] M. Grünewald, M. Wahler, F. Schumann, M. Michelfeit, C. Gould, R. Schmidt, F. Würthner, G. Schmidt, and L.W. Molenkamp. Tunneling anisotropic magnetoresistance in organic spin valves. *Physical Review B*, 84(12):125208, 2011.

[122] F. Wang, F. Macia, M. Wohlgenannt, A.D. Kent, and M.E. Flatté. Magnetic fringe-field control of electronic transport in an organic film. *Physical Review X*, 2(2):021013, 2012.

[123] F.G. Monzon, H.X. Tang, and M.L. Roukes. Magnetoelectronic phenomena at a ferromagnet-semiconductor interface. *Physical review letters*, 84(21):5022, 2000.

[124] M. Johnson and R.H. Silsbee. Interfacial charge-spin coupling: Injection and detection of spin magnetization in metals. *Physical Review Letters*, 55(17):1790, 1985.

[125] J. Li, B. Huang, and I. Appelbaum. Oblique hanle effect in semiconductor spin transport devices. *Applied Physics Letters*, 92(14):142507, 2008.

[126] F.J. Jedema, H.B. Heersche, A.T. Filip, J.J.A. Baselmans, and B.J. Van Wees. Electrical detection of spin precession in a metallic mesoscopic spin valve. *Nature*, 416(6882):713–716, 2002.

[127] B. Huang, D.J. Monsma, and I. Appelbaum. Coherent spin transport through a 350 micron thick silicon wafer. *Phys. Rev. Lett.*, 99:177209, Oct 2007.

[128] V. Coropceanu, J. Cornil, D.A. da Silva Filho, Y. Olivier, R. Silbey, and J.L. Brédas. Charge transport in organic semiconductors. *Chemical reviews*, 107(4):926–952, 2007.

[129] K. Ando, S. Watanabe, S. Mooser, E. Saitoh, and H. Sirringhaus. Solution-processed organic spin–charge converter. *Nature materials*, 12(7):622–627, 2013.

[130] S. Watanabe, K. Ando, K. Kang, S. Mooser, Y. Vaynzof, H. Kurebayashi, E. Saitoh, and H. Sirringhaus. Polaron spin current transport in organic semiconductors. *Nature Physics*, 10(4):308–313, 2014.

[131] E. Saitoh, M. Ueda, H. Miyajima, and G. Tatara. Conversion of spin current into charge current at room temperature: Inverse spin-hall effect. *Applied Physics Letters*, 88(18):182509, 2006.

[132] S.O. Valenzuela and M. Tinkham. Direct electronic measurement of the spin hall effect. *Nature*, 442(7099):176–179, 2006.

[133] T. Kimura, Y. Otani, T. Sato, S. Takahashi, and S. Maekawa. Room-temperature reversible spin hall effect. *Physical review letters*, 98(15):156601, 2007.

[134] Y. Kajiwara, K. Harii, S. Takahashi, J. Ohe, K. Uchida, M. Mizuguchi, H. Umezawa, H. Kawai, K. Ando, K. Takanashi, et al. Transmission of electrical signals by spin-wave interconversion in a magnetic insulator. *Nature*, 464(7286):262–266, 2010.

[135] S.W. Jiang, S. Liu, P. Wang, Z.Z. Luan, X.D. Tao, H.F. Ding, and D. Wu. Exchange-dominated pure spin current transport in Alq_3 molecules. *Physical review letters*, 115(8):086601, 2015.

[136] Z.G. Yu. Suppression of the hanle effect in organic spintronic devices. *Physical review letters*, 111(1):016601, 2013.

[137] S. Sanvito. Molecular spintronics: The rise of spinterface science. *Nature Physics*, 6(8):562–564, 2010.

[138] T. Suzuki, M. Kurahashi, and Y. Yamauchi. Spin polarization in molecular orbitals of copper-phthalocyanine deposited on a magnetized Fe(100) substrate. *The Journal of Physical Chemistry B*, 106(31):7643–7646, 2002.

[139] A. Scheybal, T. Ramsvik, R. Bertschinger, M. Putero, F. Nolting, and T.A. Jung. Induced magnetic ordering in a molecular monolayer. *Chemical physics letters*, 411(1):214–220, 2005.

[140] H. Wende, M. Bernien, J. Luo, C. Sorg, N. Ponpandian, J. Kurde, J. Miguel, M. Piantek, X. Xu, P. Eckhold, et al. Substrate-induced magnetic ordering and switching of iron porphyrin molecules. *Nature materials*, 6(7):516–520, 2007.

[141] M. Bernien, X. Xu, J. Miguel, M. Piantek, P. Eckhold, J. Luo, J. Kurde, W. Kuch, K. Baberschke, H. Wende, et al. Fe-porphyrin monolayers on ferromagnetic substrates: Electronic structure and magnetic coupling strength. *Physical Review B*, 76(21):214406, 2007.

[142] F. Djeghloul, F. Ibrahim, M. Cantoni, M. Bowen, L. Joly, S. Boukari, P. Ohresser, F. Bertran, P. Le Fevre, P. Thakur, et al. Direct observation of a highly spin-polarized organic spinterface at room temperature. *Scientific reports*, 3, 2013.

[143] S. Steil, N. Großmann, M. Laux, A. Ruffing, D. Steil, M. Wiesenmayer, S. Mathias, O.L.A Monti, M. Cinchetti, and M. Aeschlimann. Spin-dependent trapping of electrons at spinterfaces. *Nature Physics*, 9(4):242–247, 2013.

[144] C. Barraud, P. Seneor, R. Mattana, S. Fusil, K. Bouzehouane, C. Deranlot, P. Graziosi, L. Hueso, I. Bergenti, V. Dediu, et al. Unravelling the role of the interface for spin injection into organic semiconductors. *Nature Physics*, 6(8):615–620, 2010.

[145] R. Göckeritz, N. Homonnay, A. Müller, T. Richter, B. Fuhrmann, and G. Schmidt. Nanosized perpendicular organic spin-valves. *Applied Physics Letters*, 106(10):102403, 2015.

[146] Nicolae Atodiresei, Jens Brede, Predrag Lazić, Vasile Caciuc, Germar Hoffmann, Roland Wiesendanger, and Stefan Blügel. Design of the local spin polarization at the organic-ferromagnetic interface. *Physical review letters*, 105(6):066601, 2010.

[147] L.O. Chua and S.M. Kang. Memristive devices and systems. *Proceedings of the IEEE*, 64(2):209–223, 1976.

[148] TW Hickmott. Low frequency negative resistance in thin anodic oxide films. *Journal of Applied Physics*, 33(9):2669–2682, 1962.

[149] F. Argall. Switching phenomena in titanium oxide thin films. *Solid-State Electronics*, 11(5):535 – 541, 1968.

[150] L.E. Hueso, I. Bergenti, A. Riminucci, Y.Q. Zhan, and V. Dediu. Multipurpose magnetic organic hybrid devices. *Advanced Materials*, 19(18):2639–2642, 2007.

[151] P. Graziosi, M. Prezioso, A. Gambardella, C. Kitts, R.K. Rakshit, A. Riminucci, I. Bergenti, F. Borgatti, C. Pernechele, M. Solzi, D. Pullini, D. Busquets-Mataix, and V.A. Dediu. Conditions for the growth of smooth $La_{0.7}Sr_{0.3}MnO_3$ thin films by pulsed electron ablation. *Thin Solid Films*, 534(0):83 – 89, 2013.

[152] M. Galbiati, S. Tatay, S. Delprat, H. Le Khanh, B. Servet, C. Deranlot, S. Collin, P. Seneor, R. Mattana, and F. Petroff. Is spin transport through molecules really occurring in organic spin valves? a combined magnetoresistance and inelastic electron tunnelling spectroscopy study. *Applied Physics Letters*, 106(8):082408, 2015.

[153] H.J. Jang, K.P. Pernstich, D.J. Gundlach, O.D. Jurchescu, and C.A. Richter. Observation of spin-polarized electron transport in Alq3 by using a low work function metal. *Applied Physics Letters*, 101(10):102412, 2012.

[154] S.W. Jiang, B.B. Chen, P. Wang, Y. Zhou, Y.J. Shi, F.J. Yue, H.F. Ding, and D. Wu. Voltage polarity manipulation of the magnetoresistance sign in organic spin valve devices. *Applied Physics Letters*, 104(26):262402, 2014.

[155] S.W. Jiang, D.J. Shu, L. Lin, Y.J. Shi, J. Shi, H.F. Ding, J. Du, M. Wang, and D. Wu. Strong asymmetrical bias dependence of magnetoresistance in organic spin valves: the role of ferromagnetic/organic interfaces. *New Journal of Physics*, 16(1):013028, 2014.

[156] Y. Liu, S.M. Watson, T. Lee, J.M. Gorham, H.E. Katz, J.A. Borchers, H.D. Fairbrother, and D.H. Reich. Correlation between microstructure and magne-

totransport in organic semiconductor spin-valve structures. *Physical Review B*, 79(7):075312, 2009.

[157] J.J.H.M. Schoonus, P.G.E. Lumens, W. Wagemans, J.T. Kohlhepp, P.A. Bobbert, H.J.M. Swagten, and B. Koopmans. Magnetoresistance in hybrid organic spin valves at the onset of multiple-step tunneling. *Physical review letters*, 103(14):146601, 2009.

[158] L. Schulz, L. Nuccio, M. Willis, P. Desai, P. Shakya, T. Kreouzis, V.K. Malik, C. Bernhard, F.L. Pratt, N.A. Morley, et al. Engineering spin propagation across a hybrid organic/inorganic interface using a polar layer. *Nature materials*, 10(1):39–44, 2011.

[159] G. Szulczewski, H. Tokuc, K. Oguz, and J.M.D. Coey. Magnetoresistance in magnetic tunnel junctions with an organic barrier and an mgo spin filter. *Applied Physics Letters*, 95(20):202506, 2009.

[160] F.J. Wang, Z.H. Xiong, D. Wu, J. Shi, and Z.V. Vardeny. Organic spintronics: the case of Fe/Alq_3/Co spin-valve devices. *Synthetic Metals*, 155(1):172–175, 2005.

[161] S. Wang, Y.J. Shi, L. Lin, B.B. Chen, F.J. Yue, J. Du, H.F. Ding, F.M. Zhang, and D. Wu. Room-temperature spin valve effects in $La_{0.67}Sr_{0.33}MnO_3$/Alq_3/Co devices. *Synthetic Metals*, 161(15):1738–1741, 2011.

[162] X. Zhang, S. Mizukami, Q. Ma, T. Kubota, M. Oogane, H. Naganuma, Y. Ando, and T. Miyazaki. Spin-dependent transport behavior in c60 and Alq3 based spin valves with a magnetite electrode. *Journal of Applied Physics*, 115(17):172608, 2014.

[163] R.G. Kepler, P.M. Beeson, S.J. Jacobs, R.A. Anderson, M.B. Sinclair, V.S. Valencia, and P.A. Cahill. Electron and hole mobility in tris (8-hydroxyquinolinolato-n1, o8) aluminum. *Applied physics letters*, 66(26):3618–3620, 1995.

[164] B.J. Chen, W.Y. Lai, Z.Q. Gao, C.S. Lee, S.T. Lee, and W.A. Gambling. Electron drift mobility and electroluminescent efficiency of tris (8-

hydroxyquinolinolato) aluminum. *Applied Physics Letters*, 75(25):4010–4012, 1999.

[165] G.G. Malliaras, Y. Shen, D.H. Dunlap, H. Murata, and Z.H. Kafafi. Nondispersive electron transport in Alq3. Technical report, DTIC Document, 2001.

[166] W.F. Brinkman, R.C. Dynes, and J.M. Rowell. Tunneling conductance of asymmetrical barriers. *Journal of Applied Physics*, 41(5), 1970.

[167] L.I. Glazman and K.A. Matveev. Inelastic tunneling across thin amorphous films. *Sov. Phys. JETP*, 67(6):1276–82, 1988.

[168] Tunneling characteristics and resistivity behavior of $La_{0.6}Pb_{0.4}MnO_3$.

[169] S.Lundqvist E.Burstein. *Tunneling Phenomena in Solids.* Plenum Press, New York, 1969.

[170] B.J. Jonsson-Akerman, R. Escudero, C. Leighton, S. Kim, I.K. Schuller, and D.A. Rabson. Reliability of normal-state current-voltage characteristics as an indicator of tunnel-junction barrier quality. *Applied Physics Letters*, 77(12):1870–1872, 2000.

[171] D.A. Rabson, B.J. Jönsson-Åkerman, A.H. Romero, R. Escudero, C. Leighton, S. Kim, and I.K. Schuller. Pinholes may mimic tunneling. *Journal of Applied Physics*, 89(5):2786–2790, 2001.

[172] I.J.V. Marún, F.M. Postma, J.C. Lodder, and R. Jansen. Tunneling magnetoresistance with positive and negative sign in $La_{0.67}Sr_{0.33}MnO_3/SrTiO_3/Co$ junctions. *Physical Review B*, 76(6):064426, 2007.

[173] M. Viret, M. Drouet, J. Nassar, J.P. Contour, C. Fermon, and A. Fert. Low-field colossal magnetoresistance in manganite tunnel spin valves. *EPL (Europhysics Letters)*, 39(5):545, 1997.

[174] J.Z. Sun, K.P. Roche, and S.S.P. Parkin. Interface stability in hybrid metal-oxide magnetic trilayer junctions. *Physical Review B*, 61(17):11244, 2000.

[175] R. Galceran, L. Balcells, A. Pomar, Z. Konstantinović, F. Sandiumenge, and B. Martínez. Transport properties of $La_{2/3}Sr_{1/3}MnO_3/LaAlO_3/Pt$ tunnel junctions. *Journal of Applied Physics*, 117(10):103909, 2015.

[176] J. Ventura, J.M. Teixeira, J.P. Araujo, J.B. Sousa, P. Wisniowski, and P.P. Freitas. Pinholes and temperature-dependent transport properties of mgo magnetic tunnel junctions. *Phys. Rev. B*, 78:024403, Jul 2008.

[177] N Garcia, M Munoz, and Y-W Zhao. Magnetoresistance in excess of 200% in ballistic ni nanocontacts at room temperature and 100 Oe. *Physical Review Letters*, 82(14):2923, 1999.

[178] N Garcıa. Conducting ballistic magnetoresistance and tunneling magnetoresistance: Pinholes and tunnel barriers. *Applied Physics Letters*, 77(9):1351–1353, 2000.

[179] W.H. Rippard, A.C. Perrella, F.J. Albert, and R.A. Buhrman. Ultrathin aluminum oxide tunnel barriers. *Physical review letters*, 88(4):046805, 2002.

[180] A. Bedoya-Pinto, H. Prima-García, F. Casanova, E. Coronado, and L.E. Hueso. Spin-polarized hopping transport in magnetically tunable rare-earth quinolines. *Advanced Electronic Materials*, 2015.

[181] P.E. Liley C.Y. Ho, R.W. Powell. *Physical and Chemical reference data*. American Chemical Society, New York, 1975.

[182] T. Okuda, Y. Tomioka, A. Asamitsu, and Y. Tokura. Low-temperature properties of $La_{1-x}Ca_xMnO_3$ single crystals: Comparison with $La_{1-x}Sr_xMnO_3$. *Physical Review B*, 61(12):8009, 2000.

[183] J.B. Wachtman Jr, W.E. Tefft, D.G. Lam Jr, and C.S. Apstein. Exponential temperature dependence of young's modulus for several oxides. *Physical review*, 122(6):1754, 1961.

[184] T.S. Kim. Inverse tunneling magnetoresistance in nanoscale magnetic tunnel junctions. *Physical Review B*, 72(2):024401, 2005.

[185] J.M. De Teresa, A. Barthelemy, A. Fert, J.P. Contour, F. Montaigne, and P. Seneor. Role of metal-oxide interface in determining the spin polarization of magnetic tunnel junctions. *Science*, 286(5439):507–509, 1999.

[186] J.L. Moruzzi, J.F. Janak, and A.R. Williams. Calculated band structure properties, 1978.

[187] M.N. Grecu, A.M., C. Ghica, M. Calle, and M. Schwoerer. Paramagnetic defect centres in crystalline Alq_3. *Journal of Physics: Condensed Matter*, 17(39):6271, 2005.

[188] B.J. Chen, W.Y. Lai, Z.Q. Gao, C.S. Lee, S.T. Lee, and W.A. Gambling. Electron drift mobility and electroluminescent efficiency of tris (8-hydroxyquinolinolato) aluminum. *Applied Physics Letters*, 75(25):4010–4012, 1999.

[189] A. Riminucci, M. Prezioso, P. Graziosi, and C. Newby. Electrode artifacts in low resistance organic spin valves. *Applied Physics Letters*, 96(11):112505, 2010.

[190] P. Graziosi, A. Gambardella, M. Prezioso, A. Riminucci, I. Bergenti, N. Homonnay, G. Schmidt, D. Pullini, and D. Busquets-Mataix. Polaron framework to account for transport properties in metallic epitaxial manganite films. *Physical Review B*, 89(21):214411, 2014.

[191] W. Oepts, H.J. Verhagen, R. Coehoorn, and W.J.M. De Jonge. Analysis of breakdown in ferromagnetic tunnel junctions. *Journal of applied physics*, 86(7):3863–3872, 1999.

[192] O. Kurnosikov, F.C. de Nooij, P. LeClair, J.T. Kohlhepp, B. Koopmans, H.J.M. Swagten, and W.J.M. de Jonge. Stm-induced reversible switching of local conductivity in thin Al_2O_3 films. *Physical Review B*, 64(15):153407, 2001.

[193] M. Cölle, M. Büchel, and D.M. de Leeuw. Switching and filamentary conduction in non-volatile organic memories. *Organic Electronics*, 7(5):305–312, 2006.

[194] J.J. Yang, M.D. Pickett, X. Li, D.A.A. Ohlberg, D.R. Stewart, and R.S. Williams. Memristive switching mechanism for metal/oxide/metal nanodevices. *Nature nanotechnology*, 3(7):429–433, 2008.

[195] H. Nili, S. Walia, A.E. Kandjani, R. Ramanathan, P. Gutruf, T. Ahmed, S. Balendhran, V. Bansal, D. B Strukov, O. Kavehei, et al. Donor-induced

performance tuning of amorphous $SrTiO_3$ memristive nanodevices: Multistate resistive switching and mechanical tunability. *Advanced Functional Materials*, 2015.

[196] L.D. Bozano, B.W. Kean, V.R. Deline, J.R. Salem, and J.C. Scott. Mechanism for bistability in organic memory elements. *Applied Physics Letters*, 84(4):607–609, 2004.

[197] T. van Woudenbergh, J. Wildeman, P.W.M. Blom, J.J.A.M. Bastiaansen, and B.M.W. Langeveld-Vos. Electron-enhanced hole injection in blue polyfluorene-based polymer light-emitting diodes. *Advanced Functional Materials*, 14(7):677–683, 2004.

[198] M. Cölle, M. Büchel, and D.M. de Leeuw. Switching and filamentary conduction in non-volatile organic memories. *Organic Electronics*, 7(5):305–312, 2006.

[199] R. Schmechel and H. Von Seggern. Electronic traps in organic transport layers. *Physica status solidi (a)*, 201(6):1215–1235, 2004.

Ringraziamenti

Desidero ringraziare tutto il gruppo di spintronica dell'ISMN di Bologna con cui ho collaborato in questi anni: Alek, Alessandro, Elisabetta, Eugenio, Federico, Francesco, Ilaria, Lorenzo, Mauro, Mirko, Patrizio, Raimondo e Silvio.
Un ringraziamento particolare va ad Alberto, per la disponibilità con cui mi ha seguito in questo lavoro di tesi.
Grazie a Lucia per il suo supporto dall'università.
Un grande grazie va alla mia famiglia e agli amici con cui ho condiviso questo periodo.